Self-heating of HEMT low-noise amplifiers in liquid cryogenic environments and the limits of microwave noise performance

Thesis by
Anthony J. Ardizzi

In Partial Fulfillment of the Requirements for the
Degree of
Doctor of Philosophy

CALIFORNIA INSTITUTE OF TECHNOLOGY
Pasadena, California

2022
Defended May 26, 2022

Anthony J. Ardizzi
ORCID: 0000-0001-8667-1208

ACKNOWLEDGMENTS

I sincerely thank both my advisors, Austin Minnich and Keith Schwab, for their immeasurable patience, support, and instruction. Without them I would not be where I am today, and I am forever indebted to each of them. I also extend my gratitude to all of my peers and collaborators during my time at Caltech, especially Jeff Botimer, Bekari Gabritchidze, Iretomiwa Esho, Alex Choi, Jacob Kooi, Kieran Cleary, and Greg MacCabe.

I also thank my mother, father, and my entire family for their unconditional love and support, and for granting me such a privileged and fortunate life where graduating with a PhD from Caltech could become a reality.

And to my lovely bride-to-be, words cannot express both my love and gratefulness for supporting me over the last several years, and for putting up with all my long hours in the lab.

ABSTRACT

Detection and processing of microwave signals is of substantial scientific importance in fields ranging from radio astronomy to quantum computing. An essential component of the signal processing chain is the microwave amplifier, which adds gain to the signal so that it may be processed by subsequent microwave components. However, the amplifier itself adds its own internally generated noise into the measurement chain. As a result, amplifiers which add a minimal amount of noise are crucial to any high precision measurement scheme. A device which is commonly employed for this task is the high-electron-mobility transistor (HEMT) amplifier. Understanding the fundamental limits of the microwave noise performance of HEMT amplifiers is highly desirable. Noise temperatures in these devices as low as 3 times the quantum limit have been observed in the last decade, but the lack of understanding of the origin of the excess noise has hindered further improvements. Noise in HEMTs is attributed to a generator at the output, known as drain noise; and a generator at the input, which is attributed to thermal noise of the gate. At cryogenic temperatures of ~4 K, thermal noise is predicted to be negligible. However, a plateau in noise temperature has been observed at physical temperatures below ~20 K, with a negligible improvement in noise performance upon further cooling.

The primary noise mechanism responsible for this plateau is believed to be ohmic heating of the HEMT structure induced by current in the active device channel, a process known as self-heating. At room temperature the ambient thermal noise dominates the amplifier's overall noise performance, but at the cryogenic temperatures required to achieve low-noise performance the self-heating effect produces thermal noise at the input of the HEMT gate which contributes significantly to the total noise. A potential mechanism to mitigate self-heating is to provide an additional thermal dissipation path for the Joule heating in the channel. However, given the sub-micron length scales and buried gate structure of HEMTs, thermal management is challenging. The primary heat conduction pathway, that of phonons travelling through the bulk HEMT substrate, decreases rapidly in magnitude at cryogenic temperatures. An alternative option is to submerge the HEMT in a cryogenic fluid, thereby presenting an alternate thermal conduction route through the HEMT surface into the fluid. This technique, while commonly employed in cryogenic thermal management of superconducting magnets, has not been investigated for HEMTs.

In this work we explore the use of liquid cryogenic cooling to directly mitigate

the effect of HEMT self-heating. We test in particular the effectiveness of cooling using superfluid helium-4, which has the highest known thermal conductivity of any known substance. We report a systematic experimental investigation of the noise performance of a cryogenic packaged two-stage HEMT low-noise amplifier over a wide range of biases in a 4.0–5.5 GHz frequency band, with the device immersed in a variety of cryogenic baths including helium-4 vapor, liquid helium-4, superfluid helium-4, and vacuum. We present the details of the experimental apparatus which was constructed to perform microwave noise measurements of the low-noise amplifier when submerged in a liquid cryogen environment. We interpret our results using a small-signal model of the amplifier and compare our findings with the predictions of a phonon radiation model of heat dissipation. We find that liquid cryogenic cooling is unable to mitigate the thermal noise associated with self-heating. Considering this finding, we examine the implications for the lower bounds of cryogenic noise performance in HEMTs by incorporating the effects of self-heating into the existing noise modelling of HEMT amplifiers. Our analysis supports the general design principle for cryogenic HEMTs of maximizing gain at the lowest possible power.

PUBLISHED CONTENT AND CONTRIBUTIONS

[1] A. J. Ardizzi, A. Y. Choi, B. Gabritchidze, J. Kooi, K. A. Cleary, A. C. Readhead, and A. J. Minnich, "Self-heating of cryogenic hemt amplifiers and the limits of microwave noise performance", arXiv:2205.03975 (2022),

Contributions: A.J.A. designed and constructed the experimental apparatus, wrote the LabVIEW and MATLAB scripts, acquired and analyzed the data, performed the small-signal model fitting, extended the amplifier noise modelling to include the effects of self-heating, and wrote the manuscript.

CONTENTS

LIST OF FIGURES

LIST OF TABLES

Chapter 1

INTRODUCTION

In this thesis we present a systematic investigation of the noise performance of a packaged high-electron-mobility transistor (HEMT) amplifier when immersed in various liquid cryogenic environments, including the quantum liquid superfluid helium-4. In this chapter we begin by providing a brief history of semiconductor devices leading to the development of HEMT amplifier technology, which we describe in greater depth. We then present an overview of helium-4, focusing particularly on superfluid helium-4, before finishing by detailing the heat transport properties of superfluid helium-4 and its uses as a cryogenic coolant.

1.1 HEMT overview

Electronic devices constructed from semiconductor materials are a hallmark of modern technology. First discovered in the 19th century by Thomas Seebeck [1] and Michael Faraday [2], it wasn't until the discovery of the electron, the advent of quantum mechanics, and the development of solid-state physics theory by scientists such as Johan Koenigsberger [3] and Ferdinand Bloch [4] in the early 20th century that semiconductor physics was more rigorously understood. The unique electronic properties of semiconductors, which possess resitivities spanning 11 orders of magnitude at room temperature [5, 6] that can be both precisely engineered through fabrication techniques and electrically tuned in situ at frequencies of up to several terahertz [7], naturally lend themselves to being excellent electrical switches and valves, controlling the flow of electrical current in an analogous manner to the control of liquid flow using hydrodynamic valves. The first semiconductor devices were point-contact rectifiers which were used as early radio wave detectors [8]. In 1947 the famous Bell Labs group consisting of William Shockley, John Bardeen, and Walter Brattain demonstrated successful operation of a bipolar transistor for the first time [9], for which they were awarded a Nobel Prize. Over the coming decades, semiconductor transistor technology exploded into widespread use and helped drive the development of computer chips, with modern chips containing tens of billions of metal–oxide–semiconductor field-effect transistor (MOSFET) switches [10]. Very rough estimates place the total number of MOSFET switches produced globally every year to be over 10^{21} as of 2020, a number which has grown exponentially

since the early 1970s [11].

The particular distinguishing feature of semiconductors when compared to pure insulators is their relatively smaller energy gap (bandgap), which are energies at which electron states cannot exist in the material's energy-momentum band structure. This permits electrons in semiconductors to more readily cross the bandgap from the valence band into the conduction band than in insulators [5, 6]. The conduction band can be made even more accessible by introducing lattice impurities into a semiconductor through a process known as doping, which creates allowed energy bands inside the bandgap near the bandgap edge and provides even more readily ionizable electron states. Thus through either appropriate selection of undoped semiconductors, referred to as "intrinsic" semiconductors, or through the engineering of the dopant density in doped semiconductors, referred to as "extrinsic" semiconductors, the electrical transport parameters most critical for high-speed device performance such as electron mobility (μ_e) which characterizes the average speed of electrons in a semiconductor, peak velocity (v_p) which is the peak charge carrier velocity for a semiconductor subjected to strong electric fields, and the effective mass of charge carriers (m^*) can all be adjusted [12].

The most commonly used semiconductor material by far is silicon (Si) due to its relatively low production costs, superior rectifying properties and high-temperature workability when compared with its immediate competitor germanium (Ge) [13]. However, through decades of research into high-performance devices it was found that III-V semiconductors such as gallium arsenide (GaAs) and more recently indium phosphide (InP) possess far superior transport properties at high frequencies [12, 14, 15]. These materials are thus used to make analog amplifier devices with high operating frequencies and excellent low-noise properties, known as high-electron-mobility transistor (HEMT) amplifiers, the primary subject of study in this work. The technology of HEMTs evolved from the metal-semiconductor field-effect transistor (MESFET) technologies of the 1960s and 1970s, first through research at IBM where exceptional transport properties were demonstrated [16], and then through research at laboratories located throughout the world such as Bell Laboratories [17, 18], the National Radio Astronomy Observatory in Charlottesville, VA [19–22], the Thomson-CSF laboratory in France [23], Fujitsu Labs in Japan [24], the University of Massachusetts [25], the Jet Propulsion Laboratory in Pasadena, CA [26–28], the California Institute of Technology in Pasadena, CA [29, 30], Chalmers University of Technology in Sweden [31–33], the University of Manchester [34], and Fraunhofer

IAF in Germany [35], to name just a few.

Conduction in GaAs MESFETs occurs through a Si doped GaAs conduction channel. The use of an extrinsic semiconductor for the channel material causes a significant reduction in electron mobility and an increase in overall noise when compared with intrinsic semiconductors due to electron scattering off of the dopant impurities. The improvement of the HEMT over the MESFET was to instead use an intrinsic narrow bandgap channel layer, generally indium gallium arsenide (InGaAs) of varying indium contents, with free carriers being supplied by the diffusion of electrons from a doped donor layer [36]. Drastically improved electron mobilities are observed in HEMTs over MESFETS, with typical increases of over 50% at room temperature ($\mu_e \simeq 4000$ cm^2 V^{-1} s^{-1} in MESFETs versus $\mu_e \simeq 8500$ cm^2 V^{-1} s^{-1} in HEMTS) and over a factor of 10 improvement at liquid nitrogen temperatures ($\mu_e \simeq 6000$ cm^2 V^{-1} s^{-1} in MESFETs versus $\mu_e \simeq 80000$ cm^2 V^{-1} s^{-1} in HEMTS) [12].

Figure 1.1(a) shows an example of an epitaxial layer structure of a metamorphic HEMT grown on a GaAs substrate, and reflects the transistors used in the device presented in this thesis. We discuss the stack from top to bottom. Coating the entire device is a silicon nitride (SiN) passivation layer which improves stability by preventing the semiconductor surfaces from being oxidized in uncontrolled ways, both immediately after fabrication and in the long-term [37]. The gate metal is of the double-mushroom style [38] and forms a Schottky contact with the wide-bandgap indium aluminum arsenide (InAlAs) barrier layer. This barrier layer is delta doped with silicon, which is the doping of only a thin layer of semiconductor material performed by growth-interrupted impurity deposition [39], and supplies the electrons which ultimately conduct in the undoped narrow-bandgap InGaAs channel. Conduction through the channel occurs in the two-dimensional electron gas which forms below the interface of the barrier and channel. Between the channel layer and the GaAs substrate, an InAlAs metamorphic buffer layer is employed which gradually transitions the indium content to match the different lattice constants of the channel and substrate, minimizing the presence of defects associated with lattice mismatch which degrade device performance [40, 41]. Source and drain contacts are made from Si doped InGaAs to yield small contact resistances. The general convention is to refer to devices grown on GaAs substrates colloquially as GaAs HEMTs, and HEMTs grown on InP substrates colloquially as InP HEMTs, with each designation implying the use of an InGaAs channel, a convention which we follow.

The band structure of the HEMT is shown schematically in Fig. 1.1(b). The delta

doping, which is the doping of only a thin layer of semiconductor material performed by growth-interrupted impurity deposition [39], causes bending of the InAlAs bands so that when a sufficiently high gate-source bias V_{GS} is applied electrons are able to diffuse into the quantum well created at the heterojunction of the InAlAs-InGaAs interface, with the wider bandgap of the barrier layer preventing electrons from conducting in the doped InAlAs layer. A two-dimensional electron gas is confined here, represented by the green shaded area, which acts as the conduction channel in the device. The InGaAs conduction energy E_C, valence energy E_V, and the Fermi energy E_F are also shown.

HEMT technology is now used ubiquitously in measurement schemes that require a microwave-frequency low-noise amplifier (LNA), with modern devices exhibiting truly exceptional noise properties. An amplifier's noise contribution is typically characterized by its input referred noise temperature T_e, which is the temperature that a matched resistor connected at a noiseless amplifier's input would have if it were to contribute the same magnitude of noise as the noisy amplifier, as shown schematically in Figs. 1.2(a) and 1.2(b). Modern HEMTs exhibit noise temperatures as low as 3–5 times larger than the absolute lower limit set by quantum mechanics (the quantum limit) at operational frequencies of 2–50 GHz, and 10–100 times larger than the quantum limit at frequencies of 50–1000 GHz, with worsening performance at higher frequencies [42–45].

With such favorable noise properties, HEMTs are a key component of high precision measurements across diverse fields in science and engineering such as radio astronomy [14, 44], deep-space communication [26], and quantum computing [46–50]. In radio astronomy applications, HEMT LNAs cooled to 10–20 K typically serve as the first stage of amplification, with superconducting mixers placed at the LNA input to downconvert frequencies above 100 GHz [44] . In quantum computing applications, particularly in superconducting qubit architectures, HEMT LNAs act as the second stage of amplification after a first stage of quantum-limited amplification typically performed by a superconducting parametric amplifier [48]. Since in general the manufacturing and operation of HEMT LNAs are far simpler than for parametric amplifiers which require fabrication techniques akin to that of superconducting qubits as well as an additional microwave frequency pump tone for biasing [51], and since double and triple stage HEMT LNAs typically exhibit much higher gain than a superconducting parametric amplifier, developing a quantum-limited HEMT LNA whose operating power is sufficiently low for it to be mounted directly on

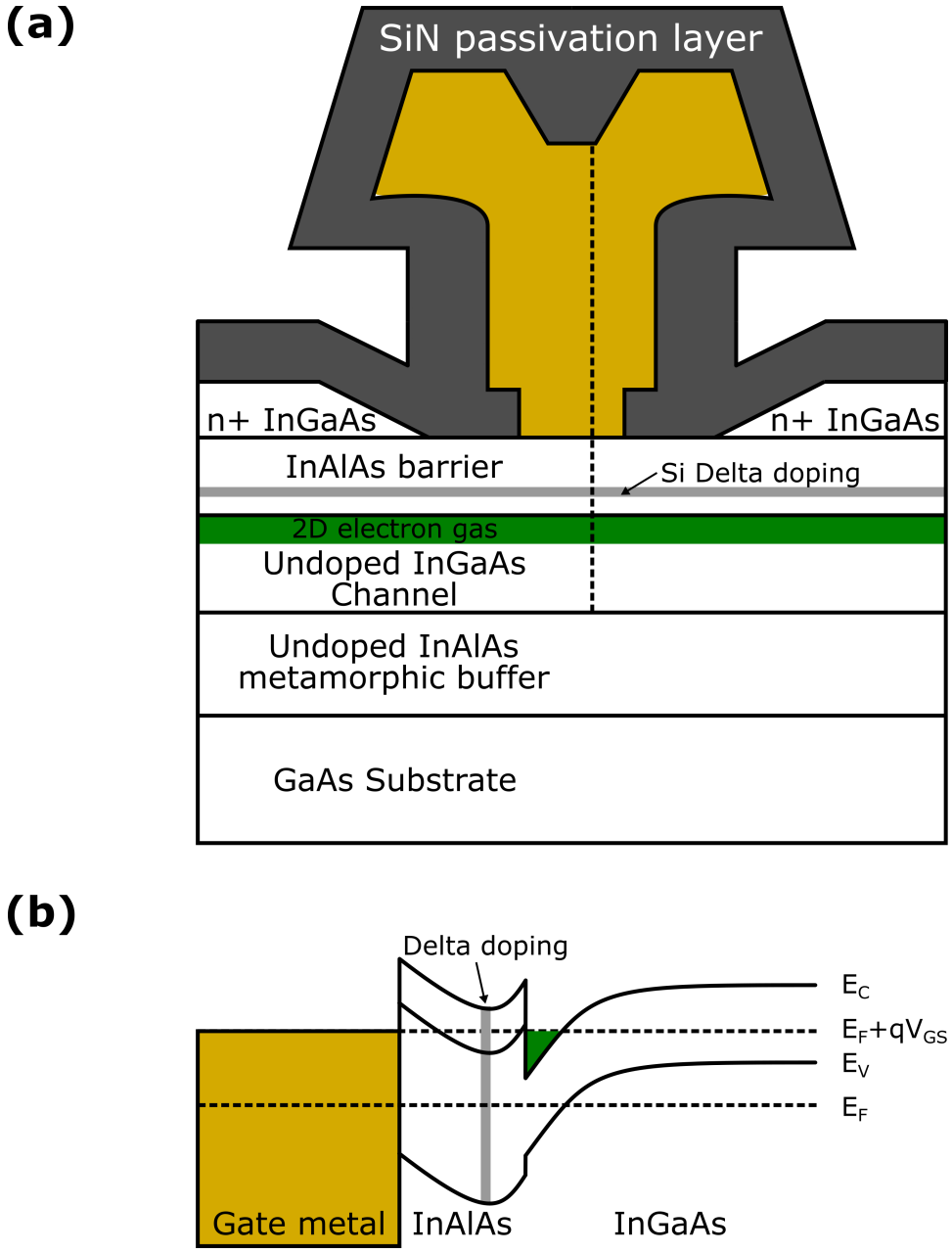

Fig. 1.1: **(a)** Epitaxial layer profile of the OMMIC 70 nm GaAs mHEMT. **(b)** Schematic of the energy band structure along the dotted-line slice in **(a)**, demonstrating how the two-dimensional electron (green region) is populated from the band bending provided by doping of the InAlAs barrier layer.

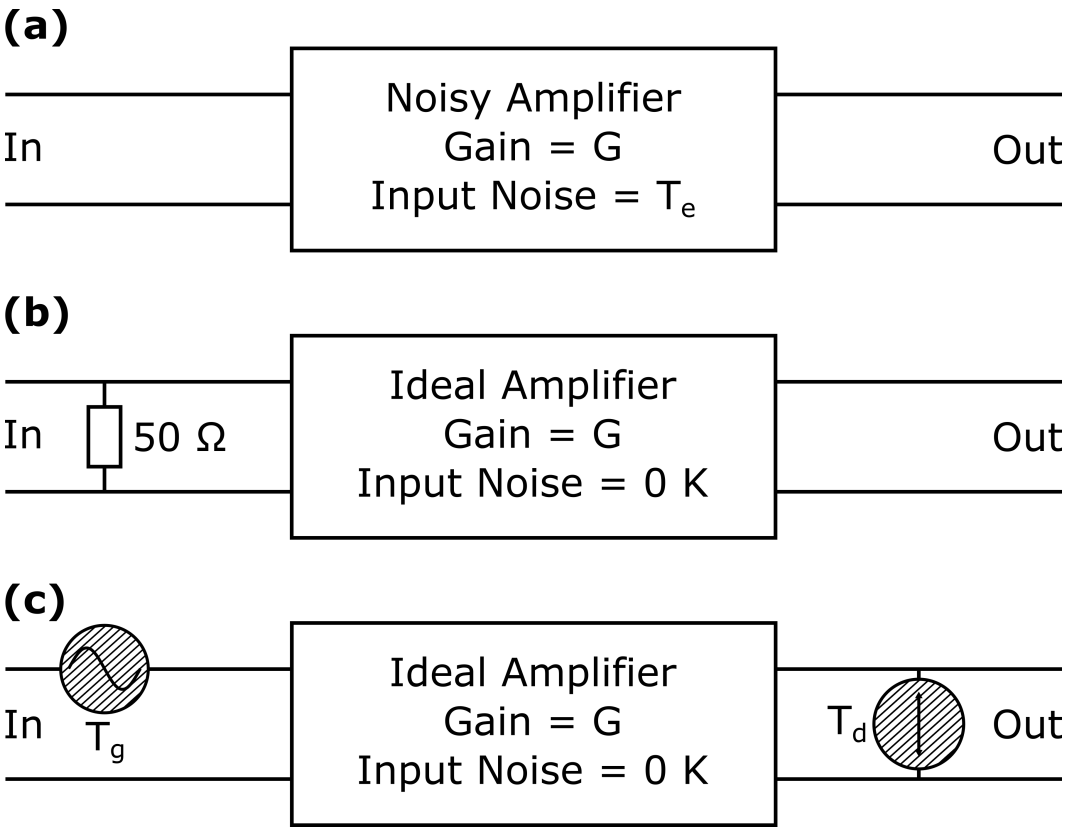

Fig. 1.2: Schematic representations of a noisy amplifier. (**a**) Noise is interpreted as originating in the amplifier. (**b**) Noise is interpreted as originating in a 50 Ω resistor across the amplifier's input. (**c**) Noise is interpreted as originating in both the 'gate' noise generator at the amplifier's input and 'drain' noise generator at the amplifier's output.

the base stage of a dilution refrigerator would constitute a significant advancement to the development of superconducting qubits and ultimately, it is hoped, a fully fault-tolerant quantum computer based on this technology [49, 52].

Modelling the noise behavior of HEMT amplifiers is typically done using the Pospieszalski model of field-effect transistors (FETs) [53]. A schematic of the equivalent circuit in this representation is shown in Fig. 1.3. The elements of the intrinsic FET are the intrinsic resistance r_i which is assumed to generate noise at the gate temperature T_g, the drain conductance g_ds which is assumed to generate noise at the drain temperature T_d, the transconductance g_m which represents the transduction of voltage fluctuations in the gate to current fluctuations in the channel, the gate-source capacitance C_gs, and the gate-drain capacitance C_gd. A simplified schematic showing only the noise generators associated with T_g and T_d, with the remaining parameters carried by the frequency dependence of the amplifier gain

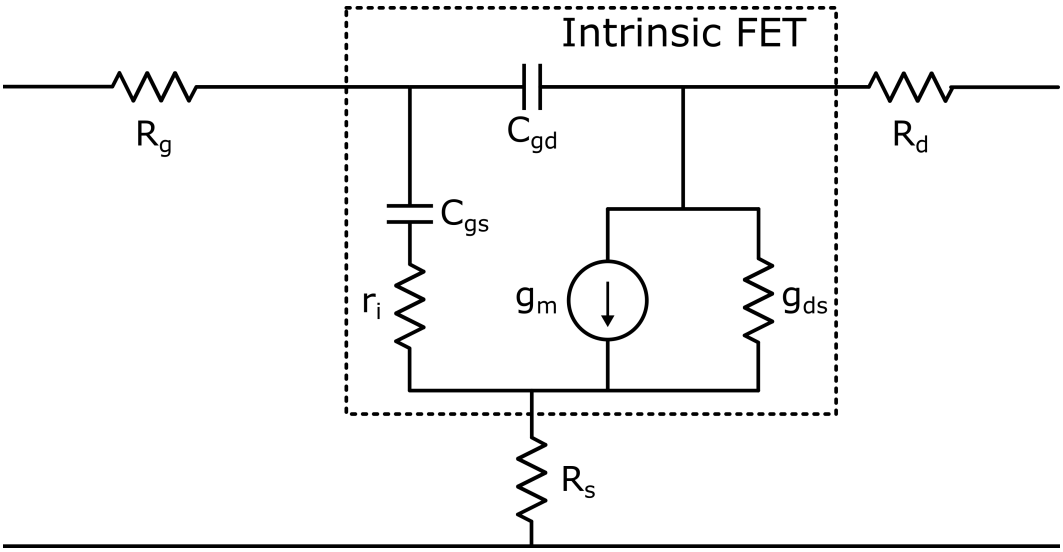

Fig. 1.3: Equivalent circuit of a FET. The intrinsic elements are enclosed by dotted lines.

G, is presented in Fig. 1.2(c). The extrinsic resistances associated with the ohmic contact resistances are the gate resistance R_{G}, the drain resistance R_{D}, and the source resistance R_{S}, which in this work we assume are all thermalized with the gate temperature T_{g}. We restate here the minimum noise temperature T_{min} of the intrinsic FET written using the formulation of the Pospiesalski noise model [22]:

$$T_{\mathrm{min}} \cong 2\frac{f}{f_{\mathrm{T}}}\sqrt{g_{\mathrm{ds}}T_{\mathrm{d}}r_{\mathrm{i}}T_{\mathrm{g}}} \tag{1.1}$$

where $f_{\mathrm{T}} = g_{\mathrm{m}}(2\pi C_{\mathrm{gs}})^{-1}$ is the intrinsic FET's cut-off frequency, and the simplified expression presented here is valid in the limit $f \ll f_{\mathrm{T}}$. Typical figures of merit for low-noise HEMTs involve the noise parameters comprising Eq. (1.1), with representative state-of-the-art cryogenic devices exhibiting values of $f_{\mathrm{T}} \gtrsim 500$ GHz, $g_{\mathrm{m}} \gtrsim 1400\,\mathrm{mS\,mm^{-1}}$, $g_{\mathrm{ds}} \lesssim 20$ mS, $T_{\mathrm{d}} \lesssim 200$ K, $r_i \lesssim 1\,\Omega$, and $T_{\mathrm{g}} \lesssim 20$ K [15, 38]. Since the Pospieszalski model is primarily a phenomenological model which relies on fitting to empirical data in order to determine these constituent parameters, other theories are required to understand the physical origins and limits of HEMT noise.

At present, the drain temperature T_{d} lacks an accepted physical origin, with several theories, generally related to the fluctuations of hot electrons in the HEMT channel, having been proposed. Early attempts at modelling drain noise attributed it to the spontaneous generation of dipole layers which drift through the channel to the drain contact [54]. A more testable theory was later made attributing drain noise

to suppressed shot noise, inspired by the fact that the observed drain noise current spectral density is proportional to the current, as is the case for pure shot noise [55, 56]. Most recently, drain noise has been attributed to real-space transfer of hot electrons which thermionically emit across the interface between the channel and barrier layers causing a significant fraction of electrons to conduct through the lower mobility barrier layer [57]. The value of T_d is typically much larger than the ambient device temperature and ranges from $T_d = 100$ K at liquid helium temperatures for state-of-the-art InP devices [49] to $T_d > 10000$ K at room temperature for GaAs devices [30], supporting the belief that drain noise is not thermal in origin. Further experimentation to test these theories [58] and develop devices with ever-lower drain noise through, for example, different indium channel contents [49] is an area of ongoing research. In this work, we simply take T_d as a fitting parameter without specific regard to its physical origin.

The gate temperature T_g, on the other hand, is widely accepted to be equal to the physical lattice temperature of the device down to cryogenic physical temperatures [22, 59], and the noise is assumed to be purely thermal in origin. Specifically, the gate noise is thought to originate primarily from ohmic losses associated with the gate metal which imprints its voltage fluctuations on the channel conductance, as well as possibly from losses in the small region of the channel closest to the source lead before the electrons are accelerated by the strong electric fields supplied by the gate and travel at their peak saturation velocity [55]. The parasitic resistances associated with the gate and source leads are also assumed to be equal to the ambient temperature. In this interpretation of gate noise, cryogenic cooling leads to improvements in the noise performance of the HEMT in part by decreasing the gate temperature and hence its thermal noise contribution, as well as by improving the intrinsic transport properties of the HEMT semiconductor material.

Cryogenic cooling of HEMT devices thus leads to a monotonic decrease in noise temperature with decreasing physical temperature. However, this trend has been observed to plateau below physical temperatures of 20 – 40 K (see Fig. 10 of [60], Fig. 1 of [28], and Fig. 2 of [61], for example). The physical origin of this plateau has been attributed to heating of the intrinsic gate resistance caused by power dissipated in the active channel, referred to as “self-heating”. In Ref. [28], Monte Carlo numerical simulations were performed to solve the Boltzmann transport equation inside an InP HEMT, which determined that the tens of milliwatts of power dissipation required for device biasing induced a region of elevated lattice

temperature localized inside the conduction channel. This localized temperature rise was found to saturate below ambient physical temperatures of approximately 30 K, persisting down to arbitrarily low temperatures. This channel heating is believed to induce heating of both the intrinsic gate resistance and the parasitic resistances associated with the gate and source leads.

A more intuitive understanding of self-heating can be understood through a black body phonon radiation model [45]. In this model, heat conduction channels across an interface are parameterized by occupation of available phonon modes, which at low temperatures can be predicted by the Debye model. The result is analogous to the Stefan-Boltzmann law for black body photon radiation, and it predicts a heat flux $q \propto T^4$ at low temperatures. Similar to the results of the Monte Carlo simulation method, this model predicts that at cryogenic temperatures heat transport away from the heated channel can no longer occur, and the gate temperature T_g saturates at approximately 20 K at physical temperatures below 20 K. These predictions were experimentally confirmed using a Schottky thermometry method based on the temperature-dependent diode characteristics of the HEMT gate [62]. Although heat dissipation in this experiment occurred directly in the HEMT gate metal, which was forward-biased to perform the thermometry measurements, as opposed to in the channel which is the case for normal HEMT amplifier operation, the confirmation of reduced heat transport at cryogenic temperatures is valid nonetheless. The predicted plateau in the gate temperature is thought to be responsible for the corresponding plateau in overall noise temperature.

To achieve improved device performance, mitigating the effect of self-heating is desirable. One approach is to design devices with optimal operating biases at sufficiently low powers that the effect of self-heating becomes negligible, an approach which has been actively pursued [31, 49]. Another approach is to provide additional heat conduction modes to the heated region. Thermal management of the gate in modern devices with sub-micron gate lengths and a buried gate structure is challenging, and there is no straightforward way to improve thermal conduction via solely solid-state methods. The approach taken here, which is the primary topic of investigation in this thesis, is to submerge the HEMT in a cryogenic fluid, in particular superfluid helium-4, a quantum fluid with the highest known thermal conductivity [63]. Such an approach is routinely used for cryogenic thermal management of superconducting magnets [64] and is actively employed in high-energy physics experiments [65–67]. However, the effectiveness of liquid cryogens to mitigate

self-heating in HEMTs has not yet been experimentally evaluated. The following sections in this chapter provide the background information on superfluid helium-4 required to understand the details of the heat transport mechanism proposed here.

1.2 Helium-4 overview

Helium, the second chemical element on the periodic table, forms an inert, colorless, odorless, non-toxic, monatomic gas at room temperature and barometric pressure. Seemingly uninteresting under such conditions, at sufficiently low temperatures helium becomes arguably the most interesting of all pure chemical elements. We list just a few of helium's unique properties, focusing in particular on the more abundant isotope helium-4: (a) after hydrogen, it is the second lightest and second most abundant element; (b) along with neon, it is the only element for which no known compounds exist; (c) since its zero-point energy is larger than its binding energy, it is the only element which does not freeze at any temperature under its own vapor pressure, transitioning to the liquid phase at 4.23 K in which it persists down to 0 K; (d) it is the only element which undergoes a second order phase transition and condenses into a quantum liquid at sufficiently low temperature, known as the "lambda point" due to the shape of the helium-4 specific heat versus temperature curve around $T_\lambda = 2.17$ K [68], under its own vapor pressure; (e) in this quantum liquid phase, it possesses the highest known thermal conductivity of any known substance [69].

The properties of liquid helium-4, which we denote as He II at temperatures $T < T_\lambda$ where the helium-4 is a quantum liquid or "superfluid", and He I at temperatures $T > T_\lambda$ where helium-4 is entirely a normal liquid, comprise an entire field of study in their own right, particularly in the superfluid regime [70–74]. The first observation of quantum fluidity was made in 1937 independently by Pyotr Kapitza in Russia [75] (to whom the Nobel Prize in physics was awarded), and John Allen and Don Misener at Cambridge [76, 77], which led to major advances in the understanding of low-temperature physics and spawned the fields of superconductivity in solid-state physics and superfluidity in condensed-matter physics of liquids and ultracold atomic gases. The complicated dynamics of superfluids such as quantized vortices [78], phase-slippage [79], and Josephson effects [80] have been studied extensively over the course of the twentieth century [81]. This has led to the development of several He II based technologies in recent years such as matter-wave interferometric devices [82, 83] used to measure the Earth's rotation, and superfluid optomechanical devices [84–86] which have been proposed as tabletop gravity wave detectors [87,

88] and dark-matter detectors [89, 90].

For our purposes, we focus on the study of heat transport and the use of liquid helium as a cryogenic liquid coolant [63, 91]. Helium is used extensively in modern cryogenic laboratories in a variety of different refrigeration systems, including gas-phase cryocoolers (base temperatures of 20 K) [92, 93], helium-4 refrigerators (base temperatures of 1 K), helium-3 refrigerators (base temperatures of 0.3 K), and dilution refrigerators (base temperatures of 0.02 K) [94–97]. Each of these technologies uses their cooling power to convectively cool several mounting "stages", which are generally machined sections of oxygen-free high-conductivity (OFHC) copper to which the components requiring cryogenic cooling are thermally strapped.

A more direct cooling method using helium is to submerge an object to be cooled directly in a bath of liquid helium. This method has the advantage of allowing the helium to directly extract heat which cannot readily conduct through the body of the object and is therefore localized to a particular region of the object's surface, but has the disadvantage of being more costly since in general a larger volume of liquid helium is required. Furthermore, since evaporatively cooling a bath of liquid helium-4 down to the superfluid state generally requires conversion of approximately 50% of the liquid into the gas state [96], if this vapor is not recaptured then a significant quantity of helium can be wasted. In some situations, this convective cooling method is required. Direct cooling using liquid helium is routinely used to cool high-field superconducting magnets [64]. Liquid He I is used ubiquitously in modern magnetic resonance imaging (MRI) devices [98] and in fusion reactor research [99–101]. Liquid He II is used in high-energy physics experiments such as the Large-Hadron Collider [65–67]. In the following section, we provide a more detailed account of the physical mechanisms which determine the transport properties of He II.

1.3 Superfluid helium-4 heat transport

The basis for understanding the transport properties of He II is the two-fluid model. First postulated by Laszlo Tisza in 1938 [102], a more rigorous quantum hydrodynamical account was given by Lev Landau in 1941 [103]. In this description, the fluid properties are comprised of a linear combination of two components, the normal fluid component with density ρ_n and the superfluid component with density ρ_s, with the overall fluid density given by the sum $\rho = \rho_s + \rho_n$. Landau showed

that the assumption of viscous-less fluid flow of the superfluid component leads to a velocity field $\mathbf{v_s}$ which obeys the Euler equation for ideal fluid flow, carrying with it zero entropy. We restate Euler's equation of motion here in the form derived in Ref. [68]:

$$\rho_s \frac{\mathrm{D}\mathbf{v_s}}{\mathrm{D}t} = -\frac{\rho_s}{\rho}\nabla P + \rho_s \sigma \nabla T \tag{1.2}$$

where ∇P is the pressure gradient, ∇T is the temperature gradient, and ρ is the total entropy per unit mass.

The normal fluid component responsible for entropy transport arises from the elementary excitations seen in the dispersion curve of energy E versus momentum k, with conservation laws predicting a gas of elementary thermal excitations which behave as an ordinary liquid governed by a Navier-Stokes type equation [68]:

$$\rho_n \frac{\mathrm{D}\mathbf{v_n}}{\mathrm{D}t} = -\frac{\rho_n}{\rho}\nabla P - \rho_s \sigma \nabla T + \eta_n \nabla^2 \mathbf{v_n} \tag{1.3}$$

where η_n is the normal fluid viscosity. In Fig. 1.4 we plot a smoothed spline to compiled energy-momentum dispersion data from neutron scattering experiments taken from Ref. [104], emphasizing both the linear dispersion regime near $k = 0$ associated with phonons which move at the speed of sound in helium, and the local minimum at higher energy associated with excitations called rotons. In 1947 Bogolyubov showed that a very similar dispersion for He II could be derived by treating it as a weakly-interacting Bose gas with a macroscopically occupied lowest energy state and excitations arising from the interactions [105]. In 1954 Feynamn further demonstrated the strong connection between the quantum hydrodynamic treatment by Landau and the interacting Bose condensate picture of Bogolyubov by applying his path-integral formulation to prove that the dispersion curve derived by Landau was a necessary consequence of an interacting Bose condensate [106]. Today, the understanding that He II is a Bose condensate described by the same physics as ultracold atomic gas condensates is well established.

The internal consistency and overall applicability of the two-fluid model has been confirmed by several classes of experiments, including the flow of He II in channels [107, 108], the flow of He II films [109–111] for which the question of whether He II film thickness depends on the motion of fluid in the film is still an open question, the He II fountain effect [112] wherein the interdependence of heat and mass flow in He II is most evident, and the propagation of sound waves [113] which have been used to make precise determinations of the thermophysical properties of He II. Arguably the most striking two-fluid model demonstration was performed by Andronikashvili

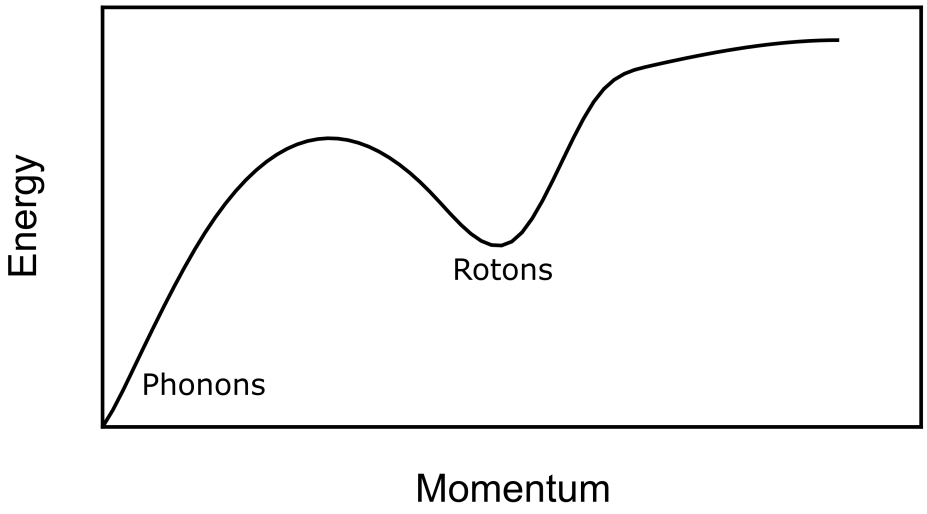

Fig. 1.4: Dispersion curve of He II emphasizing both the phonon and roton dissipation regimes.

in 1946 [114], where a stack of thin metal disks was suspended by a torsional fiber in He II and driven to oscillate. A measurement of the disks' oscillation frequency then gave a direct measurement of the viscosity of the liquid, and from this the normal fluid fraction ρ_n/ρ responsible for the viscosity η was inferred as a function of liquid temperature. The normal fluid fraction was found to obey a $T^{5.6}$ dependence, in approximate agreement with the predictions of the excitation spectrum determined by the calculations of Landau and Feynman. In Fig. 1.5 we plot a smoothed spline to compiled fluid fraction data from Ref. [104]. The sharp decrease in superfluid fraction above 1 K can be attributed to the increased population of roton excitation modes. Below 1 K, the superfluid fraction comprises over 99% of the total fluid.

We can understand the properties of steady state bulk He II heat transfer in the context of the two-fluid model. Two loss mechanisms contribute to the limits of bulk heat transfer. One is the mutual friction between the two fluid components, and the other is the viscous nature of the normal fluid component. For conductive heat transport in large channels such as those used for superconducting magnets and particle accelerators, the latter effect of mutual friction tends to dominate [115]. In this regime, the heat conductivity function exhibits a maximum at $T = 1.9$ K near the saturated vapor pressure (SVP), although typical large-scale heat exchangers use sub-cooled He II at 1.9 K and 1 atm for two reasons. The first is simply to eliminate risks associated with air in-leaks. The second is that in saturated He II, the bulk liquid can only tolerate temperature excursions up to the local saturation point fixed

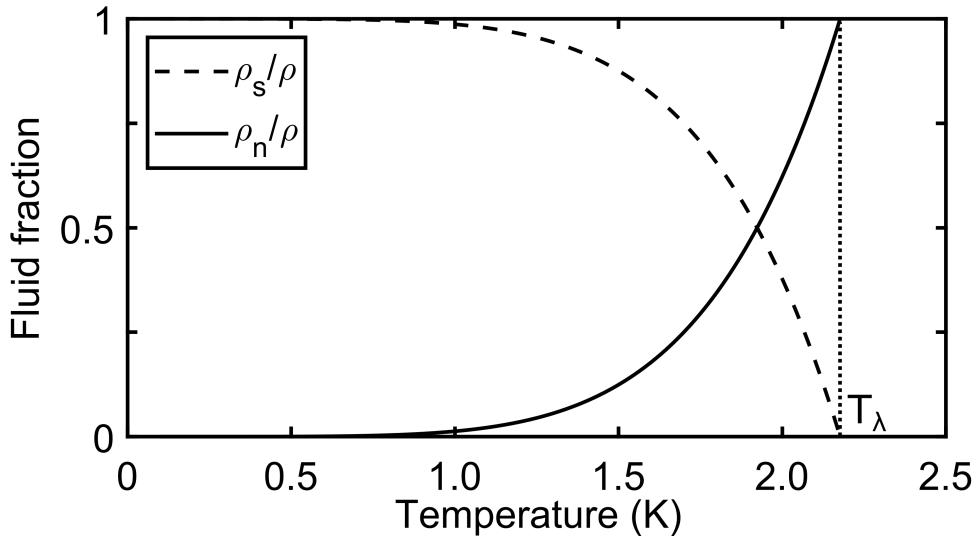

Fig. 1.5: The normal fluid and superfluid fractions comprising a given volume of He II versus temperature. Above T_λ the fluid is entirely in the normal state.

by the pressure in the bulk liquid before boiling occurs. In sub-cooled He II a fixed pressure of, for example, 1 atm allows for temperature excursions all the way up to T_λ, offering a form of cryogenic stabilization [116]. In the experiments presented in this work, we consider only saturated He II due primarily to the fact that it is straightforward to achieve directly via evaporative cooling.

The second loss mechanism, that of turbulence, must be included when considering flow through small channels. Both the superfluid and normal fluid components experience turbulent flow above a critical velocity. In the superfluid, the critical velocity v_c is associated with the minimum energy above which excitations such as rotons and quantized vortices can form and enable dissipative interaction between the fluid and its surroundings [81]. Experimentally, v_c has been observed to vary roughly as $d^{-1/4}$ where d is the characteristic diameter of the transport channel [117]. In the normal fluid the critical velocity is associated with the onset of classical turbulence above Reynolds numbers of approximately 1200 in rigid channels [63].

Figure 1.6 shows both data and modelling of the motion of He II between two volumes connected by a small channel from an unpublished experiment performed by this author. The fluid height in one of the volumes, which was a partially filled 5 GHz quarter-wave tin-plated copper resonator with a quality factor of 3700, a height of 2 cm, and a volume of 175 mm^3 whose frequency change was used to measure the fluid height, is plotted as a time series for different values of bulk liquid temperature at SVP. At time $t = 0$ seconds a pressure was applied by a cylindrical

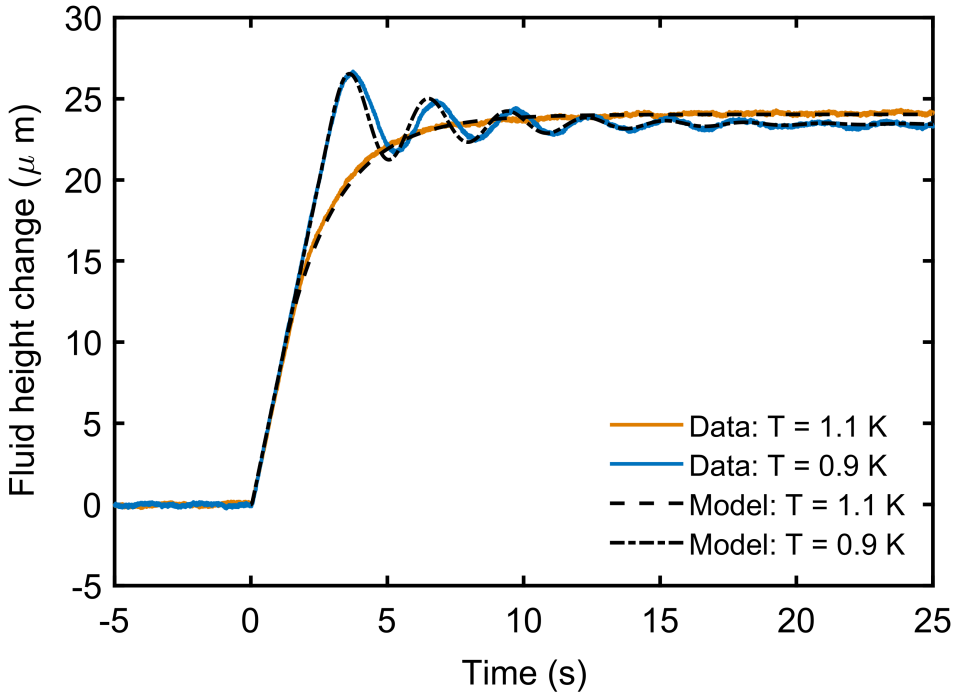

Fig. 1.6: Change in liquid level height versus time of a bath of He II contained in a partially filled quarter-wave resonator connected through a small channel to another volume after a step in pressure is applied at time $t = 0$ s. The data is shown here for He II temperatures of $T = 0.9$ K (blue line) and $T = 1.1$ K (orange line). The model is also shown for $T = 0.9$ K (dash-dotted black line) and $T = 1.1$ K (dashed black line).

capacitor which formed the container for the other volume of fluid and coupled to the liquid through weak dielectric constant of He II to induce mass flow. Before $t = 3$ s, the fluid was constrained by the critical velocity in the channel before the build-up of a temperature gradient caused a counter-flow of mass, exemplifying the interdependence of mass and heat flow in He II. The lag between temperature gradient and mass flow induced mass oscillations between the two volumes, seen in the data at $T = 0.9$ K. Above approximately $T = 1$ K the oscillations become over-damped. Modelling was performed by numerically solving a modified version of Eq. (1.2) while including the limiting critical velocity value of v_c. We note the resemblance to the film-flow trace shown in shown in Fig. 5 of Ref. [118].

In modelling such a system it was necessary to consider how heat was transported not only through the bulk He II, but between the liquid and its containing walls. Careful consideration of this interfacial heat transfer is of critical importance to the work presented in this thesis, where we attempt to use He II to cool the HEMT

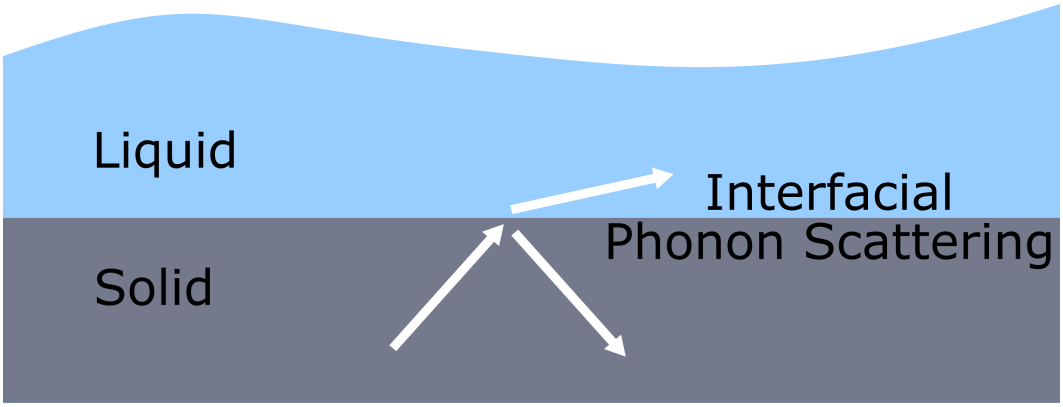

Fig. 1.7: Schematic representation of phonon scattering at the interface between two dissimilar media, in this case between a hot solid and a cool liquid, which resembles the scattering of light between two media of dissimilar indices of refraction.

gate surface. Fundamentally, the thermal boundary resistance arises due to the discontinuity in the thermal environment experienced by the heat-carrying phonons across the boundary. The effect was first observed by Pyotr Kapitza in 1941 [119] and the interfacial conductance is generally referred to as the Kapitza conductance h_K. The first physical predictions of h_K explained the interfacial heat conduction in terms of the phonon radiation on each side of the boundary as predicted by the Debye model, referred to as the "phonon radiation limit" [120, 121]. This description, while capturing the observed $h_K \propto T^3$ dependence, over-predicts the observed values of h_K by more than a factor of 10 because it allows for more heat transfer channels than are physically possible. An advancement to this model was made by Khalatnikov in 1965 [122] and is known as “acoustic mismatch theory.” While fundamentally similar to the phonon radiation limit, acoustic mismatch theory attempts to account for the properties of the materials on both sides of the interface. In particular it accounts for the finite reflection coefficient in a similar manner as in photon reflection between two dissimilar optical media, as shown schematically in Fig. 1.7. Particular to heat transfer between a solid surface and He II, it also accounts for the fact that transverse phonon modes cannot exist in the liquid. While believed to be the correct physical interpretation, acoustic mismatch theory tends to under-predict the measured h_K by a factor of nearly 20. Furthermore, neither the phonon radiation limit nor acoustic mismatch theory correctly predict the observed $h_K \propto T_D^{-1}$ dependence on the solid Debye temperature T_D, with the former predicting $h_K \propto T_D^{-2}$ and the latter predicting $h_K \propto T_D^{-3}$.

Further complications arise in the case where the solid surface is sufficiently hot

such that the local He II in its vicinity exceeds T_λ. This heat transfer regime is known as the "film-boiling" regime where several phases of helium can coexist and contribute to the film-boiling heat conductivity h_{fb}. Given the elevated HEMT gate temperatures of ~ 20 K predicted to occur in the experiments presented in this thesis, if the conductive heat flux due to phonon radiation is insufficient to reduce the He II temperature in the vicinity of the gate below T_λ then film-boiling heat transfer will necessarily occur. There are three cases two consider. The first is where the local pressure at the heated surface remains below the SVP at T_λ, referred to as the saturation boiling condition. In this case both He II liquid and helium vapor coexist in the vicinity of the surface. The second is where the local pressure exceeds the SVP at T_λ. If the heat flux does not exceed the critical heat flux in He I, then a film of He I will form in which heat transfer occurs via nucleate boiling, and bulk heat conduction occurs in the He II. Otherwise, there will be a coexistence of He II, He I, and vapor at the heat transfer interface. The third case occurs in sub-cooled He II, where again a coexistence of three phases can occur [63].

The film-boiling heat transfer regime, even for the simplest case of only a two-phase coexistence of He II and vapor, remains the least well understood. The simplest physical model, presented in Ref. [63], assumes a stable vapor film of constant thickness covering the heat transfer surface, where heat transported through the vapor film occurs by thermal conduction only. The variation in h_{fb} with diameter of a heated wire predicted by this model tends to agree with experiment; see for example Fig. 7.42 of Ref. [63]. An alternative to this model presented in Ref. [123] is to assume that the heat flux through the surface of the vapor film is equal to the bulk He II heat conduction, and that the vapor film thickness increases to limit the heat flux, a trend which is also borne out by experiment [124]. Yet another alternative theory suggested in Ref. [125] uses molecular kinetic theory and treats film boiling as a non-equilibrium process involving heat and mass transfer at the vapor-He II interface. This theory predicts a minimum heat flux necessary to establish a stable vapor film which is less than the critical heat flux predicted by assuming a temperature excursion above T_λ, as was done previously. One way to reconcile these two pictures is to treat the latter as the peak heat flux required to establish a vapor film, and the former as the "recovery" heat flux which must be subceeded to return to the non-boiling regime [126]. In all cases of film-boiling heat transfer, the heat transfer coefficient h_{fb} is typically 10–100 less than h_K, although h_{fb} is strongly dependent on a number of parameters such as heat surface configuration, bath temperature and pressure, and immersion depth.

We now make some preliminary estimates of the heat flow $\dot{Q} = hA\Delta T$ that is expected between a submerged HEMT gate surface and a He II bath, where h is the heat transfer coefficient, A is the heat transfer surface area, and ΔT is the temperature difference across the interface. We take the heat transfer surface area to be approximately that of the gate head in our device, 1 μm $\times$ 200 μm. In the regime of the phonon radiation limit, we take h_K = 5.7 kW m^{-2} K^{-1} which is the measured value of the Kapitza conductance for SiO_2 (taken from the compiled data in Table 2 of Ref. [121]) and ΔT = 0.5 K as a representative value of the temperature difference in the case of non-boiling heat transfer. Using these values, we estimate $\dot{Q}_K$ = 0.6 μW. In the film-boiling regime, we take h_{fb} = 1 kW m^{-2} K^{-1} as a representative value for heat transfer between He II and flat surfaces (taken from the compiled data in Table 7.5 of Ref. [63]), and ΔT = 10 K as a representative value of the temperature difference if the He II is able to measurably decreases the surface temperature. Using these values, we estimate $\dot{Q}_{fb}$ = 2 μW. Although both estimates $\dot{Q}_K$ and $\dot{Q}_{fb}$ predict heat flows which are several orders of magnitude below the milliwatts of dissipated heat required to optimally bias the device, we note that considerable uncertainty exists in these predictions owing to the complexity of the heat transfer process in both the film-boiling and phonon radiation regimes and its dependence on the surface conditions, as well as the appropriate choice for the effective area of heat transfer given the mushroom-shaped HEMT gate head and the SiN passivation layer covering the device. We therefore expect our estimates to give at best an order-of-magnitude indication of the heat flux. We also note that the observed increase in heat transfer coefficients with decreasing heat transfer surface size (see Fig. 11 from Ref. [124], for example) lends support that observing a cooling effect in small HEMT geometries may be possible, and perform the experiment designed to conclusively test these predictions, the primary experimental topic of this thesis.

1.4 Outline of thesis

In Chapter 2 we present the experimental apparatus which was constructed to perform microwave noise characterization of a packaged HEMT amplifier submerged in saturated He II, and describe the calibration procedures involved. In Chapter 3 we present the results of the noise measurements and interpret them using a small-signal model of the device. We compare these results with the predictions of a phonon radiation heat conduction model. We find that liquid cryogenic cooling is unable to mitigate self-heating in HEMTs, and discuss the implications of this

finding in the context of prior studies of He II heat transport in both the film-boiling and non-boiling regimes. We also examine the implications for the limits of noise performance in modern HEMT amplifiers using both the Pospiezalski noise model and a phenomenological model of noisy linear amplifiers. Finally, in Chapter 4 we summarize the central findings of our work and identify potential directions for future related research.

Chapter 2

EXPERIMENTAL METHODS: LIQUID CRYOGENIC COOLING OF HEMT AMPLIFIERS

Microwave low-noise amplifiers based on III-V semiconductor high electron mobility transistor technology are a key component of high precision measurements across diverse fields in science and engineering. In this chapter we establish the approach taken in our experiment to mitigate self-heating in HEMTs using liquid cryogenic cooling, in particular He II. We begin with background information on the cold attenuator Y-factor measurement technique used here, before presenting the experimental apparatus design and construction including both the cryogenic vacuum apparatus and the microwave measurement components. We then detail all calibration measurements, both at room temperature and in liquid cryogenic environments, and finish by describing the noise measurement procedure for our device under test (DUT), a common-source two-stage packaged amplifier (model WBA46A, designed by Ahmed Akgiray and detailed further in Ch. 5.1 of Ref. [38]) comprised of OMMIC D007IH metamorphic HEMTs [35], each with a 70 nm gate length and a 4 finger 200 μm width (4f200) double-mushroom gate structure consisting of an InGaAs-InAlAs-InGaAs-InAlAs epitaxial stack on a semi-insulating GaAs substrate with each stage biased nominally identically, using the cold attenuator Y-factor method. An input matching network (IMN) was employed to match the optimal transistor impedance to the 50 Ω impedance of our measurement system over a 4–5.5 GHz bandwidth at cryogenic temperatures. We refer to the device under test using the terms “device”, “amplifier”, “DUT”, and “LNA” interchangeably for the remainder of this work.

2.1 Background theory for cold attenuator Y-factor measurements

Although there are many techniques available to measure noise, by far the most straightforward and commonly used method to measure the noise temperature of a noisy amplifier at cryogenic temperatures is the Y-factor method [127–129]. In this scheme, a noise source with a known noise temperature in the "hot" (noise source turned on) and "cold" (noise source turned off) states is connected to the input of the amplifier, pulsed on and off, and the output noise power in the hot and cold states is

measured. The Y-factor is then defined as:

$$Y = \frac{P_{\mathrm{H}}}{P_{\mathrm{C}}} \tag{2.1}$$

where P_{H} (P_{C}) is the measured noise power with the noise source switched on (off).

Figure 2.1 shows the measured noise powers P_{H} (noise source switched on with noise temperature T_{H}) and P_{C} (noise source switched off with noise temperature T_{C}), plotted as black dots. Also plotted is the line that passes through these two points in the idealized scenario where the DUT has a linear power gain G, all connectors are lossless, and only the amplifier and noise source contribute to the measured noise power. We have also used the definition of noise temperature $T_N = P_N B^{-1} k_{\mathrm{B}}^{-1}$, where P_N is the noise power, B is the measurement bandwidth and k_{B} is the Boltzmann constant. By knowing the slope and y-intercept of the established line along with the definition of the Y-factor, we can readily find the gain G and noise temperature T_{e} of the amplifier as:

$$G = \frac{P_{\mathrm{H}} - P_{\mathrm{C}}}{B k_{\mathrm{B}} (T_{\mathrm{H}} - T_{\mathrm{C}})} \tag{2.2}$$

$$T_{\mathrm{e}} = \frac{T_{\mathrm{H}} - Y T_{\mathrm{C}}}{Y - 1} \tag{2.3}$$

In any real experiment, additional components will contribute to the measured noise. Figure 2.2 shows a schematic of a Y-factor measurement which includes two lossy input components with respective losses L_1 and L_2 and physical temperatures T_{L_1} and T_{L_2}, the DUT with gain G and noise temperature T_{e}, one lossy output component with loss L_3 and physical temperature T_{L_3}, and a noise power detector which we refer to as the "backend" detector, with noise temperature T_{BE}. The first input component and output component represent coaxial cables connecting to the noise source and backend detector. The second input component represents an attenuator with an intentionally higher loss than the input coaxial cable by a factor of approximately 100. For cryogenic noise measurements, this attenuator is useful in that its temperature can be more easily manipulated and measured in order to dominate over the relative noise contribution of the coaxial cables. The use of such an attenuator is known as the "cold attenuator" Y-factor method [130]. In this scheme, again using the definition of noise power in terms of noise temperature, one

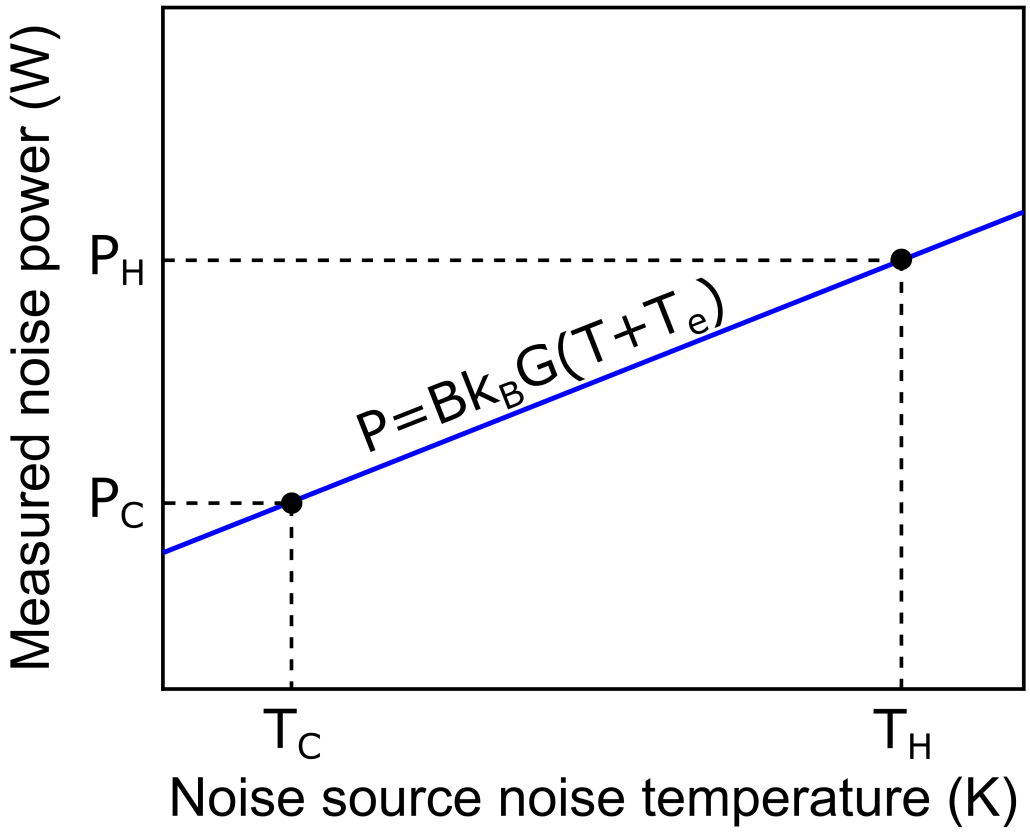

Fig. 2.1: Diagram of measured noise power versus noise source noise temperature in the Y-factor measurement scheme.

can write the measured hot and cold noise powers as:

$$\frac{P_{\mathrm{H}}}{Bk_{\mathrm{B}}} = \left(T_{\mathrm{H}} \frac{G}{L_1 L_2 L_3} + T_{L_1} \frac{G(L_1 - 1)}{L_1 L_2 L_3} + T_{L_2} \frac{G(L_2 - 1)}{L_2 L_3} + T_e \frac{G}{L_3} + T_{L_3} \frac{(L_3 - 1)}{L_3} + T_{\mathrm{BE}} \right) \tag{2.4}$$

$$\frac{P_{\mathrm{C}}}{Bk_{\mathrm{B}}} = \left(T_{\mathrm{C}} \frac{G}{L_1 L_2 L_3} + T_{L_1} \frac{G(L_1 - 1)}{L_1 L_2 L_3} + T_{L_2} \frac{G(L_2 - 1)}{L_2 L_3} + T_e \frac{G}{L_3} + T_{L_3} \frac{(L_3 - 1)}{L_3} + T_{\mathrm{BE}} \right) \tag{2.5}$$

where each term in Eqs. (2.4) and (2.5) represents the noise power added by successive elements in the measurement chain shown schematically in Fig. 2.2. We have also used the fact that the input-referred noise temperature T_{in} of a matched attenuator with loss L and physical temperature T_L is given by $T_{\mathrm{in}} = (L - 1)T_L$ as derived in Ref. [128].

By plugging Eqs. (2.4) and (2.5) into Eq. (2.1) and solving for T_{e} we arrive at the

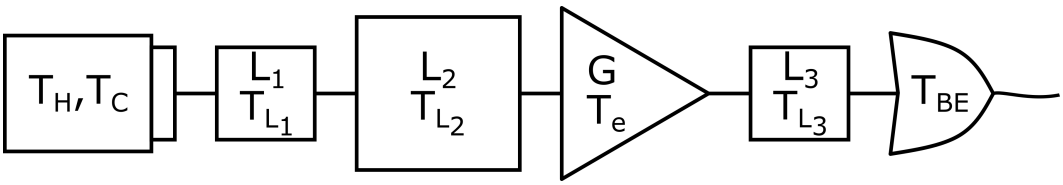

Fig. 2.2: Schematic of the cold attenuator Y-factor measurement chain. From left to right the components are: Noise source with hot (cold) noise temperature T_{H} (T_{C}), input coaxial cable with loss L_1 and physical temperature T_{L_1}, attenuator with loss L_2 and physical temperature T_{L_2}, DUT with gain G and input-referred noise temperature T_{e}, output coaxial cable with loss L_3 and physical temperature T_{L_3}, and backend noise power detector with input-referred noise temperature T_{BE}.

following expression for the DUT noise temperature:

$$T_{\mathrm{e}} = \frac{1}{L_1 L_2}\left[\frac{T_0 E}{Y-1} - T_{\mathrm{C}} - T_{\mathrm{coax}}(L_1-1) - T_{L_2}(L_2-1)L_1 - \frac{T_{\mathrm{coax}}(L_3-1)}{G_{\mathrm{full}}L_3} - \frac{T_{\mathrm{BE}}}{G_{\mathrm{full}}}\right] \quad (2.6)$$

where we have defined $E = (T_{\mathrm{H}} - T_{\mathrm{C}})T_0^{-1}$ to be the excess noise ration (ENR) of the noise source where $T_0 = 290K$, and we have assumed that the input and output coaxial cable temperatures are equal so that $T_{\mathrm{coax}} = T_{L_1} = T_{L_3}$. We have also defined $G_{\mathrm{full}} = GL_1^{-1}L_2^{-1}L_3^{-1}$ to be the the total gain from the input plane of the input coaxial cable to the output plane of the output coaxial cable, which is a useful change of variables since G_{full} is the only gain which can be directly measured in this configuration without disconnecting any coaxial components. We can also subtract Eq. (2.4) from Eq. (2.5) to find an expression for the DUT gain:

$$G = \frac{L_{\mathrm{coax}} L_2 (P_{\mathrm{H}} - P_{\mathrm{C}})}{B k_{\mathrm{B}} T_0 E} \quad (2.7)$$

where we have defined $L_{\mathrm{coax}} = L_1 L_3$ to be the total loss of the coaxial cables.

In order to make gain and loss measurements with the highest possible precision, it was necessary to use a Vector Network Analyzer (VNA). These instruments are capable of fully characterizing multi-port networks by determining their scattering matrix (S-matrix) $\mathbf{S}$, consisting of scattering parameters (S-pars) $S_{ij} = V_i^-/V_j^+$, by driving port j with an incident wave of voltage V_j^+ and measuring the scattered wave at port i of voltage V_i^-. In particular, a two-port network can be fully characterized by the parameters S_{11}, S_{12}, S_{21}, and S_{22}. Of special interest for our purposes is that the power gain G (loss L) of a two-port device is given by $G = |S_{21}|^2$ ($L = |S_{21}|^{-2}$), and the complex reflection coefficient between the device and a component connected to the input of the device is given by $\Gamma = S_{11}$. A more complete treatment of microwave network analysis can be found in Chapter 4 of Ref. [131]. Unless

specified otherwise, all loss and gain measurements shown in this work were taken using a Rhode & Schwarz RSZVA50 VNA calibrated with a Maury 8050CK20 SOLT calibration kit, calibrated at most 24 hours before each measurement. The uncertainty in any gain or loss measurement using this instrument was estimated to be ±0.01 dB, given by the magnitude of the variation in the measured gain or loss versus frequency of the calibration cable immediately after calibration.

With this in mind, we outline a method of transferring the high-precision calibration of the VNA over to any noise power detector. We first note from Eq. (2.7) that so long as the quantity $(Bk_\mathrm{B}T_0E)^{-1}$ is constant (which is a reasonable assumption over the timescale of a Y-factor measurement using stable filters and a stable noise source), then the ratio $G_\mathrm{full}(P_\mathrm{H} - P_\mathrm{C})^{-1}$ is also constant. Thus by fixing the gain at some arbitrary calibration value $G^\mathrm{cal}_\mathrm{full}$, which can be measured with the VNA, and then measuring the corresponding hot and cold noise powers $P^\mathrm{cal}_\mathrm{H}$ and $P^\mathrm{cal}_\mathrm{C}$ with the noise power detector, any other gain G_full can be determined by measuring only P_H and P_C and using the following equation, derived by from Eq. (2.7) and the above considerations:

$$G = \frac{P_\mathrm{H} - P_\mathrm{C}}{P^\mathrm{cal}_\mathrm{H} - P^\mathrm{cal}_\mathrm{C}} G^\mathrm{cal}_\mathrm{full} L_\mathrm{coax} L_2 \tag{2.8}$$

One subtlety to note is that in the derivations of T_e and G, it was assumed that all components are perfectly impedance matched so that the reflection coefficients $\Gamma_{ij} = (Z_i - Z_j)(Z_i + Z_j)^{-1}$ between components i and j with complex impedances Z_i and Z_j are zero. In any real experiment, all microwave components are generally manufactured with a consistent nominal impedance Z_0 ($Z_0 = 50\ \Omega$ in our experiment) so that the mismatch between components is small enough that negligible error is introduced. The exceptions are the low-noise amplifiers themselves which typically have a relatively poor impedance match over a given bandwidth, and the noise source which has an impedance that changes between the hot and cold states. If the noise source impedance changes significantly relative to the impedance of the component connected to its output, the error introduced into the propagated power will be significant. If the S-pars of all components including the noise source in the hot and cold states are known, then this error can be corrected. The correction algorithm is derived and demonstrated in Appendix A. Unless otherwise stated, this correction was not used for data shown in this work since the impedance match between the noise source and input coaxial cable was found to be sufficiently good so as to introduce negligible uncertainty to the measurements.

Another subtlety of note is the distinction between representation of units in their linear form (such as V, W, etc.) and in their logarithmic form (such as dB, dBV, dBm, etc.). Unless otherwise stated, all units are assumed to be in their linear representation and any logarithmic representation uses the "power ratio" definition $P_{\mathrm{dB}} = 10\log_{10}(\frac{P}{P_0})$ so that $V_{\mathrm{dB}} = 20\log(\frac{V}{V_0})$. Furthermore, for error propagation purposes it is useful to be able to convert uncertainties between their linear and logarithmic representations. For a quantity X with uncertainty ΔX with logarithmic representation X_{dB} and logarithmic error ΔX_{dB} this can be done using the following equations:

$$\Delta X = 10^{\frac{X_{\mathrm{dB}}}{10}}(10^{\frac{\Delta X_{\mathrm{dB}}}{10}} - 1) \tag{2.9}$$

$$\Delta X_{\mathrm{dB}} = 10\log_{10}\left(1 + \frac{\Delta X}{X}\right) \tag{2.10}$$

Finally, it is also useful to write the measured Y-factor explicitly as a time-series in terms of the measured voltages $V_{\mathrm{H},k}$ and $V_{\mathrm{C},k}$ output by the backend detector at time index k. We assume the tunnel diode detectors linearly transduced the noise power with some power-to-voltage gain $\mathrm{K_D}$ and with a zero-power offset voltage $V_{0,k}$ so that $V_{\mathrm{H},k} = \mathrm{K_D}P_{\mathrm{H},k} + V_{0,k}$ and $V_{\mathrm{C},k} = \mathrm{K_D}P_{\mathrm{C},k} + V_{0,k}$ at time index k, which is the expected behavior for microwave power tunnel diode detectors operating in the square-law regime [132, 133]. The voltage data was analog filtered and over-sampled at f_{s} to avoid aliasing artifacts. We emphasize here that there is a trade-off between the faster response time offered by tunnel diode detectors versus the improved stability offered by commercial power sensors. We enhanced the stability of our diode detectors by re-measuring the zero-power offset voltage at a frequency $f_0 \gg f_{\mathrm{ENR}}$ for a duration $t_0 = D f_{\mathrm{ENR}}$ to correct for DC offset drifts, where D was the duty cycle of the recalibration pulse. The noise source was pulsed at a frequency f_{ENR}, and each half-pulse of hot (cold) voltage data was integrated for its duration $t_{\mathrm{ENR}} = 0.5 f_{\mathrm{ENR}}^{-1}$. The integrated zero-power offset was subtracted from each integrated hot (cold) half-pulse to give hot (cold) offset-corrected data $V'_{\mathrm{H},p}$ ($V'_{\mathrm{C},p}$) for each pulse p. This procedure yielded Y-factor data effectively sampled at f_{ENR} with t_0 seconds of data skipped every calibration cycle. The expression for the measured Y-factor for pulse p considering the above specifications is:

$$Y_p = \frac{N_{\mathrm{HC}}^{-1}\left(\sum_{k=k_{\mathrm{H},p}}^{k_{\mathrm{HC},p}} V_{\mathrm{H},k}\right) - N_0^{-1}\left(\sum_{k=0}^{k_0} V_{0,k}\right)}{N_{\mathrm{HC}}^{-1}\left(\sum_{k=k_{\mathrm{HC},p}}^{k_{\mathrm{C},p}} V_{\mathrm{C},k}\right) - N_0^{-1}\left(\sum_{k=0}^{k_0} V_{0,k}\right)} = \frac{V'_{\mathrm{H},p}}{V'_{\mathrm{C},p}} \tag{2.11}$$

where $N_0 = t_0 f_s$ is the number of sampled points in each calibration pulse, $N_{HC} = f_s t_{ENR}$ is the number of sampled points in each half-pulse, $k_{H,p} = (k_0 + 1) + 2(p - 1)N_{HC}$ is the time index at the start of the pth hot pulse, $k_{HC} = k_{H,p} + N_{HC}$ is the time index at the center of the pth pulse when the noise source switches from hot to cold, and $k_{C,p} = k_{H,p} + 2N_{HC}$ is the time index at the end of the pth cold pulse.

2.2 Experimental apparatus overview

In order to measure the noise of the HEMT LNA when submerged in He II, a microwave noise characterization apparatus was designed and constructed around the principle of dipping the LNA directly into the liquid bath of a commercially available liquid helium transport dewar, and evaporatively cooling this bath to reach temperatures below the helium-4 lambda point. A schematic of the experimental design which is an adaption of the cold attenuator Y-factor method with the inclusion of a liquid helium bath surrounding the DUT and attenuator is shown in Fig. 2.3(a). The apparatus consisted of: a 15 dB ENR 2-18 GHz solid state packaged noise diode to generate noise power, stainless steel coaxial cabling to carry noise power between the room temperature and cryogenic components, a 20 dB packaged chip attenuator and LNA under test mounted to a copper mounting stage, and a room temperature noise power detector. Further details of the cryogenic components and the noise power detector are provided in Sections 2.3 and 2.4, respectively. Representative output noise power voltage data is shown as a time series in Fig. 2.3(b) where the data was analog-filtered at 1 kHz and over-sampled at $f_s = 1.1$ kHz, and the measurement parameters were $f_{ENR} = 10$ Hz, $f_0 = 1$ Hz, and $D = 0.1$. The first and last half-pulses of each cycle were discarded due to the 20 ms switching time of the microwave switch used for recalibration, yielding 8 total pulses. Unless otherwise indicated, these parameters were used for all subsequent measurements. For all steady-state data the Y-factor was further averaged over a total measurement time $t_{fin} = 4$ s.

2.3 Cryogenic engineering

Figure 2.4 shows an image of the mounted vacuum apparatus, which was helium leak-tested at room temperature on an empty 60 L Cryofab liquid helium transport dewar with a Pfeiffer SmartTest HLT 550 leak detector. A conical 2.5" Tri-Clamp to KF-40 adapter was used to seal directly to the dewar. A 6-way KF-40 cross adapter was used to attach the necessary vacuum fittings. These vacuum fittings consisted of the following: (1) MKS 901P loadlock transducer to measure absolute pressure

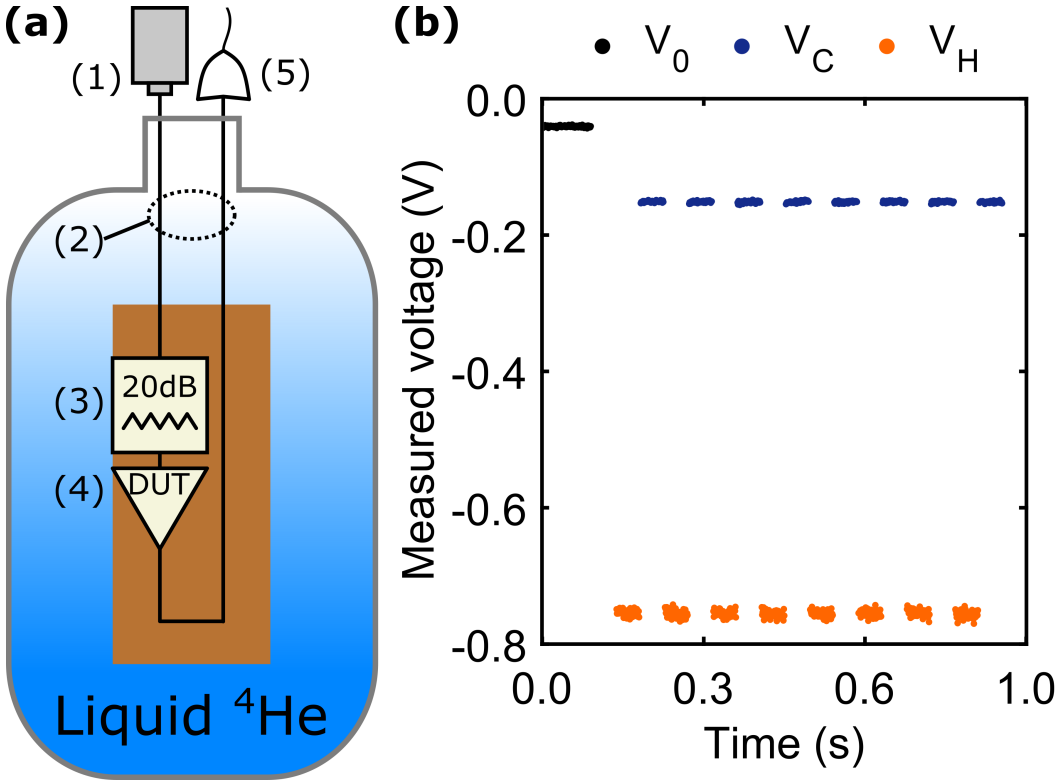

Fig. 2.3: **(a)** Schematic of the measurement apparatus inside a liquid helium-4 dewar, including the following components: (1) 15 dB ENR 2-18 GHz solid state SMA packaged noise diode biased at 28 V through a MOSFET amplifier circuit (not shown); (2) input and output silver-plated stainless steel SMA coaxial cables each 1.3 m in length; (3) 20 dB packaged cryogenic chip attenuator with factory calibrated DT-670-SD diodes mounted directly on the attenuator substrate; (4) packaged WBA46A LNA; (5) backend noise power detector. **(b)** Representative raw Y-factor data versus time. The diode detector DC offset voltage V_0 (black lines), hot voltage V_H (orange lines), and cold voltage V_C (blue lines) are all shown.

from 1 atm down to $\sim 10^{-5}$ Torr; (2) leak-tight cryogenic 20 PSI pressure-relief valve for safe release of helium pressure buildup in the event of a power failure to the pumping system; (3) KurtLesker inline bellows valve connecting to an ultra high purity helium-4 gas supply to control the back-filling rate of helium gas, with inlet pressure measured by a Bourdon tube mechanical pressure gauge; (4) pumping line connection consisting of a KurtLesker inline bellows valve for flow-rate control in series with a normally-closed Agilent electromagnetically actuated block valve to prevent back-filling of air in the event of power failure to the pumping system, which was comprised of a Leybold DK-50 rotary piston vacuum pump (50 m^3 h^{-1} pumping speed) in parallel with an Anest Iwata ISP-500B dry scroll vacuum pump (35 m^3 h^{-1} pumping speed) each outfitted with one-way valves on their outlet ports to further

protect from back-filling with air; (5) vertically mounted KF-40 straight connector tube to extend the height of the vacuum fitting to match the length of the stainless steel coaxial cables used in the experiment, which connected to two conical KF-40 to KF-50 reducing adapters connected in series to provide enough space for stress-relief loops in the coaxial cabling, and then to a KF-40 to 4-1/2" UHV CF flange which was sealed with an OFHC copper gasket to a custom machined 4-1/2" UHV CF flange electronics breakout fitting with hermetically sealed SubMiniature-A (SMA) and DC feedthroughs; (6) rubber coated nickel-alloy heater tape with adjustable temperature control, which was wrapped around the flanges that were in direct contact with the helium pumping path, in order to maintain temperatures above the leak-tight temperature tolerance of the O-rings during pumping. The conical reducing adapters and custom hermetic breakout panel are shown in Fig. 2.5, with the 4" long input and output coaxial cable leads connecting to SMA test cables via inner-outer DC blocks which defined the reference plane for all subsequent microwave measurements, and a 24-wire DC cable connected to the vacuum feedthrough which enabled DC electrical connections between room temperature electronics and cryogenic components inside the dewar. The Tri-Clamp O-ring was made from PTFE which is rated leak-tight to $-100\,^{\circ}\mathrm{C}$, and all KF O-rings were made from silicone which is rated leak-tight to $-60\,^{\circ}\mathrm{C}$.

Inside the vacuum space, a thin-walled (1.250" outer diameter, 1.084" inner diameter) 304 stainless steel tube was used as a dipstick to submerge the DUT into the helium-4 bath. Figure 2.6 shows the OFHC copper stage which was machined using a TREE vertical milling machine in the Jim Hall Design and Prototyping Lab at Caltech, and screw-mounted to the dipstick. The DUT, cold attenuator, two Lake Shore DT-670-CU temperature diodes, and a heater (mounted behind the stage and not shown) were screw-mounted to the stage using indium foil as an inter-facial layer to promote thermalization between the components and the stage. An American Magnetics liquid helium level sensor calibrated for 4.2 K liquid was taped to the interior wall of the dipstick using kapton tape, with the bottom of the sensor sitting 1 cm above the top of the mounting stage. This sensor was primarily used to ensure consistent starting heights across different liquid helium dewars. The fluctuations in the readings of the temperature diodes mounted on the copper stage were used to approximate the liquid level when the bath was in the superfluid state. An improvement to this design would be to use a liquid level sensor calibrated to the operating temperature of the superfluid bath, and to mount the sensor so that the bottom of the sensor and the bottom of the mounting stage are level. Noise

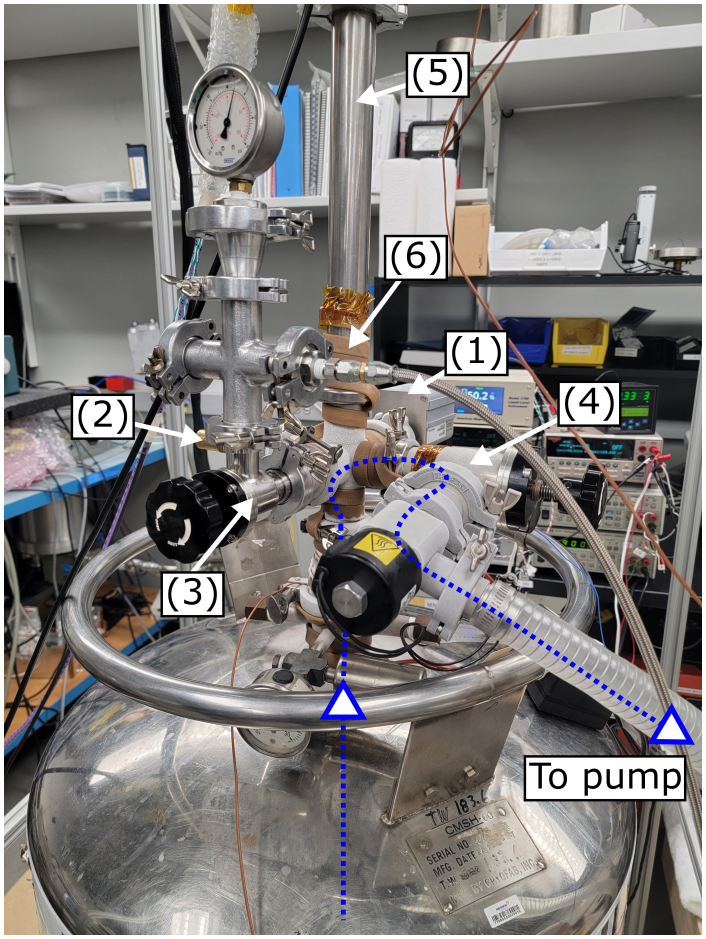

Fig. 2.4: Image of the vacuum apparatus mounted to a liquid helium dewar with the following components: (1) pressure transducer; (2) leak-tight cryogenic pressure-relief valve; (3) bellows valve connecting to an ultra high purity helium-4 gas supply; (4) pumping line connection consisting of a bellows valve for flow-rate control in series with a normally-closed electromagnetically actuated block valve; (5) vertically mounted straight connector tube; (6) heating tape. The helium flow path induced by pumping is shown as a blue dashed line, and frosting of condensation on the exterior walls of the vacuum components along this path can be seen.

power was directed to and from the attenuator and DUT through 1.3 m long 0.141" diameter low-loss silver-plated stainless steel SMA coaxial cables, which were connected to the hermetic SMA feedthrough via 0.3 m long copper-braided SMA flex cables, each with one stress relief loop. The output cable was connected to the DUT output through two SMA flex cables, which were included in the loss calibration measurement of the cabling. DC signals were carried by phosphor-bronze cryogenic wires manufactured by Lake Shore Cryotronics.

Since the experimental procedure required evaporatively cooling a relatively large

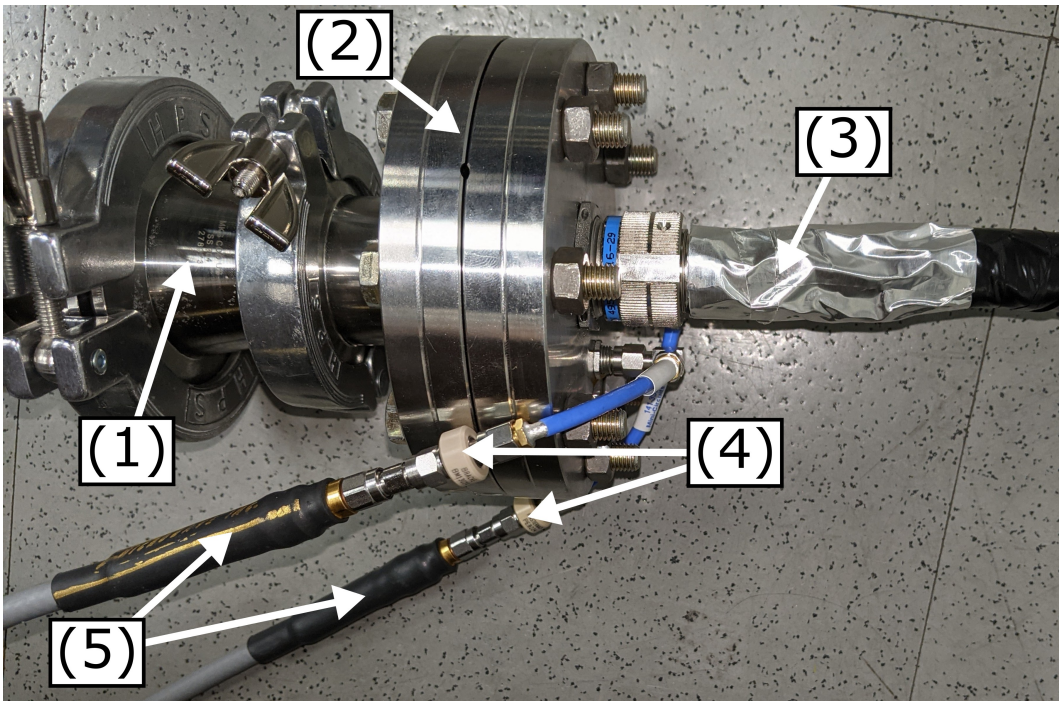

Fig. 2.5: Image of the hermetic breakout flange with the following labeled components: (1) conical reducing adapter; (2) CF flange with hermetic breakouts; (3) DC cable; (4) input and output inner-outer DC blocks terminating the coaxial cable leads; (5) SMA test cables connected to the VNA (not shown). The reference plane for all microwave measurements was the male connector of the inner-outer DC blocks.

quantity of helium liquid, thermal modelling was performed to determine what pumping speed was required so that the evaporative cooling power was sufficient to overcome the heating power of the mounting apparatus, and to ensure that enough liquid would remain to submerge the DUT for the length of time required for Y-factor measurements. Figure 2.7 shows a schematic of the model which includes

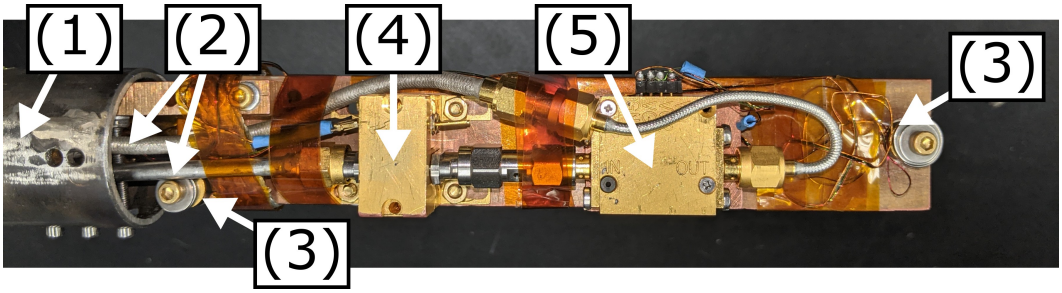

Fig. 2.6: Image of the copper mounting stage with the following labeled components: (1) dipstick; (2) input and output coaxial cables; (3) Lake Shore DT-670-CU temperature diodes; (4) packaged 20 dB cold attenuator; (5) DUT.

the following parameters: the saturated vapor pressure P_{vap}, the liquid helium-4 density $\rho_{4\text{He}}$ and heat capacity $C_{4\text{He}}$, and the enthalpy (latent heat) of vaporization ΔH_{vap}, which all vary with the liquid bath temperature T_{L}; the effective pumping speed $S_{\text{eff}} = \text{C}_{\text{tube}} S(S + C_{\text{eff}})^{-1}$ given the pumping speed S of the pump and the hydrodynamic tubing conductance $\text{C}_{\text{tube}} = 1350 d^4 \bar{P} l^{-1}$ where $d = 2.64$ cm is the diameter of standard KF-25 tubing, $l = 1$ m is the approximate length of tubing used here, and $\bar{P} \approx P_{\text{vap}}$ since we have $\text{C}_{\text{tube}} \gg S$ for all pressures measured in this experiment (down to $P_{\text{vap}} = 5.6$ Torr at $T_{\text{L}} = 1.6$ K); the pump inlet pressure and temperature $P_i \approx P_{\text{vap}}$ and $T_i \approx 300$ K; and the external heating $P_{\text{ext}} \approx 100$ mW on the liquid bath carried by both the coaxial cabling and the helium dewar walls, estimated by considering both the average evaporation rate of a liquid helium transport dewar of 1 liter/day and the contributions from the coaxial cabling connecting the 300 K breakout flange to the liquid bath. By using the fact that both the total helium-4 mass and energy are conserved along with the above specifications, we arrive at the following differential equations for the liquid bath temperature T_{L} and volume V_{L}:

$$\frac{\text{d}V_{\text{L}}}{\text{d}t} = -\frac{P_{\text{vap}}(t) S_{\text{eff}} M_{4\text{He}}}{R T_{\text{L}}(t) \rho_{4\text{He}}(t)} \tag{2.12}$$

$$\frac{\text{d}T_{\text{L}}}{\text{d}t} = -\frac{M_{4\text{He}}}{C_{4\text{He}}(t) \rho_{4\text{He}}(t) V_{\text{L}}(t)} \left(\frac{P_{\text{vap}}(t) S_{\text{eff}} \Delta H_{\text{vap}}(t)}{R T_{\text{L}}(t)} - P_{\text{ext}} \right) \tag{2.13}$$

where $M_{4\text{He}} = 4$ g mol^{-1} is the molar mass of helium-4 and $R = 8.31$ J (mol K)$^{-1}$ is the gas constant. All temperature dependent helium-4 quantities were taken from the compiled data in Ref. [104].

Equations (2.12) and (2.13) were solved using the ode45 differential equation solver in MATLAB. Figure 2.8(a) shows the modelled bath temperature versus time for various pumping speeds. The cooling speed from a starting bath temperature of 4.2 K down to 2.5 K happens relatively quickly, taking less than 3 hours for a modest pumping speed of 15 m^3 h^{-1}. The cooling slows drastically as the temperature crosses the lambda point where the heat capacity increases, and then speeds up again as the heat capacity comes back down. The critical pumping speed, below which the evaporative cooling power is insufficient to ever achieve bath temperatures below T_λ, is around 2 m^3 h^{-1}, although pumping speeds of 25 m^3 h^{-1} and above are required in order to achieve stable base temperatures below T_λ in less than one day of pumping. Furthermore, a high throughput pump is required to move the significant mass of helium-4 vapor over the first several hours of pumping. This can be seen in Fig. 2.8(b) which shows the volume of remaining liquid versus time, and suggests

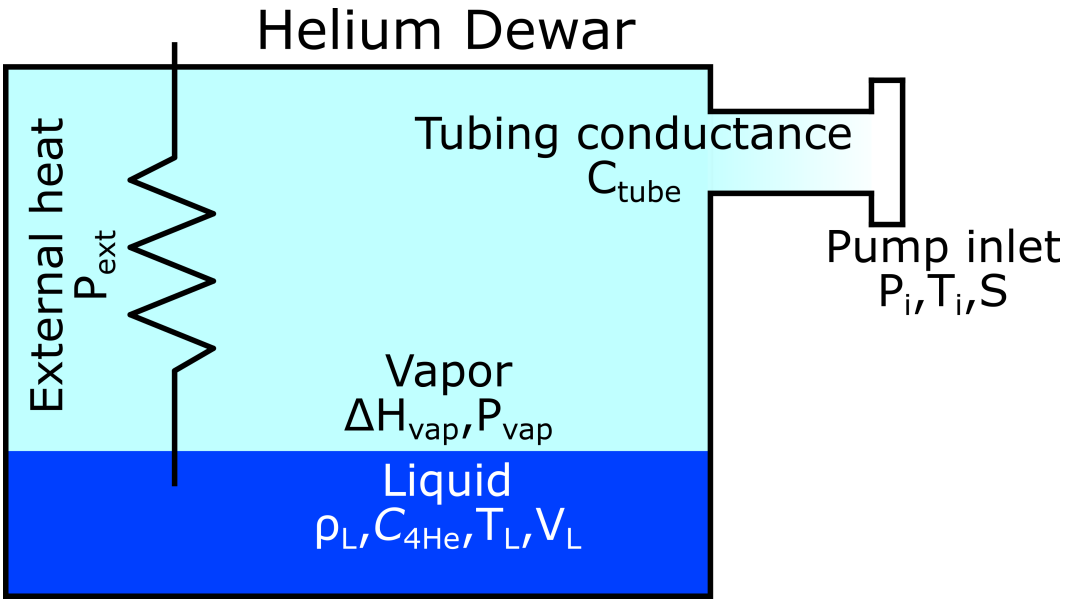

Fig. 2.7: Schematic of the liquid helium-4 dewar pumping model which includes the pumping speed S, the hydrodynamic tubing conductance C_{tube}, the pump inlet pressure and temperature P_i and T_i, the external heating P_{ext} on the liquid bath and the temperature dependence of the saturated vapor pressure P_{vap}, liquid helium-4 density ρ_{4He}, heat capacity C_{4He}, and the enthalpy of vaporization ΔH_{vap}

that at least 20 L of liquid, which weighs 2.5 kg, must be removed. Since the rate of liquid volume change decreases as the vapor pressure decreases with decreasing temperature, Fig. 2.8(b) also suggests that even for relatively fast pumping speeds the liquid volume will last for at least several days, an expectation which was indeed borne out in the experiment.

Also shown in Fig. 2.8(a) is the measured bath temperature over the first 5 hours of pumping during a cooldown. For the first 1.3 hours only the more powerful Leybold DK-50 rotary piston pump was used to move the bulk of the helium, and the pumping speed was throttled manually by adjusting the bellows valve in order to minimize frosting of the O-rings while the helium vapor density was still high enough to significantly cool the vacuum tubing, with adjustments of the throttling seen as kinks in the cooling curve. After 1.3 hours the valve was fully opened, and after another 20 minutes the Anest Iwata ISP-500B dry scroll pump was engaged, as seen by the kink in the cooling curve at 1.6 hours. After this, the pumping occurred at a rate of approximately 60 $m^3\ h^{-1}$, estimated by comparison with the modelled curve, with the pumping rate decreasing with decreasing temperature. This pumping speed is less than the highest rated pumping speed of the two pumps when added in parallel ($50 + 35 = 85\ m^3\ h^{-1}$), which is expected when considering the reduction

in rated pumping speed associated with reduced pump inlet pressures.

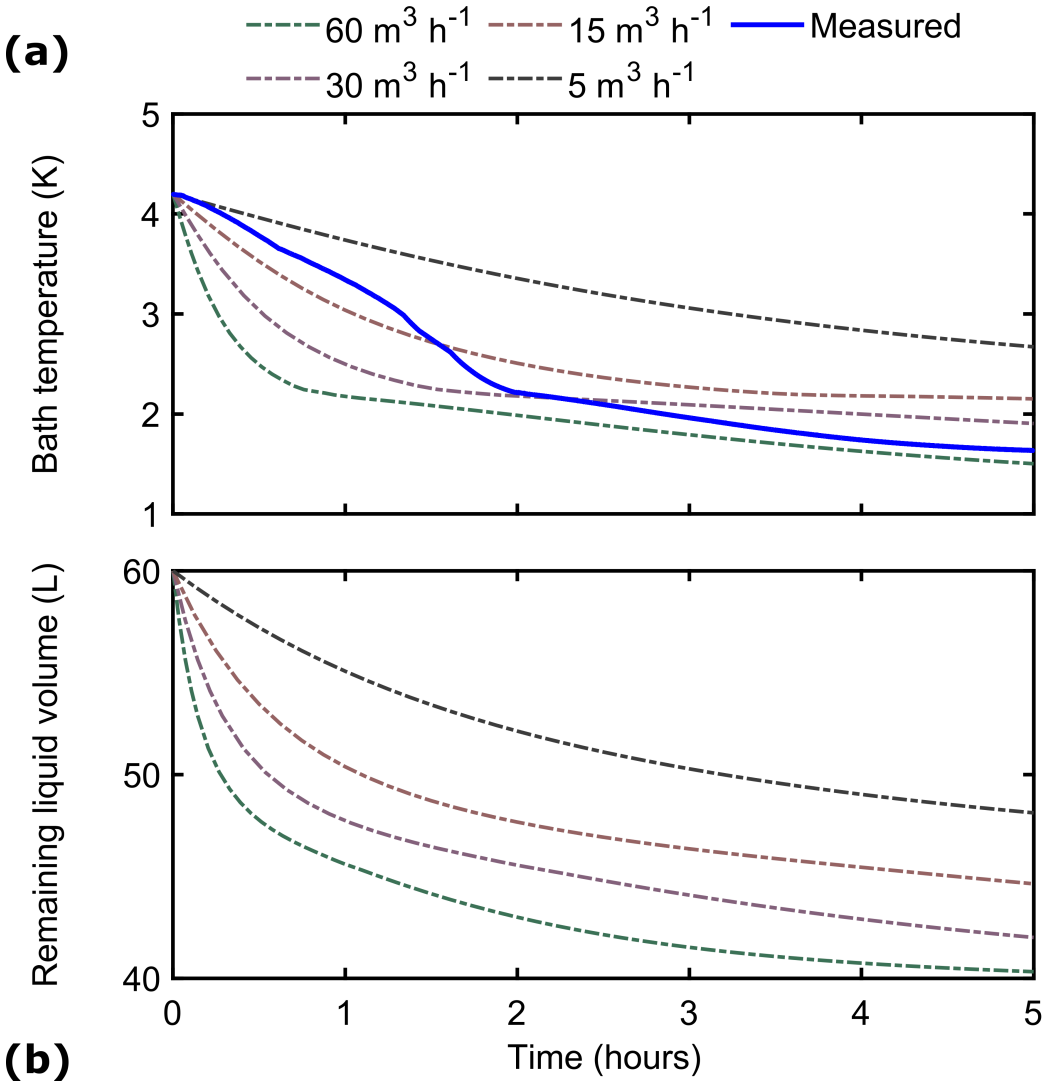

Fig. 2.8: **(a)** Liquid bath temperature versus time. The pumping model solution for T_L is shown for pumping speeds of 60 m^3 h^{-1} (dash-dotted gray line), 30 m^3 h^{-1} (dash-dotted beige line), 15 m^3 h^{-1} (dash-dotted purple line), and 5 m^3 h^{-1} (dash-dotted green line). The measured bath temperature during a dewar cooldown is also shown (solid blue line). **(b)** Remaining liquid volume versus time. The pumping model solution for V_L is shown for the same pumping speeds as in **(a)**.

We conclude this section by noting several design considerations with regards to pumping on the vacuum space of a cryogenic dewar. Firstly, it is critical to ensure that all vacuum fittings are helium leak-tight over the full temperature range they experience while pumping. In our design, the fast moving helium vapor from the dewar space to the pump caused significant forced convective cooling of the vacuum fittings in the pumping line, as evidenced by the frosting visible in Fig. 2.4.

Throttling of the pumping speed was performed to ensure all O-rings stayed within their temperature tolerance. A possible improvement to this design would be to use an inner lining tube along the pumping path to separate the flow of helium from directly contacting the room temperature vacuum fittings, although due to space limitations such a design is difficult to employ in narrow-neck dewars such as the one used in this experiment. Second, a sufficiently strong pump must be employed which can sustain pumping speeds above approximately 25 m^3 h^{-1} at inlet pressures above 10 Torr. It was found that a dry-scroll pump of the type commonly used in low-temperature laboratories was insufficient for this task, necessitating the use of a rotary piston pump or another pump of comparable or greater sustained throughput.

2.4 Device characterization and calibrations at room temperature

The operation of a transistor amplifier requires direct current (DC) voltage biasing of both the drain terminal relative to the source terminal which we denote V_{DS} and the gate terminal relative to the source terminal which we denote V_{GS}. A positive V_{DS} is applied to drive a current I_{DS} along the transistor channel from source to drain, and since the GaAs HEMT transistors used in this work are depletion mode a negative V_{GS} is applied in order for a microwave frequency voltage signal applied to the gate to modulate the conductance of the channel and induce gain. Device bias voltages and currents were generated using Keithley 2400 SourceMeters.

Both DC and microwave characterization of the amplifier were performed at room temperature in order to ensure reasonable device operation. Figures 2.9(a) and 2.9(b) show the DC current-voltage (I-V) data taken over a range of V_{GS} on the first and second amplifier stages, respectively. In order to measure the I-V curve of an individual transistor stage, the other stage was pinched off at $V_{GS} = -8$ V. The plotted V_{DS} is corrected to account for the 44 Ω resistor in series with the drain-source bias line of each transistor as part of the protection circuitry, as are all V_{DS} values reported hereafter. The current density I_{DS} is normalized to the gate periphery of 200 μm. Figure 2.9(c) shows the S_{11} and S_{21} of the LNA measured using the VNA as well as the noise temperature of the LNA measured using an internally calibrated Agilent N8975A noise figure analyzer (NFA) and a N4000A noise source, with the device biased at its low-noise bias of $P_{DC} = 37.1$ mW mm^{-1} at room temperature. The device exhibits a noise temperature minimum of $T_e = 50K$ at a frequency of 4 GHz at room temperature. These characterization measurements suggest a functioning device within the device design parameters, although the differences between Fig. 2.9(a) and Fig. 2.9(b) suggest a slight asymmetry between

the two nominally identical stages.

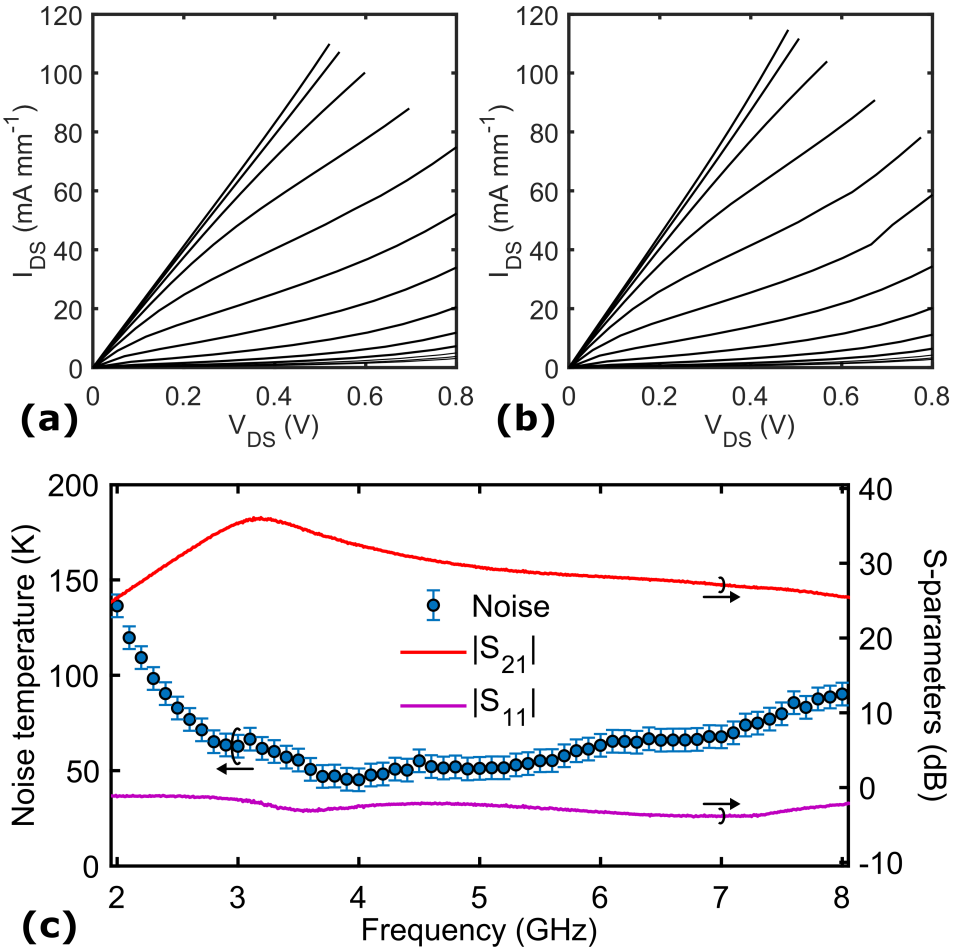

Fig. 2.9: **(a)** I_{DS} versus V_{DS} measured at room temperature with the reverse-bias of the first transistor stage ranging from $V_{GS} = -8$ V to $V_{GS} = -2$ V in 0.5 V steps (black lines from bottom to top) with the second transistor stage pinched off at -8 V. **(b)** I_{DS} versus V_{DS} measured at room temperature with the reverse-bias of the second transistor stage ranging from $V_{GS} = -8$ V to $V_{GS} = -2$ V in 0.5 V steps (black lines from bottom to top) with the first transistor stage pinched off at -8 V. An asymmetry in the IV curves between the two stages can be seen. **(c)** Noise temperature (left axis, blue circles), $|S_{21}|$ (right axis, red line), and $|S_{11}|$ (right axis, magenta line) versus microwave frequency with the device biased at its low-noise bias of $P_{DC} = 37.1$ mW mm^{-}1 ($V_{DS} = 0.85$ V, $I_{DS} = 43.7$ mA, $V_{GS1} = -4.5$ V, $V_{GS2} = -4.9$ V) at room temperature. Noise temperature was measured using a NFA, and S-pars were measured using a VNA.

In order to measure microwave noise power, a backend room temperature microwave power detector was assembled. Figure 2.10 shows a schematic of the backend, which consisted of the following components. Microwave power coupled to the input of the detector first passed through a 3-–6 GHz microwave isolator to improve impedance

matching and minimize reflections. Two Minicircuits ZX60-83LN-S+ broadband amplifiers were placed sequentially following the isolator. A microwave filter was then used to limit the bandwidth of power amplified by the final gain stage, a Miteq AMF-3B-04000800-25-25P power amplifier. Next, a microwave switch was used to periodically switch between the signal path and a 50 Ω load, enabling recalibration of the detector to correct for DC offset drifts. A variable attenuator was then used to set the magnitude of noise power which was then split into two channels, one with a temperature-controlled yttrium iron garnet (YIG) filter with adjustable center frequency, and the other with a fixed Reactel 5 GHz bandpass cavity filter. The latter channel was primarily used for diagnostic purposes. Microwave noise power finally reached the Herotek DT4080 tunnel diode detectors, which linearly transduced this power into a DC voltage. Inner-outer DC blocks were placed at the diode detectors' inputs to eliminate unwanted biasing. The final DC signals were amplified and low-pass filtered by two SRS560 pre-amplifiers and then digitized by a National Instruments NI6259-USB DAQ for further data processing. All data acquisition was controlled via LabVIEW running on a Windows desktop computer, and instrument control was generally performed using the GPIB protocol. All data processing was performed in MATLAB.

Several diagnostic measurements were performed on the backend to ensure appropriate operation of the backend elements. Figure 2.11 shows the magnitude of the $|S_{21}|$ versus frequency of each of the backend filter channels with the YIG filter set at a few different center frequencies. Both filters exhibit reasonable flatness over their 20 MHz bandwidth.

Figure 2.12(a) shows one calibration measurement of the voltage output by the tunnel diode detectors versus incident microwave power, along with a linear fit to the power range 0–4 μW. The diodes exhibit good linearity in this range but deviate from linearity above 5 μW (−23 dBm). Figure 2.12(b) shows another calibration measurement of diode detector voltage output versus incident microwave power with more data taken at lower powers, plotted logarithmically along with a linear fit. Linearity is observed here within measurement error down to −44 dBm (100 nW). The magnitude of incident microwave power was measured using a LadyBug LB5940A TrueRMS power sensor which was connected to the diode detectors via a calibrated microwave power splitter. We find power-to-voltage sensitivities of $K_{\mathrm{YIG}} = 1004$ mV mW^{-1} and $K_{\mathrm{fixed}} = 1111$ mV mW^{-1}, in agreement with the manufacturer reported minimum sensitivity of 900 mV mW^{-1}. A variable attenuator

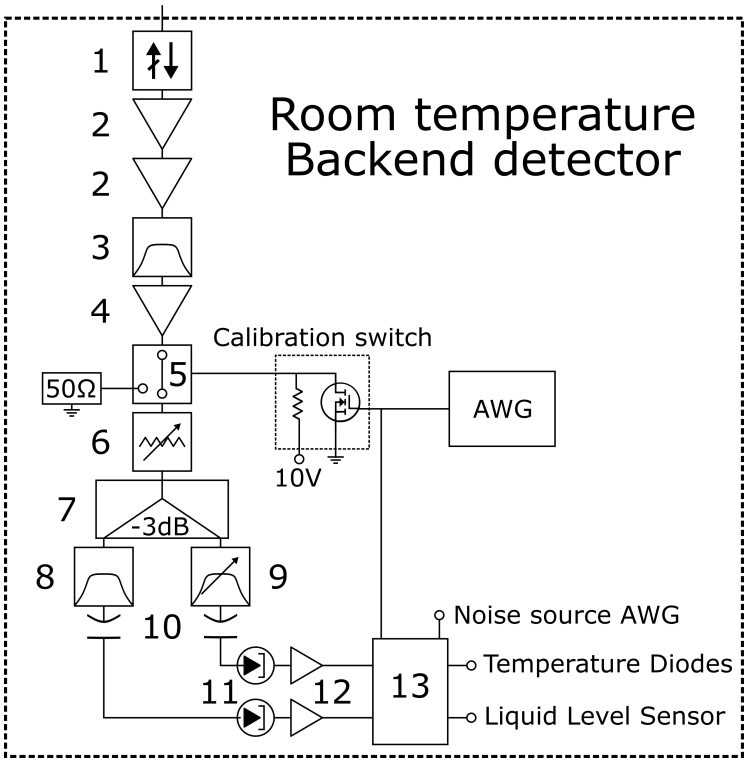

Fig. 2.10: Schematic of the room temperature backend noise power detector consisting of (1) Pasternak PE8327 isolator, (2) Minicircuits ZX60-83LN-S+ low-noise amplifiers, (3) Minicircuits filters with 3-6 GHz bandwidth, (4) Miteq AMF-3B-04000800-25-25P medium power amplifier, (5) RF switch for calibration, (6) 0 – 20 dB variable attenuator, (7) microwave power splitter, (8) Reactel cavity filter with 5 GHz center frequency and 20 MHz bandwidth, (9) Micro Lambda MLFM-42008 20 MHz bandwidth tunable YIG filter, (10) Pasternak PE8224 inner-outer DC blocks, (11) Herotek DT4080 tunnel diode detectors, (12) SRS560 low-noise preamps, (13) National Instruments NI6259-USB DAQ. Also shown is the Agilent 33210A arbitrary waveform generator (AWG) used to pulse the microwave switch MOSFET biasing circuit, as well as the DAQ terminals connecting to the AWG port used to bias the noise source (not shown), temperature diode voltage outputs from the temperature controller, and liquid level sensor voltage output from the American Magnetics 1700 liquid level instrument, enabling synchronous measurement of each component with the noise power data. The losses of the SMA cabling and attenuator pads are not shown.

was used to ensure that the microwave power incident on the diode detectors was between −40 dBm and −24 dBm for all subsequent measurements.

Figure 2.13 shows the Allan deviation of the output of the tunnel diode detectors referred to their input versus integration time τ, measured with an incident microwave power of −100 dBm which is five orders of magnitude below the detectors'

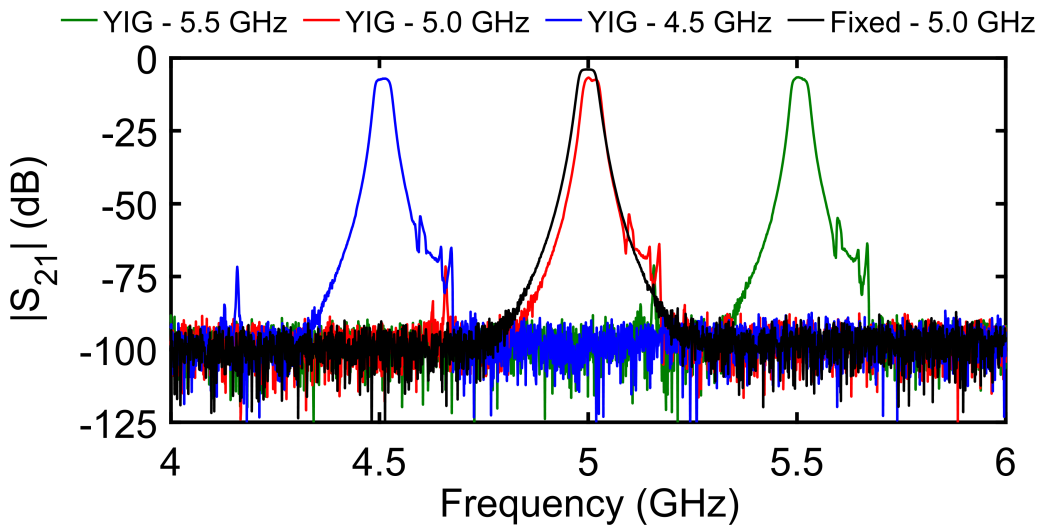

Fig. 2.11: $|S_{21}|$ of the fixed 5 GHz filter channel (black line) and the YIG filter channel with center frequency set to 4.5 GHz (blue line), 5.0 GHz (black line), and 5.5 GHz (red line) versus frequency. The filters exhibit better than ±0.5 dB flatness over their 20 MHz bandwidth. The −100 dB noise floor is set by the VNA noise floor.

manufacturer-reported noise floor of −50 dBm. The voltage was sampled by the DAQ at 500 Hz after being analog-filtered at 1000 Hz and amplified by a factor of 1000 by the SRS560 preamps. This voltage gain was used for all subsequent measurements. Both detectors exhibited a minimum in their Allan deviation of less than 0.1 nW $\mathrm{Hz}^{-1/2}$ at an integration time of approximately 1 s, so a recalibration period of 1 s was chosen for all subsequent measurements. Another minimum in the Allan deviation was observed at 500 s, suggesting the presence of a noise source other than 1/f noise at frequencies between roughly 1 Hz and 2 mHz, although such long integration times are not relevant to our measurements.

In order to ultimately extract T_e, the measurement components corresponding to each term in Eq. (2.6) were calibrated. Figure 2.14(a) shows the calibration data for the backend noise temperature T_{BE} versus frequency. This measurement was performed using a nitrogen cooled fixed load method, where the noise power of the backend terminated with a 50 Ω load was first measured at room temperature, and then measured again with the 50 Ω load submerged in a small liquid nitrogen bath at 77 K. Thermal insulation was placed over the bath to minimize vapor cooling of the 3.5" long stainless steel coaxial cable connecting the backend to the 50 Ω load. The time between hot and cold measurements was 1 minute, which was the time it took to dip the load into the nitrogen bath and allow its temperature to stabilize as indicated

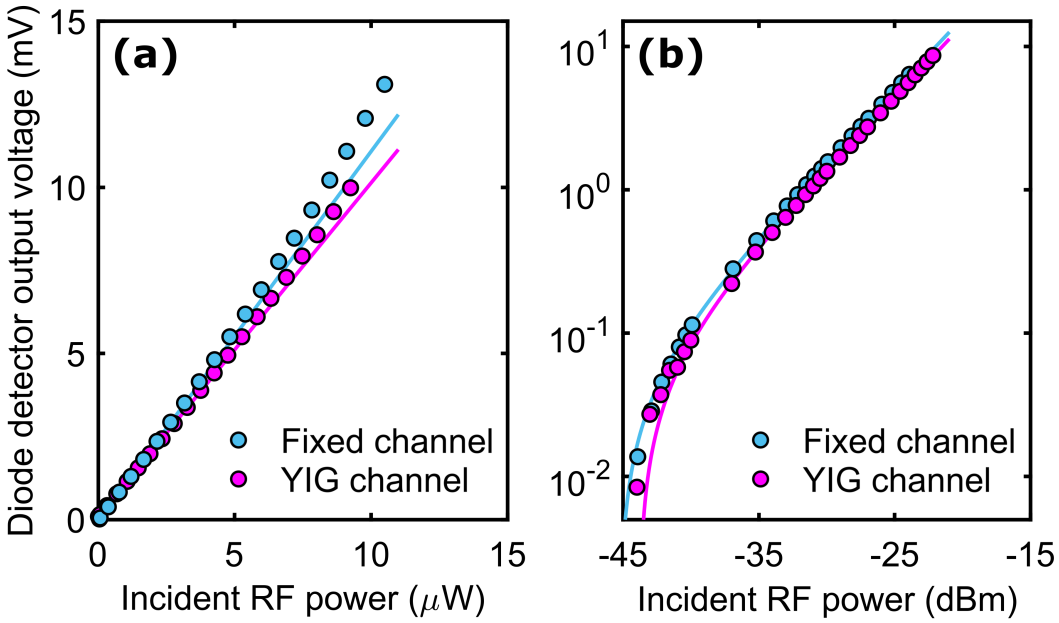

Fig. 2.12: Diode detector output voltage versus incident microwave power on the diode detector for the fixed 5 GHz filter channel (blue circles) and the YIG channel with center frequency set to 5 GHz (magenta circles). **(a)** Data shown for incident microwave power ranging from 0 μW to 10 μW (−20 dBm). A linear fit to the data below 4 μW (−24 dBm) is also shown (solid lines). A nonlinear response can be seen above 5 μW (-23 dBm). **(b)** Data shown for incident microwave power ranging from −44 dBm to −22 dBm, plotted logarithmically. A linear fit to the full range of data is also shown (solid lines)

by a plateauing of the measured noise power. The backend noise temperature was found to be stable over at least a several-month timeframe. All backend amplifiers, tunnel diode detectors, and DC pre-amplifiers were wrapped in thermal insulation to mitigate drifts in gain and noise temperature.

Noise power was generated by a packaged 2 – 18 GHz solid state SMA noise diode with a 15 dB excess noise ratio, which was biased using an Agilent 33220A arbitrary waveform generator whose output was amplified by a MOSFET biasing circuit. The circuit was formed by an Ohmite Arcol HS25 100 Ω power resistor in series with a Vishay Siliconix IRFP140 power MOSFET and the noise diode in parallel, with the MOSFET gate bias pulsed by the 3 V square wave output of the signal generator. A schematic of an identical circuit which was used to pulse the microwave switch is shown in Fig. 2.10 labeled as "Calibration switch." Figure 2.14(b) shows the calibration data for the noise source ENR versus frequency, measured by taking Y-factor measurements with the noise source connected directly to the calibrated backend detector. The inset shows a schematic of the MOSFET biasing circuit. The

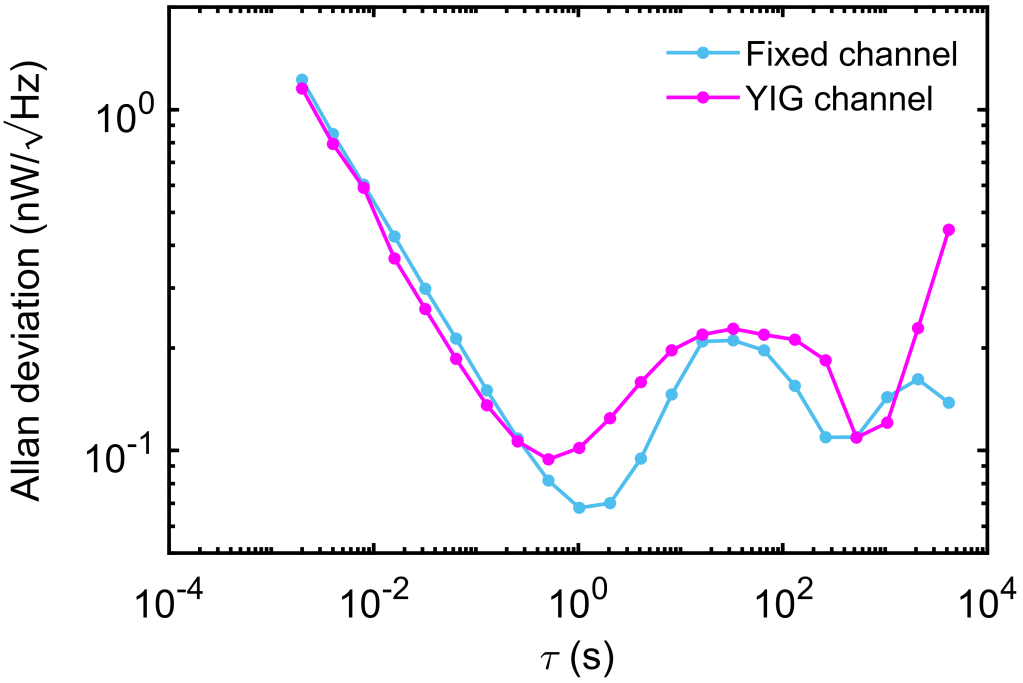

Fig. 2.13: Allan deviation versus integration time for the fixed 5 GHz filter channel (blue dots) and the YIG channel with center frequency set to 5 GHz (magenta dots) with −100 dBm incident microwave power on the detectors' inputs. A minimum is observed at approximately 1 s, which was used as the recalibration period for subsequent measurements. Another minimum is seen at 500 s, suggesting the presence of a noise source other than 1/f noise.

ENR was extracted using the following equation:

$$E = \frac{Y-1}{T_0}(T_C + T_{BE}) \tag{2.14}$$

The noise source chassis, which was wrapped in thermal insulation to promote thermal equilibration between the chassis and the internal noise diode, was monitored at all times using a type T thermocouple, and was found to vary negligibly under all experimental conditions. We took the chassis temperature to be equal to the internal diode temperature T_C.

The MOSFET biasing scheme allowed for Y-factor sampling as fast as hundreds of kHz, limited by the RC time constant of the MOSFET and noise diode circuit. Figure 2.14(c) shows the fastest Y-factor measurements recorded on this setup with data sampled at f_s = 600 kHz (the fastest stable sampling speed of the DAQ) and the noise source pulsed at f_{ENR} = 50 kHz, taken with the noise source connected directly to the backend detector. The fact that no discernible rise time is observed indicates that the the noise source circuit cutoff frequency is faster than 600 kHz.

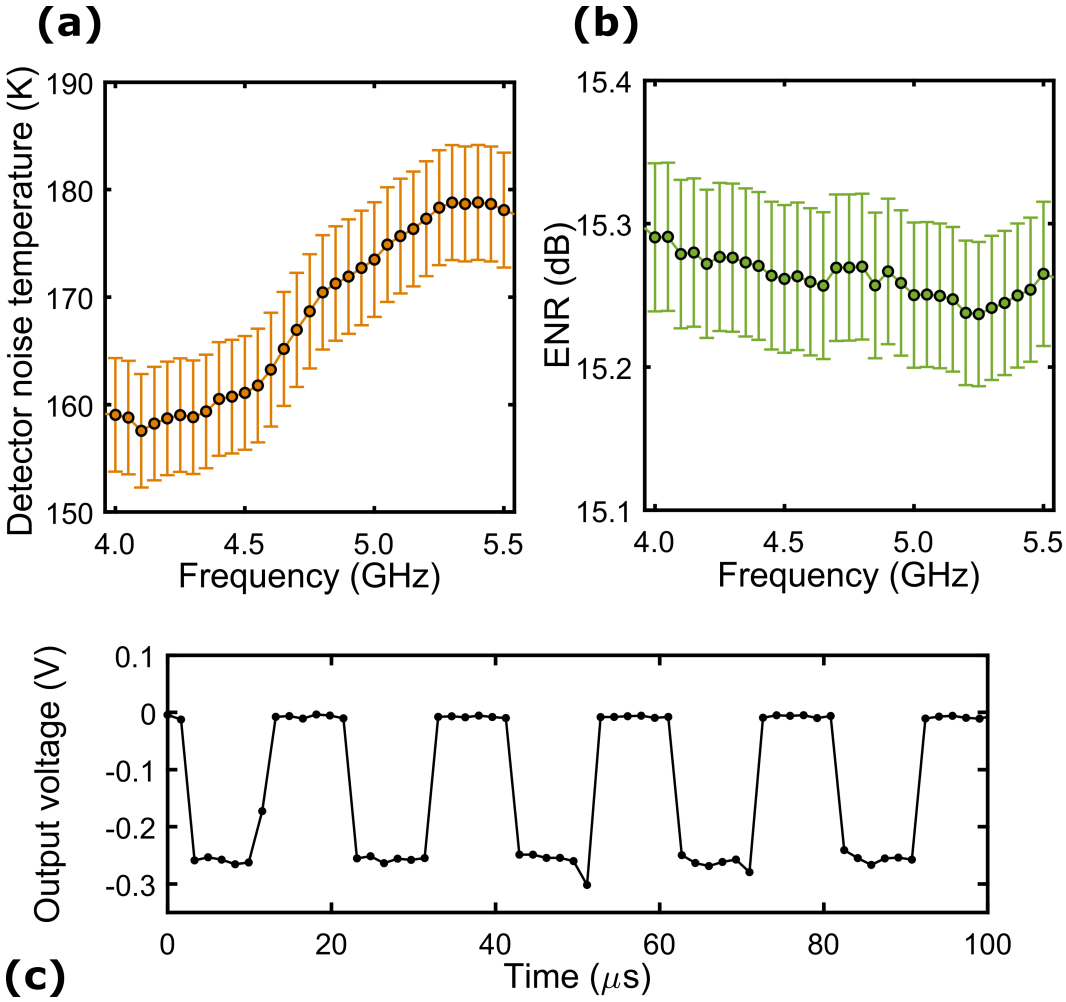

Fig. 2.14: **(a)** Backend detector noise temperature versus frequency. Error bars reflect the uncertainty in the temperature of the cable connecting the 50 Ω load to the backend. **(b)** Noise source ENR versus frequency. Error bars reflect the error propagated from uncertainty in the backend noise temperature. **(c)** Diode detector output voltage sampled at f_s = 600 kHz with the noise source connected directly to the input of the backend detector and pulsed at f_{ENR} = 50 kHz.

2.5 Calibrations in liquid cryogen environments

Two separate liquid helium-4 dewar baths were used for calibration of each cryogenic component entering into Eq. (2.6). One dewar bath was used to calibrate the coaxial cable losses L_1 and L_3 and temperature T_{coax}, and then another dewar bath was used to calibrate the attenuator loss L_2.

The general procedure in each calibration dewar was as follows. The dipstick was used to submerge the mounting stage 2 cm from the bottom of a fully filled 60 L liquid helium-4 dewar at 4.2 K and ambient pressure. After waiting 30 minutes for

thermal equilibration, calibration measurements were taken. The dewar was then sealed, and a vacuum pump was used to evaporatively cool the liquid into the He II phase. A steady-state temperature of 1.6 K was reached after roughly 6 hours of pumping, and further calibration measurements were taken. A heater was then switched on for less than 2 hours to accelerate the boil-off rate of the remaining liquid, and switched off when a spike in stage temperature was observed which indicated that the liquid surface had dropped below the stage. Further calibration was performed after turning off the heater as the stage was allowed to warm from 1.6 K under the ambient heating power of the measurement apparatus. The dewar was then back-filled with helium-4 exchange gas at 1 psig to facilitate thermalization to room temperature, at which point the dipstick was removed.

We now discuss the details of the measurements in each calibration dewar. In the first calibration dewar, the attenuator and DUT shown in the configuration of Fig. 2.6 were replaced with a short through which was thermally anchored to the copper stage. The total cable loss was measured, with the inner-outer DC block SMA connectors used as the input and output reference planes. Figure 2.15(a) shows the total loss L_{coax} of the coaxial cables measured at room temperature in air and dipped in the first calibration dewar at 4.2 K and 1.6 K. To isolate the individual cable losses L_1 and L_3, the losses of the input cable (up to the input of the attenuator) and output cable (from the output of the DUT) were also measured independently at room temperature, and their ratio was assumed to remain constant for all temperatures.

The lumped coaxial cable physical temperature T_{coax}, which is the effective temperature at which the cables radiate their noise power, was measured directly using the Y-factor method. Applying the same approach as in the derivation of Eq. (2.6), we can write the measured hot and cold noise power of a single impedance matched lossy element of loss L and physical temperature T_L as:

$$P_{\text{H}} = \frac{T_0 E + T_{\text{C}}}{L} + \frac{T_L(L-1)}{L} + T_{\text{BE}} \tag{2.15}$$

$$P_{\text{C}} = \frac{T_{\text{C}}}{L} + \frac{T_L(L-1)}{L} + T_{\text{BE}} \tag{2.16}$$

taking the ratio $Y = \frac{P_{\text{H}}}{P_{\text{C}}}$ and solving for T_L gives:

$$T_L = \frac{1}{L-1}\left(\frac{T_0 E}{Y-1} - T_{\text{C}} - T_{\text{BE}} L\right) \tag{2.17}$$

Figure 2.15(b) shows the measured lumped cable temperature versus frequency with the cables dipped in a 4.2 K He I bath, using Eq. (2.17). We assumed that both cables

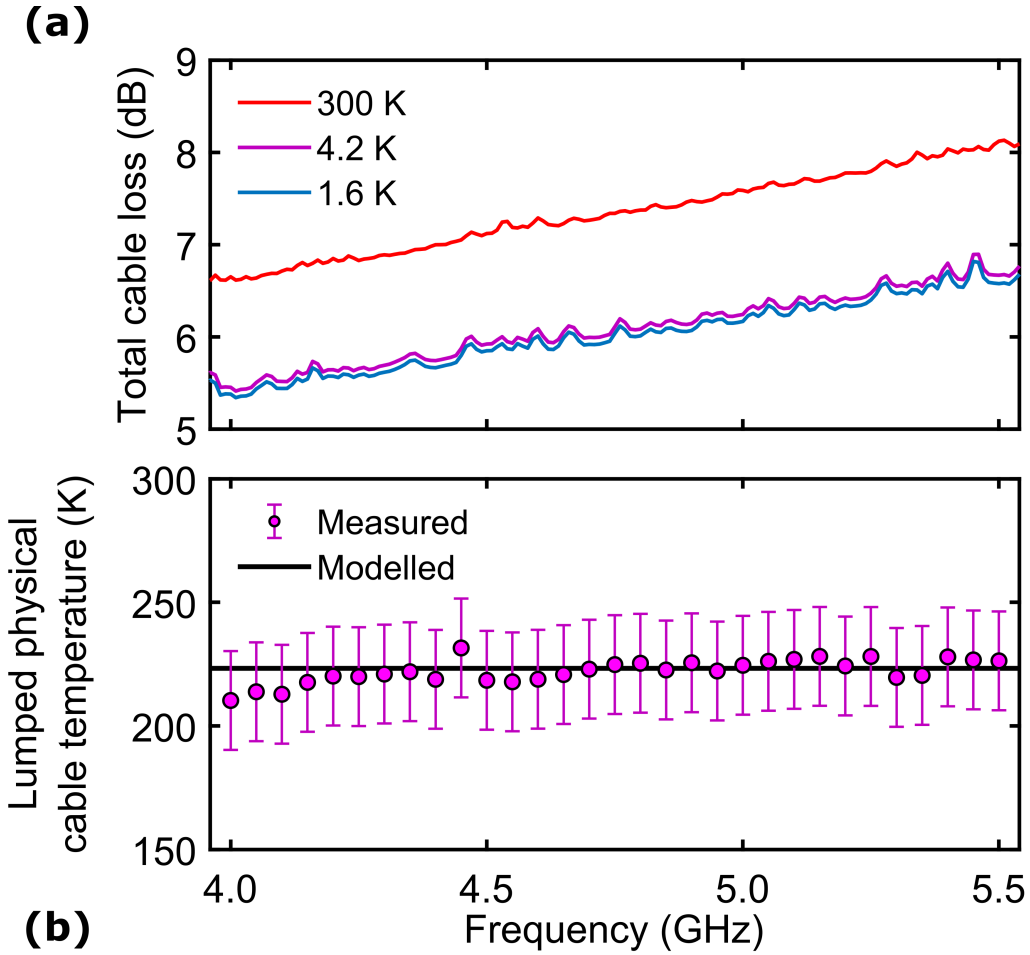

Fig. 2.15: **(a)** Total loss of input and output coaxial cables versus frequency measured at 300 K (red line), 4.2 K (magenta line), and 1.6 K (blue line) with a commercial VNA. **(b)** Lumped physical coaxial cable temperature versus frequency obtained from Y-factor measurements (magenta circles) and from a heat conduction model (black line). Error bars represent an estimate of the total uncertainty including systematic errors.

were at the same physical temperature. The 1.6 K He II calibration measurement is omitted for clarity as it is within 10 K of the He I measurement.

To support the accuracy of this method, we developed a thermal model of the cables used in our experiment. This model extends the work from Ref. [134] to include the effect of heat transfer between the cables and the surrounding fluid. We consider infinitesimal cross-sectional slices of the cable in contact with the surrounding bath. Assuming steady-state where the net heat flux is zero we can write:

$$\dot{Q}(x + \mathrm{d}x) = \dot{Q}(x) + \mathrm{d}\dot{Q}(x) \tag{2.18}$$

where $\dot{Q}(x)$ is the heat flux at height x along the cable, and $\mathrm{d}\dot{Q}(x)$ is the differential

convective heat flux along the slice of length dx. Applying Fourier's law along the length of the cable and using the definition of convective heat transfer [135] we can write:

$$\dot{Q}(x) = C_s(x)\frac{dT}{dx}\bigg|_x \tag{2.19}$$

$$d\dot{Q}(x) = PH_{g,l}(x)\Big(T(x) - T_{g,l}(x)\Big)dx \tag{2.20}$$

$$C_s(x) = \frac{\kappa_{steel}(x)A_{steel} + \kappa_{ptfe}(x)A_{ptfe}}{\kappa_{steel}(x)\kappa_{ptfe}(x)A_{steel}A_{ptfe}} \tag{2.21}$$

where $C_s(x)$ is the thermal conductance arising from the parallel stainless steel and PTFE heat conduction channels in the cable, P is the perimeter of the cable, $H_{g,l}(x)$ and $T_{g,l}(x)$ are the convection coefficient and temperature of the surrounding gas and liquid baths, respectively, and $\kappa_{steel}(x)$, $\kappa_{ptfe}(x)$, A_{steel} and A_{ptfe} are the thermal conductivities and cross-sectional areas of the inner stainless steel conductor and PTFE dielectric in the cable, respectively. The temperature dependence of the thermal conductivities κ_{steel} and κ_{ptfe} were taken from compiled data from NIST [136, 137]. Massaging the above equations and rearranging, we arrive at:

$$C_s(T(x))\frac{d^2T}{dx^2} + \frac{dC_s}{dT}(T(x))\left(\frac{dT}{dx}\right)^2 - PH_{g,l}(x)\Big(T(x) - T_{g,l}(x)\Big) = 0 \tag{2.22}$$

A schematic of the model is shown in Fig. 2.16(a), where we have defined $R_{steel} = (\kappa_{steel}A_{steel})^{-1}$, $R_{ptfe} = (\kappa_{ptfe}A_{ptfe})^{-1}$, and $R_{g,l} = (PH_{g,l}dx)^{-1}$. Equation (2.22) was solved numerically using the bvp4c routine in MATLAB with fixed boundary values of 301 K and 4.2 K, and assuming a liquid surface height of 10 cm above the bottom of the cable. Table 2.1 lists the remaining assumed parameter values, and Fig. 2.16(b) shows the modelled coaxial cable temperature profile. Averaging over this curve yields an effective lumped physical temperature of the stainless steel coaxial cable of $T_{steel} = 208K$. We now determine the effective lumped physical temperature of the full cable by including the additional SMA cabling which connected the stainless steel cables to the noise source and backend detector. We make the simplifying assumptions that the entire stainless steel cable radiates its noise at T_{steel} with a loss L_{steel} = 2.34 dB and that the additional cabling radiates entirely at T_{cab} = 301 K with a loss of L_{cab} = 0.65 dB. The additional cabling loss was measured directly, and the stainless steel cable loss was found by subtracting L_{cab} from the total loss measured at 4.2 K shown in Fig. 2.15(a), at 5 GHz. Cascading the noise from these

Parameter	Value	Source
κ_{steel}	T dependent	[136]
κ_{ptfe}	T dependent	[137]
A_{steel}	1.30 mm^2	Measured
A_{ptfe}	18.83 mm^2	Measured
P	1.12 mm	Measured
H_{g}	30 Wm^{-2}K^{-1}	[138]
H_{l}	15 kWm^{-2}K^{-1}	[63]

Table 2.1: Table of parameters used in solving the coaxial cable thermal model.

two cables we find:

$$T_{\text{coax}} = \frac{L_{\text{cab}} L_{\text{steel}}}{L_{\text{cab}} L_{\text{steel}} - 1} \left(\frac{T_{\text{cab}}(L_{\text{cab}} - 1)}{L_{\text{cab}} L_{\text{steel}}} + \frac{T_{\text{steel}}(L_{\text{steel}} - 1)}{L_{\text{steel}}} \right) \tag{2.23}$$

$$T_{\text{coax}} = 223.3\text{K}$$

The estimated lumped coaxial cable temperature from this model is plotted as a horizontal line in Fig. 2.15(b).

The final calibration measurements taken in the first calibration dewar were the loss L_{coax} and temperature T_{coax} of the cables as the stage was allowed to warm up after the liquid level dropped below the level of the stage. These measurements were again performed using the Y-factor measurement. Figures 2.17(a) and 2.17(b) shows the continuous measurement of T_{coax} and L_{coax} over the full lifetime of the calibration dewar bath from the start of the cooldown until the stage reached 100 K during warmup. Figure 2.17(c) shows the stage temperature over the same time period, as measured by the temperature diode in the attenuator (all temperature diodes agreed to within 1 % at all temperatures shown here). Figure 2.17(d) shows the calibration curves for cable temperature and loss which were ultimately used. These curves were generated by fitting a smoothing spline to the cable temperature and loss data plotted versus stage temperature data during the warmup.

In the second calibration dewar, the short through was replaced by the cold attenuator, which was a packaged 20 dB wideband chip attenuator. The mounted attenuator is shown pictured in Fig. 2.6. The total loss $L_{\text{tot}} = L_{\text{coax}} L_2$ was measured using the same procedure as in the first calibration dewar. The attenuator loss L_2 was extracted by dividing L_{tot} by the previously measured L_{coax}. Figure 2.18 shows

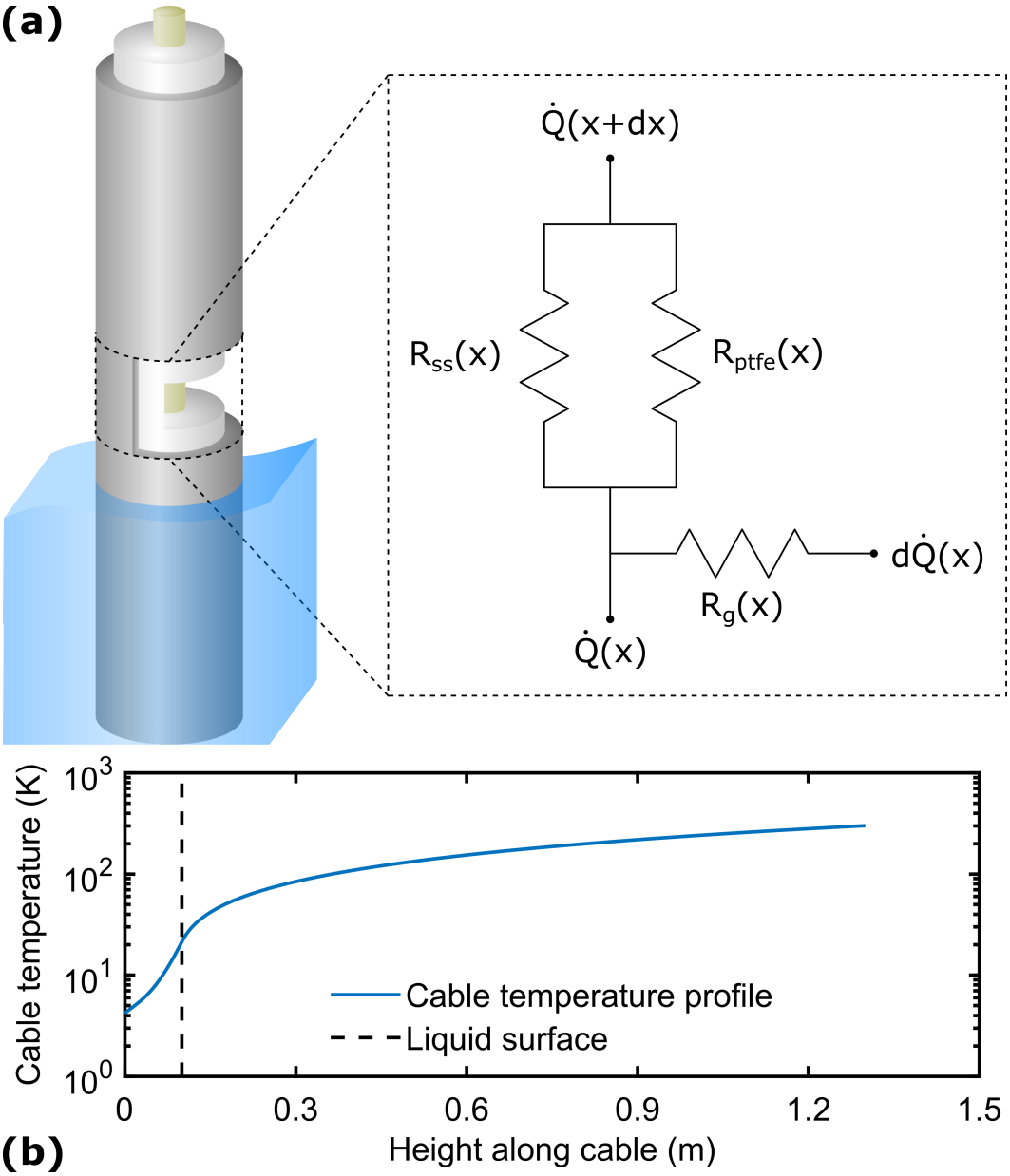

Fig. 2.16: **(a)** Schematic of the coaxial cable temperature model showing a slice of length dx along the cable in contact with the gas environment. **(b)** Coaxial cable temperature profile (blue line) versus height along the cable. The height of the liquid surface is also shown (vertical dashed black line).

the attenuator loss versus microwave frequency measured at room temperature, 4.2 K, and 1.6 K using the VNA. The attenuator loss was found to vary by less than 0.2 dB between all temperatures, which is consistent with other measurements of similar chip attenuators [139]. A measurement of the temperature of the attenuator using the Y-factor method was not possible in this case due to the larger loss of

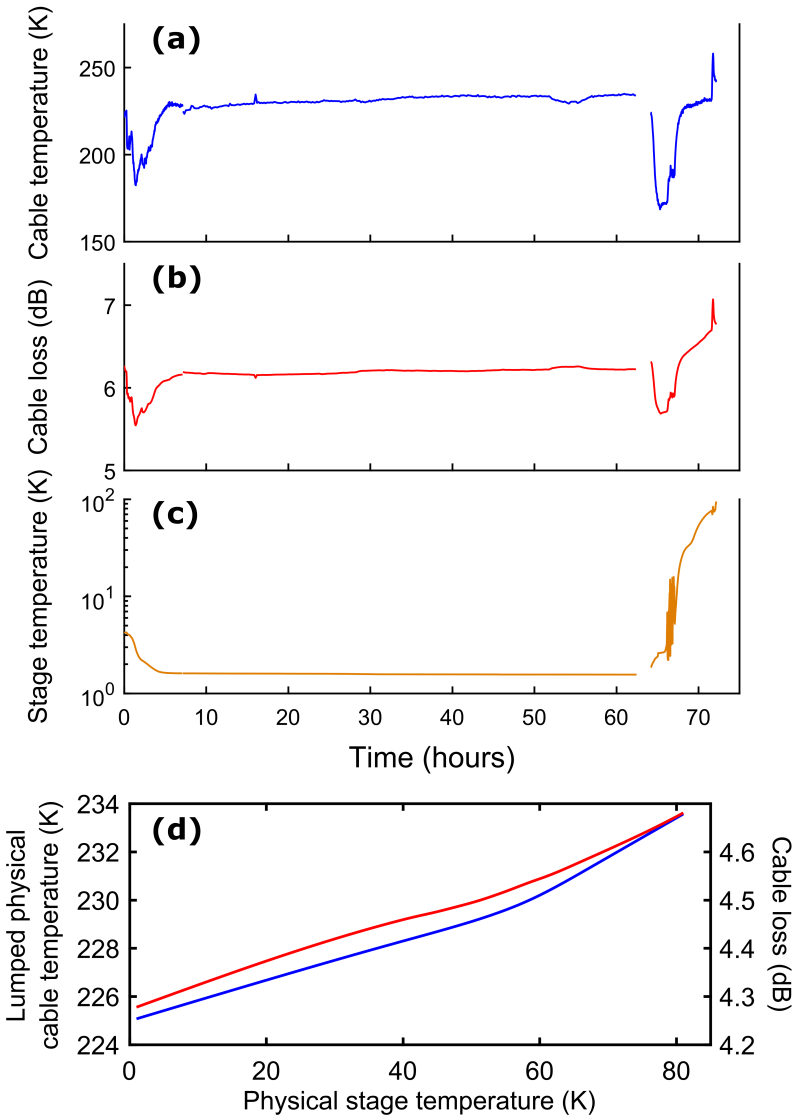

Fig. 2.17: **(a)** Cable temperature (blue line), **(b)** cable loss (red line), and **(c)** stage temperature (orange line) measured over the lifetime of the first calibration dewar. Cable temperature and cable loss were measured using the Y-factor method, and stage temperature was measured by the temperature diode housed in the attenuator. Recalibration using a VNA was performed at $t = 7$ hours and $t = 62$ hours, reflected in the discontinuities in acquired data. **(d)** Cable temperature (blue line) and cable loss (red line) versus physical stage temperature, generated by fitting a smoothing spline to the time series data of the cable temperature and loss plotted versus stage temperature, respectively, during the warming phase of the calibration measurements. These curves were used as the calibration curves for subsequent warming data.

the attenuator. Instead, the temperature T_{L_2} of the attenuator was measured by a calibrated Lake Shore DT-670-SD temperature diode indium-bonded directly to

the attenuator chip substrate. The diode calibration curve was provided by Lake Shore, and the saturated liquid temperature of He I at 4.23 K was used to correct for DC offsets. We assumed that negligible temperature differences existed between the attenuator, mounting stage, and DUT, and we therefore took the DUT physical temperature to be $T_{\text{phys}} = T_{L_2}$. All temperature diodes were measured using a Lake Shore 336 temperature controller, which converted the temperature to a voltage which was measured by the DAQ synchronously with all Y-factor measurements.

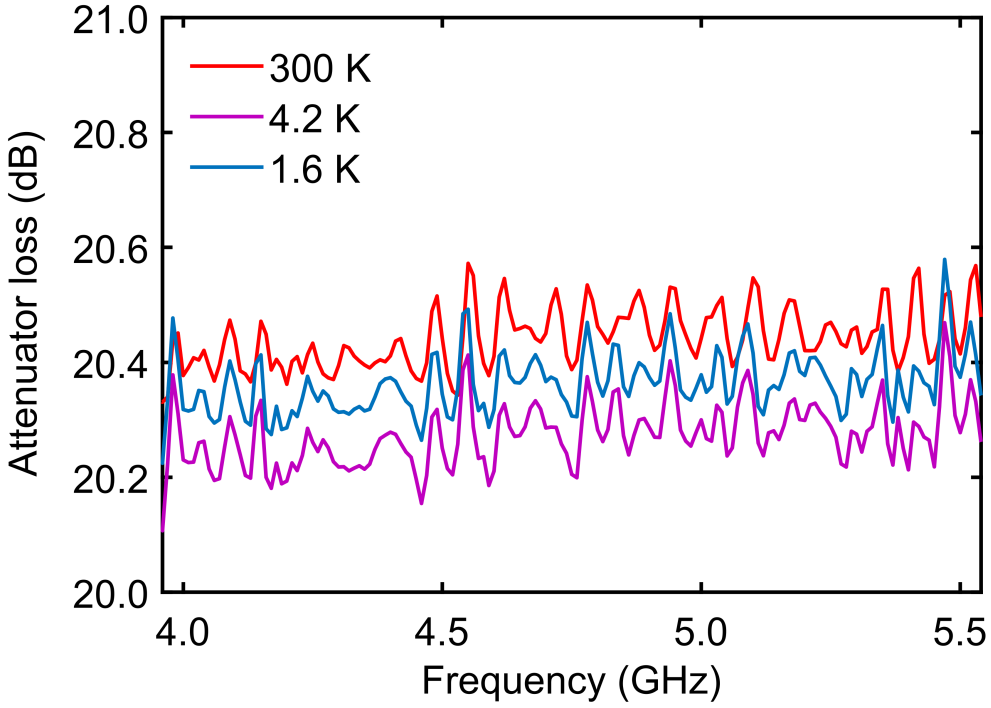

Fig. 2.18: Attenuator loss versus frequency at room temperature (red line), 4.2 K (magenta line) and 1.6 K (blue line).

2.6 LNA noise and gain measurements

With the calibration data obtained, the noise and gain of the DUT was measured using two additional liquid helium-4 dewar baths at various frequencies, temperatures, and biases. The gate and drain bias voltages V_{GS} and V_{DS}, which were nominally applied equally to each individual transistor through , were varied to yield transistor drain-source current densities I_{DS} from 35 mA mm^{-1} to 120 mA mm^{-1}, corresponding to dissipated powers $P_{\text{DC}} = V_{\text{DS}} I_{\text{DS}}$ per transistor of 15 mW mm^{-1} to 150 mW mm^{-1}. The relevant measured values from the calibration procedure described above were used to extract G and T_{e} from Eqs. (2.6) and (2.8).

In the first measurement dewar, the device was mounted to the stage in the configu-

ration shown in Fig. 2.6, and the cooldown procedure followed that of the calibration dewars described above. At each physical temperature, the DUT bias was varied and Y-factor measurements were taken versus frequency by adjusting the YIG filter center frequency. In addition, the calibration measurement of $V_{\mathrm{H}}^{\mathrm{cal}}$, $V_{\mathrm{C}}^{\mathrm{cal}}$, and $G_{\mathrm{full}}^{\mathrm{cal}}$ was performed, with the DUT bias chosen arbitrarily to be its low-noise bias. Using these measurements, the device gain G could be extracted from Y-factor voltage measurements at any bias using Eq. (2.8) without requiring a separate VNA measurement. This calibration was found to be stable over several days, and was repeated each day before data acquisition.

In addition to measurements under specific liquid cryogen environments, continuous Y-factor measurements were also taken as the He II bath was pumped away, yielding noise data both before and after the DUT gate was submerged. The measurements were performed at a fixed bias of $P_{\mathrm{DC}} = 80$ mW mm^{-1} and frequency of $f = 4.55$ GHz. This frequency was chosen due to it being the optimum noise match frequency as determined by the IMN of the DUT. The bias was chosen to be sufficiently high that any self-heating mitigation would be readily observed without risking device damage due to prolonged biasing.

The He II film creep effect [140] was expected to cause the entire mounting stage, including the heated DUT region, to be coated in a superfluid film even after the liquid bath surface dropped below the DUT height. To support this assumption, we derive the expected saturated film thickness d in terms of the height above the liquid surface level h. This can be done by expressing the chemical potential of the film as $\mu_{\mathrm{film}} = \mu_0 + mgh - \alpha d^{-n}$, where μ_0 is the chemical potential of the bulk liquid, mgh is the gravitaional potential at height h, and αd^{-n} is the van der Waals potential. In equilibrium we must have $\mu_{\mathrm{film}} = \mu_0$, so that:

$$d = \left(\frac{\alpha}{mgh}\right)^{1/n} \tag{2.24}$$

where we use the approximation $n = 3$ in the limit of thin films $d \leq 0.5$ nm [96]. This dependence has been confirmed by a number of experiments [110, 111]. We plot the prediction of Eq. (2.24) in Fig. 2.19 using a typical value of $(\alpha/mg)^{1/3} = 31.5$ nm for metal surfaces [109, 141]. Since the transistor inside the packaged device sits approximately 7 cm from the bottom of the mounting stage, we estimate a film thickness of at least 16 nm, with the thinnest film occurring immediately prior to the liquid level dropping below the mounting stage. Assuming a mean atomic spacing in the liquid of 0.3 nm, this thickness can be interpreted as a superfluid film of 53

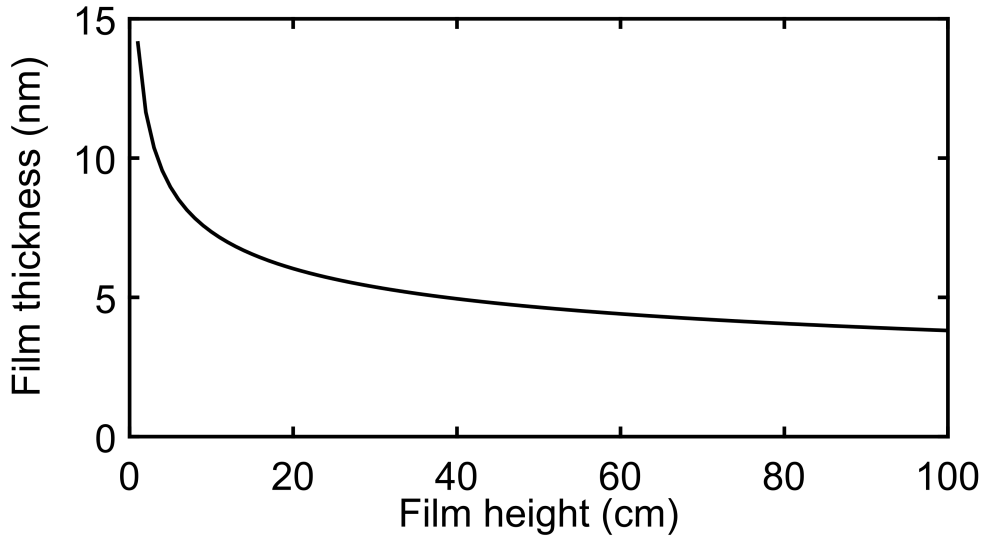

Fig. 2.19: Thickness of a He II film versus height above the bulk fluid.

atomic layers. We note that superfluidity has been observed in films as thin as 2.4 atomic layers [142]. We used the sharp rise observed in the attenuator and stage temperature measurements to indicate the complete evaporation of He II from the stage. The DUT noise was also measured on warming from 1.6 K to 80 K in the vacuum space left after all liquid was pumped away.

In the second measurement dewar, the noise temperature was again measured in 4.2 K liquid using the same procedure as in the first measurement dewar but without the subsequent evaporative cooling step. Instead, the liquid bath was allowed to evaporate under the heating power of the dipstick, enabling measurements to be taken in a vapor environment at several temperatures after the liquid level dropped below the mounting stage. The vapor warmed sufficiently slowly (< 1 K/hour) such that all measurements were effectively in a steady state vapor environment. The calibrations used for these measurements were the same as for the 4.2 K liquid since the coaxial cable loss and temperature were observed to change negligibly up to 45 K stage temperature.

Chapter 3

MEASUREMENT RESULTS, DEVICE MODELING, AND INTERPRETATIONS

In this chapter, we present the full suite of noise temperature and gain measurements taken at various frequencies, biases, physical temperatures, and in different cryogenic environments, as well as a derivation of the uncertainty analysis of our measurement scheme. We detail the small-signal model of the device which was developed, and interpret the measurement results using it. We compare these results with the predictions of a phonon radiation model of heat transport in the device. We then examine how our results compare with prior He II interfacial heat transport studies. We finish by incorporating the bias dependence of the gate temperature predicted by the radiation model into both the Pospiesalski noise model and a phenomenological circuit model, in order to demonstrate the benefits that a reduction in drain temperature through, for instance, improved device engineering would have on the overall noise temperature.

3.1 Microwave noise temperature versus bias and frequency

Figure 3.1 shows the noise temperature T_e and gain G versus bias power P_{DC} taken at a fixed frequency of $f = 4.55$ GHz, the frequency at which the device exhibited its noise minimum as determined by the IMN, and in several different cryogenic environments. Here, P_{DC} was varied by changing V_{DS} for a fixed V_{GS}. In Fig. 3.1(a), V_{DS} ranged from 0.21 V to 0.99 V yielding current densities I_{DS} from 57.9 mA mm^{-1} to 241.6 mA mm^{-1}, with a peak gain of $G = 27.5$ at biases above $P_{DC} = 50$ mW mm^{-1}. In Fig. 3.1(b), V_{DS} ranged from 0.15 V to 1.25 V yielding current densities I_{DS} from 29.2 mA mm^{-1} to 190.5 mA mm^{-1}, with a peak gain of $G = 31.5$ dB at biases above $P_{DC} = 75$ mW mm^{-1}. In Fig. 3.1(c), V_{DS} ranged from 0.19 V to 1.35 V yielding current densities I_{DS} from 21.3 mA mm^{-1} to 169.0 mA mm^{-1}, with the same peak gain of $G = 31.5$ dB at biases above $P_{DC} = 75$ mW mm^{-1}. The data taken with the DUT immersed in vapor environments was taken in the second measurement dewar, where each sweep was taken up to a smaller maximum power. The gain varies by less than 0.5 dB across all temperatures, indicating consistent biasing across each measurement dewar and cryogenic environment. The dependence of both G and T_e on P_{DC} and T_{phys} is qualitatively similar for each fixed V_{GS}. As bias is

increased, T_e initially decreases as G increases. The noise temperature then bottoms out as the gain saturates, before T_e begins to increase with bias. Across all cryogenic environments, the minimum noise temperature occurs between 1.96 K ($V_{GS} = -2.8$ V and $T_{phys} = 1.6$ K in He II, as seen in Fig. 3.1(b)) and 2.81 K ($V_{GS} = -3.2$ V and $T_{phys} = 33.8$ K in vacuum, as seen in Fig. 3.1(c)), an indication that cryogenic environment did not play a significant role in mitigating self-heating at these biases. A divergence in T_e between different physical temperatures is observed beginning at $P_{DC} = 50$ mW mm^{-1} in Fig. 3.1(a) and at $P_{DC} = 75$ mW mm^{-1} in both Figs. 3.1(b) and 3.1(c). The reason for this divergence is unclear, although we suspect that it is related to a changing thermal resistance between the channel, gate, and substrate, and not due to self-heating mitigation by the liquid cryogens.

Figure 3.2 shows T_e and G versus drain-source current I_{DS} taken at a fixed frequency $f = 4.55$ GHz in several different cryogenic environments, where I_{DS} was varied by changing V_{GS} for a fixed voltage V_{DS}^{PS} output by the biasing power supply. Converting I_{DS} to P_{DC} was not possible for this data due to complications arising from an asymmetry in the biasing circuits between the two stages, which led to an uncertainty in the true V_{DS} across each transistor. Although this uncertainty was also present in the data shown in Fig. 3.1, in that case since the gate voltage was fixed, the offset of V_{DS} caused by the bias asymmetry did not change between data points. For measurements taken in the first measurement dewar (He II, He I, and vacuum) the gate-source voltage was swept from $V_{GS} = -4.1$ V to $V_{GS} = -1.0$ V, whereas for measurements taken in the second measurement dewar (vapor) this voltage was swept from $V_{GS} = -4.0$ V to $V_{GS} = -2.0$ V. In Fig. 3.2(a) the drain-source voltage output by the power supply was $V_{DS} = 1.0$ V. The gain and noise remain relatively flat with increasing I_{DS}, with T_e varying by less than 1.5 K and G varying by less than 5 dB until a critical bias of $_{DS} = 110$ mA mm^{-1} when the gate becomes sufficiently open that the gain decreases and the noise temperature increases rapidly. The noise temperature in the flat region varies by less than 1.8 K for the same bias across different physical temperatures. In Fig. 3.2(b) the drain-source voltage output by the power supply was $V_{DS} = 1.4$ V. In this case, there was a larger spread in T_e versus T_{phys} with a maximum difference of 4.2 K between the noise measured in vacuum and He II at a bias of 99.9 mA mm^{-1}, and a bump in noise temperature is also observed between the flat region and the region of rapidly decreasing gain. The origin of this bump is presently unclear, and is suspected to be associated with asymmetric biasing.

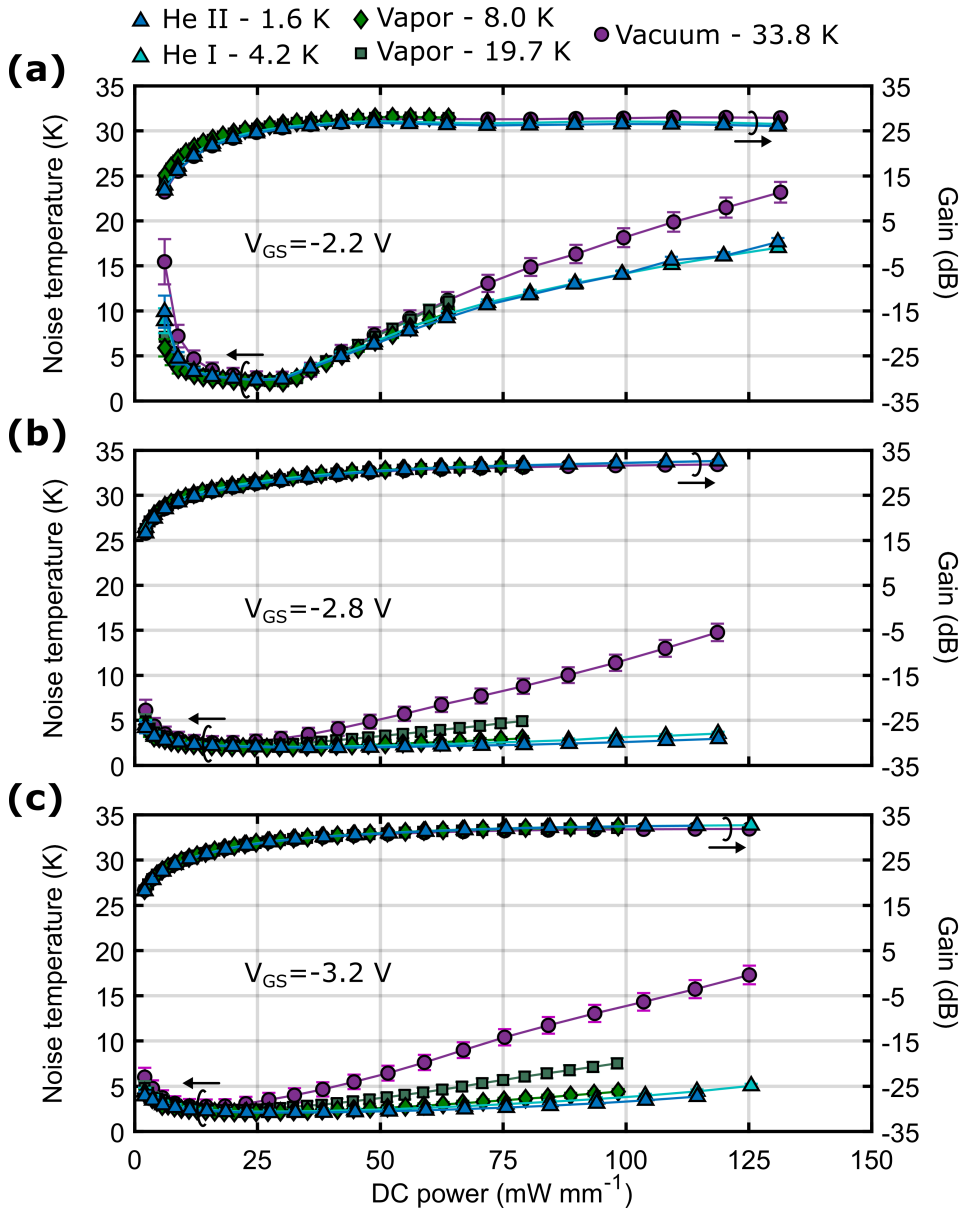

Fig. 3.1: Noise temperature (left axis) and gain (right axis) versus bias measured at a fixed frequency of f = 4.55 GHz in the following cryogenic environments: 1.6 K He II (blue triangles), 4.2 K He I (cyan triangles), 8.0 K vapor (green diamonds), 19.7 K vapor (green squares), and 33.8 K vacuum (purple circles). The bias was varied by changing the drain-source voltage for a fixed gate-source voltage of **(a)** V_{GS} = −2.2 V, **(b)** V_{GS} = −2.8 V, and **(c)** V_{GS} = −3.2 V. For each fixed V_{GS} the low-noise bias shifts by less than 10 mW mm^{-1} and the noise temperature at the low-noise bias changes by less than 1 K across all physical temperatures.

Figure 3.3(a) shows T_e and G versus microwave frequency f with the device biased at its low-noise bias P_{DC} = 24.5 mW mm^{-1} and immersed in five different bath conditions ranging from 1.6 K He II to 35.9 K vacuum. The noise varies by less

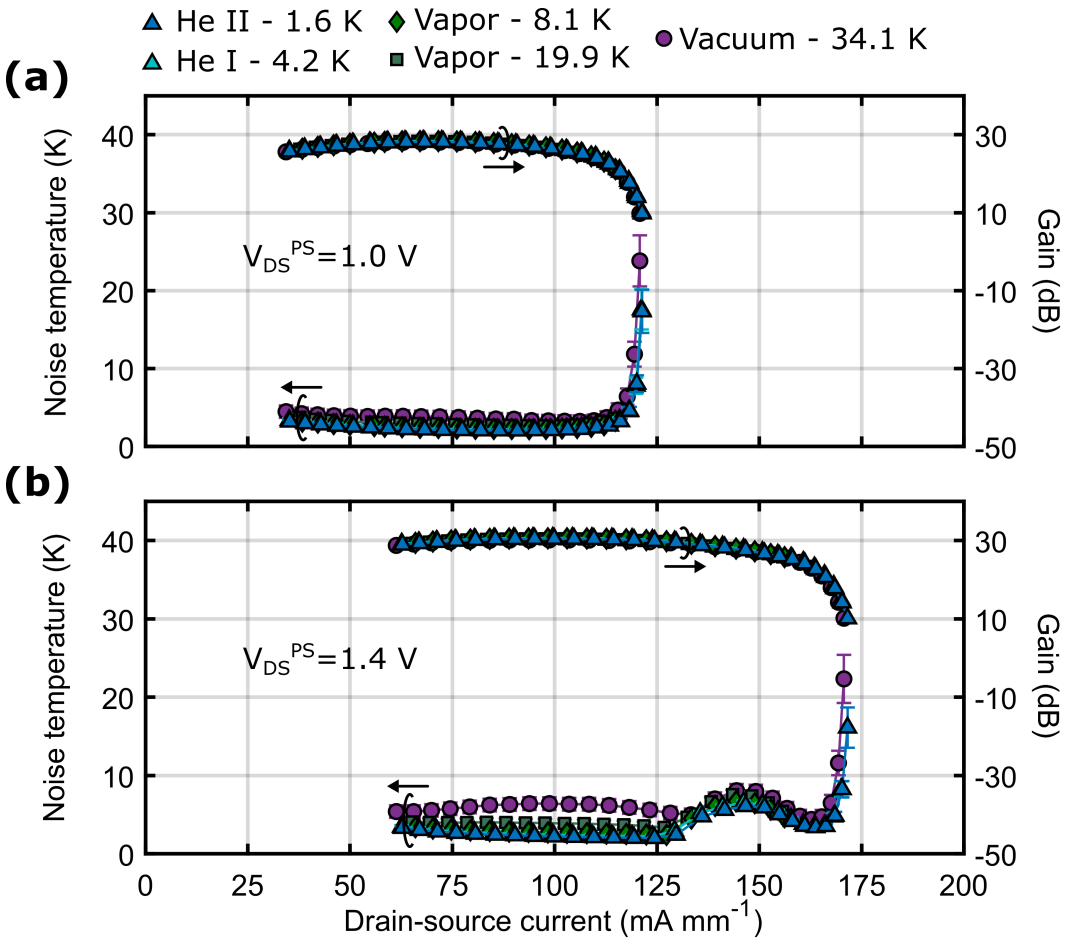

Fig. 3.2: Noise temperature (left axis) and gain (right axis) versus drain-source current measured at a fixed frequency of f = 4.55 GHz in the same cryogenic environments as in Fig. 3.1. The bias was varied by changing the gate-source voltage for a fixed drain-source voltage output by the power supply of **(a)** $V_{\mathrm{DS}}^{\mathrm{PS}=1.0}$ V and **(b)** $V_{\mathrm{DS}}^{\mathrm{PS}=1.4}$ V.

than 2 K across all measured frequencies and temperatures at this bias. The noise increases monotonically with increasing physical temperature regardless of bath condition. The gain varies by approximately 4 dB over the measured frequency range, peaking at f = 4 GHz. The gain variation with physical temperature is less than 0.5 dB at fixed f and P_{DC}.

Figure 3.3(b) shows T_{e} and G versus f with the device immersed in 1.6 K He II at three different device biases of P_{DC} = 24.5 mW mm^{-1}, P_{DC} = 79.5 mW mm^{-1} and P_{DC} = 120 mW mm^{-1}. At biases below P_{DC} = 79.5 mW mm^{-1} the noise temperature varies by less than 1.5 K for all frequencies, while above P_{DC} = 79.5 mW mm^{-1} the noise increases more rapidly with bias. The gain

increases monotonically with increasing bias while retaining the same shape versus frequency, but it appears to asymptotically plateau at approximately the highest gain shown here, at a bias of P_{DC} = 120 mW mm^{-1}.

3.2 Interpretation using small-signal modeling

To interpret these measurements, a microwave model of the full device including the IMN, monolithic microwave integrated circuit (MMIC) components, and transistor small-signal model was made using Cadence AWR Microwave Office. Figure 3.4 shows a micrograph image of the 2-stage MMIC, including the external IMN, which are all housed inside a gold-plated copper chassis. The model used micrograph measured values of the IMN, foundry schematic values for the MMIC, and independently measured small-signal model values from nominally identical discrete OMMIC D007IH 4f200 transistors from Ref. [58]. The small-signal model and IMN parameters were manually tuned, constrained to change by less than 20% from the starting values to fit both the gain and noise temperature curves. The gain data from several datasets were used first to tune the IMN microstrip geometry which determined the shape of the gain versus frequency dependence. The gain data from each dataset was then used to tune the following small-signal model parameters: the gate-source capacitance C_{gs}, the gate-drain capacitance C_{gd}, the transconductance g_m, and the drain-source conductance g_{ds}. Finally the noise data was used to tune and extract T_g and T_d. An image of the transistor model schematic at the low-noise bias at 1.6 K is shown for reference in Fig. 3.5. The parameters not listed above, such as the gate, drain, and source inductances L_g, L_d, and L_s, respectively, were not altered from their starting values since changing them did not measurably impact the results of the noise modeling.

Representative frequency-dependent results of the model are plotted in Figs. 3.3(a) and 3.3(b). The modeled and measured gain are in agreement over the full frequency range, and the model captures the overall trend in noise temperature as a function of both temperature and bias.

We used this model to extract the gate temperature T_g under various conditions. Figure 3.6(a) shows the extracted T_g versus T_{phys} at the device's low-noise bias of P_{DC} = 24.5 mW mm^{-1}. T_g is elevated above T_{phys} below 20 K even in the presence of superfluid, and follows T_{phys} above 20 K, behavior which is in agreement with prior reports [28, 60, 61]. Figure 3.6(b) shows T_g versus P_{DC} at T_{phys} = 1.6 K physical temperature. Here, T_g changes by less than 2 K for bias powers below 50 –

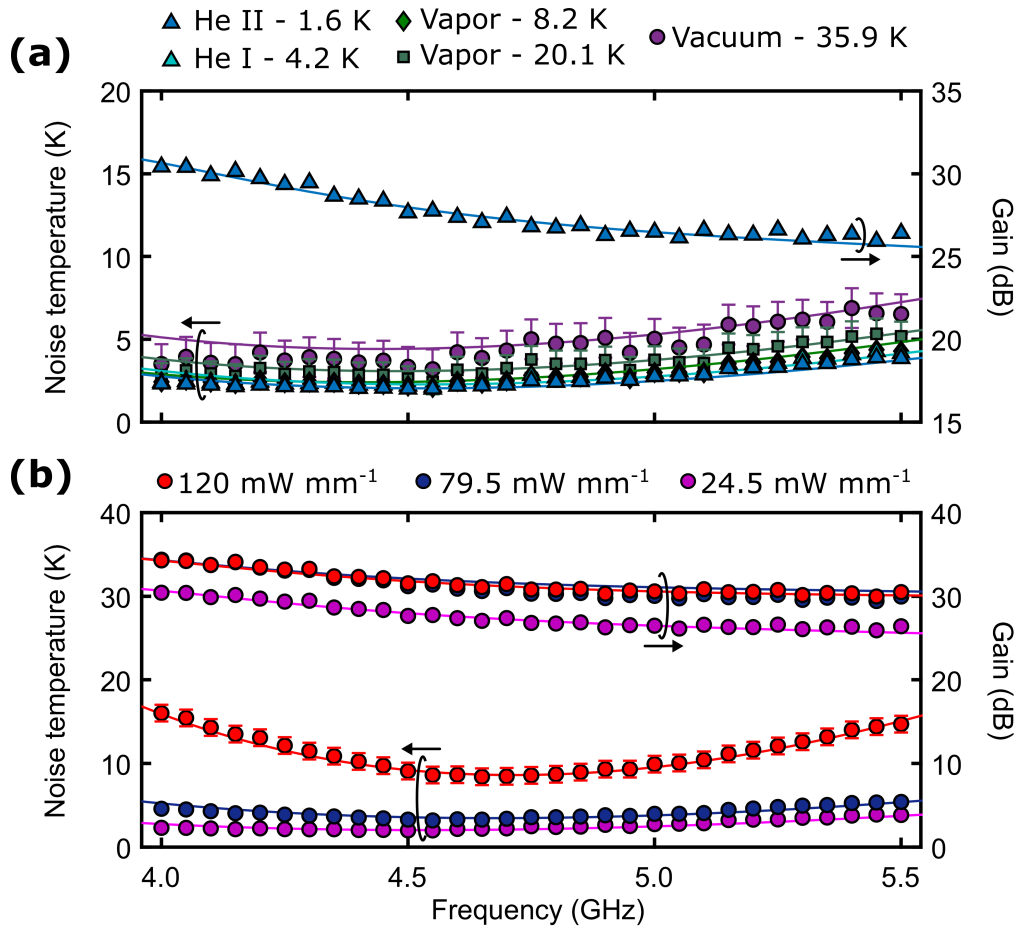

Fig. 3.3: **(a)** Noise temperature (left axis) and gain (right axis) versus frequency, measured at the device's low-noise bias of P_{DC} = 24.5 mW mm^{-1} (V_{DS} = 0.56 V, I_{DS} = 43.9 mA mm^{-1}, V_{GS} = −2.7 V) in the following cryogenic environments: 1.6 K He II (blue triangles), 4.2 K He I (cyan triangles), 8.2 K vapor (green diamonds), 20.1 K vapor (green squares), and 35.9 K vacuum (purple circles). Only the gain under He II conditions is shown for clarity since the gain varies by less than 0.5 dB across all temperatures. The small-signal model fits for each dataset is also shown (solid lines). **(b)** Noise temperature (left axis) and gain (right axis) versus frequency measured at biases of P_{DC} = 24.5 mW mm^{-1} (magenta circles; V_{DS} = 0.56 V, I_{DS} = 43.9 mA mm^{-1}, V_{GS} = −2.7 V), P_{DC} = 79.5 mW mm^{-1} (dark blue circles; V_{DS} = 1.0 V, I_{DS} = 79.5 mA mm^{-1}, V_{GS} = −2.7 V), and P_{DC} = 120 mW mm^{-1} (red circles; V_{DS} = 1.2 V, I_{DS} = 100.0 mA mm^{-1}, V_{GS} = −2.7 V) with the DUT submerged in He II at 1.6 K. To vary the bias, the gate-source voltage was held constant at V_{GS} = −2.7 V while the drain-source voltage V_{DS} was varied. The small-signal model fits (solid lines) are also shown. Where omitted in both **(a)** and **(b)**, the vertical error bars are equal to the height of the symbols.

75 mW mm^{-1}, after which T_g increases more rapidly.

We also used the model to extract the drain temperature T_d under various conditions.

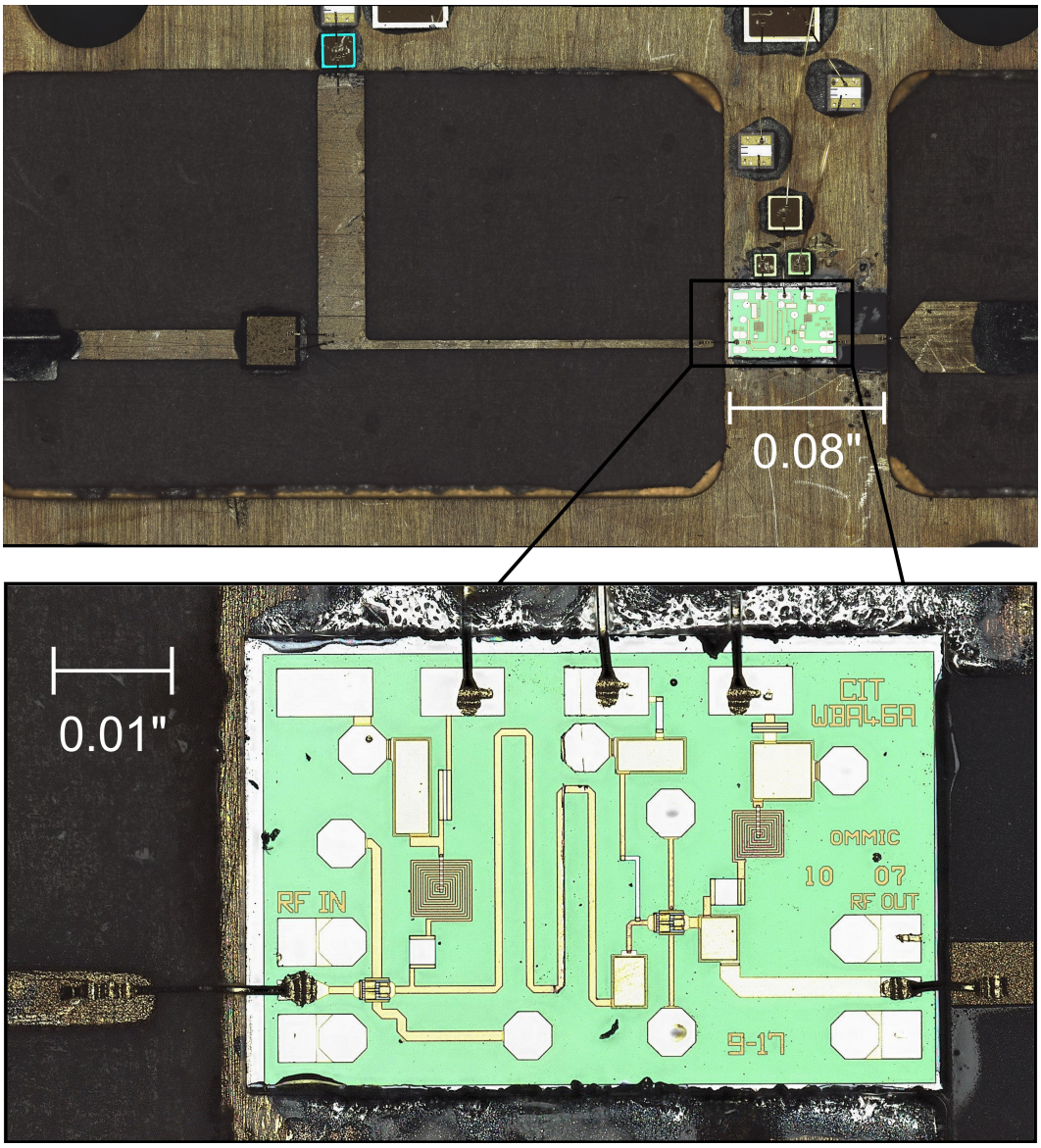

Fig. 3.4: High-resolution micrograph image of the packaged device including the input matching network and MMIC. The inset shows a zoom of the MMIC fabricated by OMMIC.

Figure 3.7(a) shows the extracted drain temperature T_d versus T_{phys} under the same bias conditions as in Fig. 3.6(a). A linear fit is also plotted for reference. The drain temperature follows this linear trend for all physical temperatures measured here, although we emphasize the magnitude of the uncertainty caused by the complexity of modeling a packaged device without access to a full S-pars characterization at these temperatures. Figure 3.7(b) shows T_d versus P_{DC} under the same conditions as in Fig. 3.6(b). The trend in T_d shows reasonable agreement with measurements of similar HEMTs in the literature (see Fig. 5 of Ref. [22] and Fig. 5 of Ref. [35])

as well as with the predictions of recent modeling of drain noise using real-space transfer (see Fig. 3.(a) of Ref. [57]); however, we emphasize that those studies use a fixed $V_{\rm DS}$ with $V_{\rm GS}$ used to change $I_{\rm DS}$.

3.3 Comparison with a phonon radiation model

We compare these results with an equivalent circuit radiation model of the HEMT structure developed in [62]. The explicit functional form for the gate temperature derived from this model is:

$$T_{\rm g}(T_{\rm s}, P_{\rm DC}) = \left(T_{\rm s}^4 + \frac{P_{\rm DC}\mathscr{R}_{cs}\mathscr{R}_{gs}}{\sigma_p(\mathscr{R}_{cs} + \mathscr{R}_{gc} + \mathscr{R}_{gs})} \right)^{1/4} \tag{3.1}$$

where $T_{\rm s}$ is the substrate temperature, $\sigma_p = 850$ W m^{-2} K^{-4} is the equivalent Stefan–Boltzmann constant for phonons in GaAs, and $\mathscr{R}_{ij} = A_i F_{ij}$ is the space resistance between nodes i and j with emitting line length A_i and view factor F_{ij} which quantifies the fraction of power emitted from surface i that intercepts surface j. The subscripts g, c, and s represent the gate, channel, and substrate, respectively. Following Ref. [45], we take $A_{\rm g} = A_{\rm c} = 70$ nm and compute $F_{gc} = 0.3$.

The predictions of Eq. (3.1) are also shown in Figs. 3.6(a) and 3.6(b). In Fig. 3.6(a) the data and model are in quantitative agreement over the full range of physical temperatures. The model captures the elevated gate temperature behavior at fixed bias. In Fig. 3.6(b) the data and model agree at biases below 50 mW mm^{-1}, but the data deviates sharply from the model above some critical bias between 25–50 mW

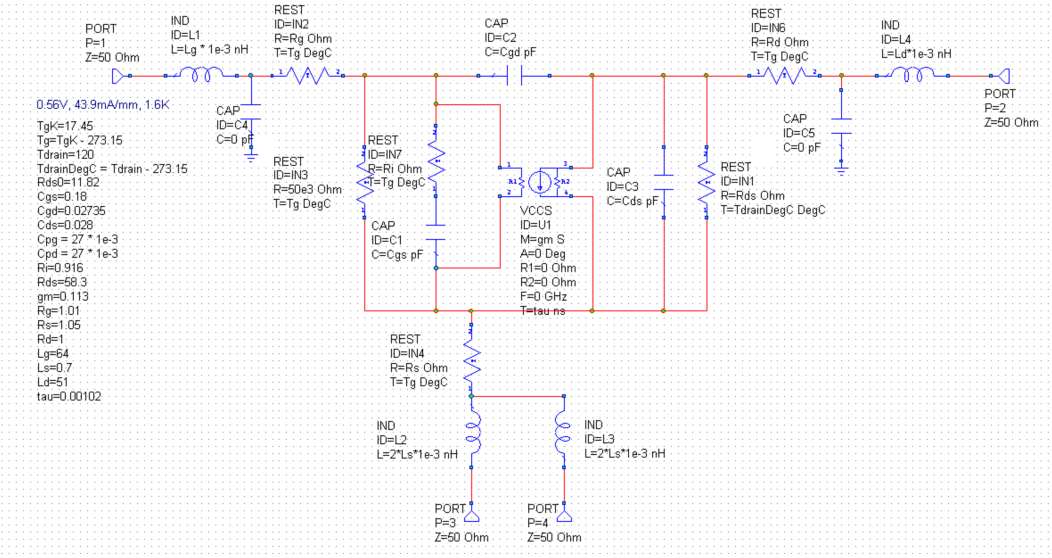

Fig. 3.5: Schematic of the transistor model made using Microwave Office.

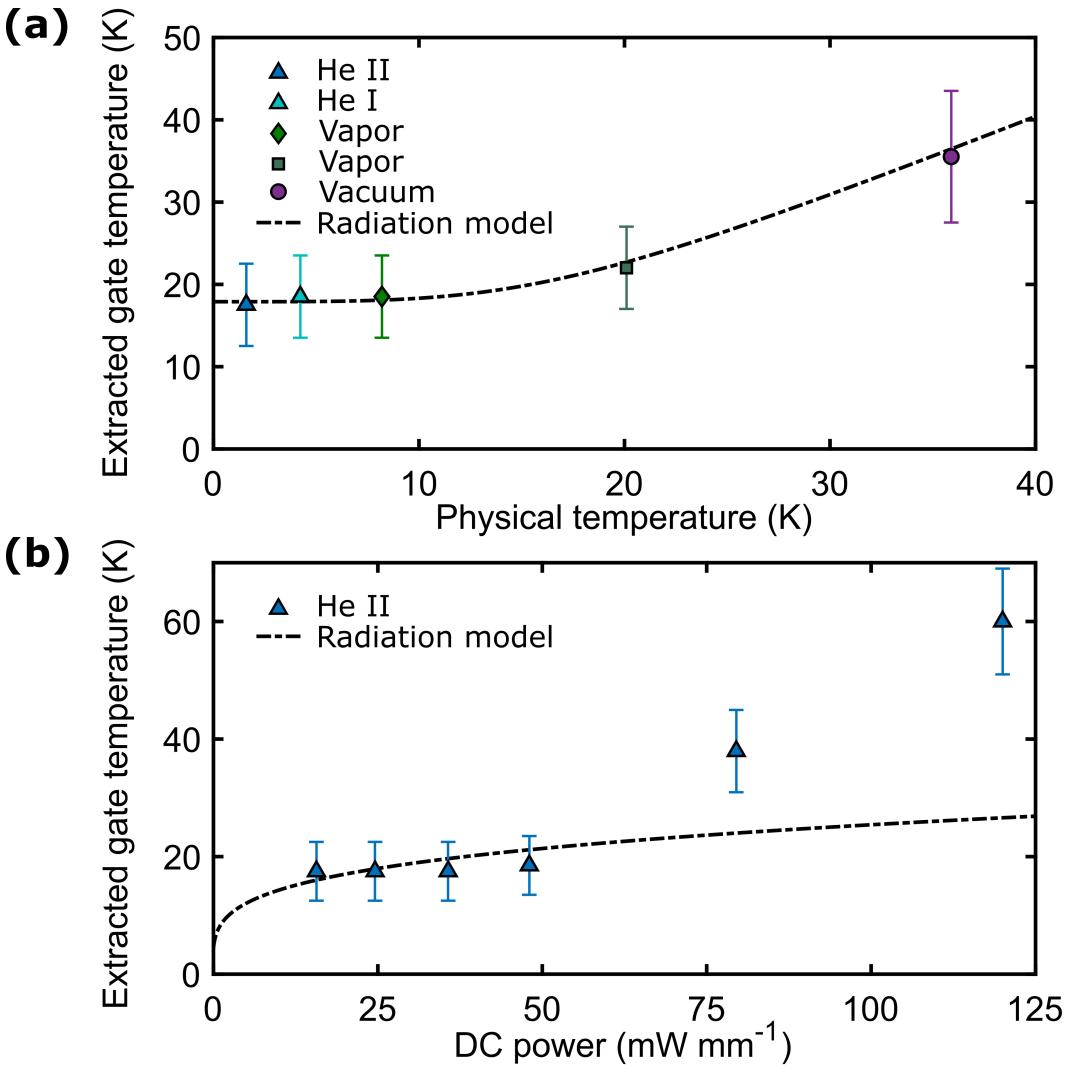

Fig. 3.6: **(a)** Extracted gate temperature versus physical temperature at the device's low-noise bias of P_{DC} = 24.5 mW mm^{-1}. Symbols indicate extracted values and represent the same conditions as in Fig. 3.3(a), along with extracted values in 4.2 K He I (cyan triangles) and 8.1 K vapor (green diamonds). The radiation model is also shown (dash-dotted black line). **(b)** Extracted gate temperature versus bias at 1.6 K physical temperature (blue triangles). The radiation model is also shown (dash-dotted black line). In both **(a)** and **(b)** the error bars were generated by determining the range of gate temperatures that accounted for the uncertainty in the frequency-dependent noise temperature data.

mm^{-1}. The origin of this discrepancy is presently unclear. A possible explanation is that other noise sources are being attributed to gate thermal noise leading to artificially high extracted gate temperatures. This additional noise may signal the onset of impact ionization [143, 144]; however, the usual indications of this process, such as increased gate-leakage current and decreased gain, were not observed. The

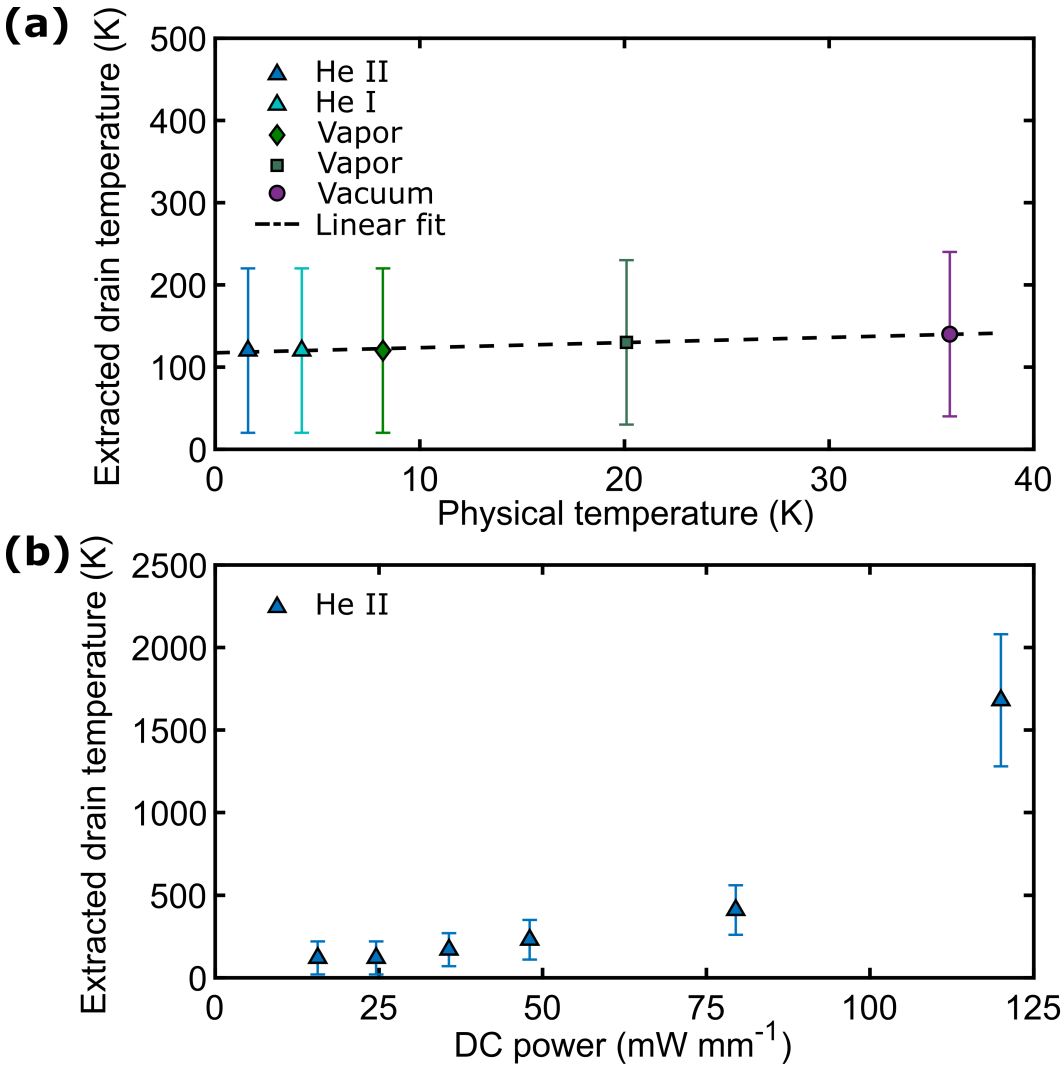

Fig. 3.7: **(a)** Extracted drain temperature versus physical temperature generated from the same extraction process as in Fig. 3.6(a). A linear fit is also shown (dashed black line). **(b)** Extracted drain temperature versus bias generated from the same extraction process as in Fig. 3.6(b). In both **(a)** and **(b)** the error bars were generated by determining the range of drain temperatures that accounted for the uncertainty in the frequency-dependent noise temperature data.

gain plateaued at 33 dB at the highest measured bias, as shown in Fig. 3.3(b), and the gate current remained less than 100 μA at all biases. This discrepancy remains a topic of investigation.

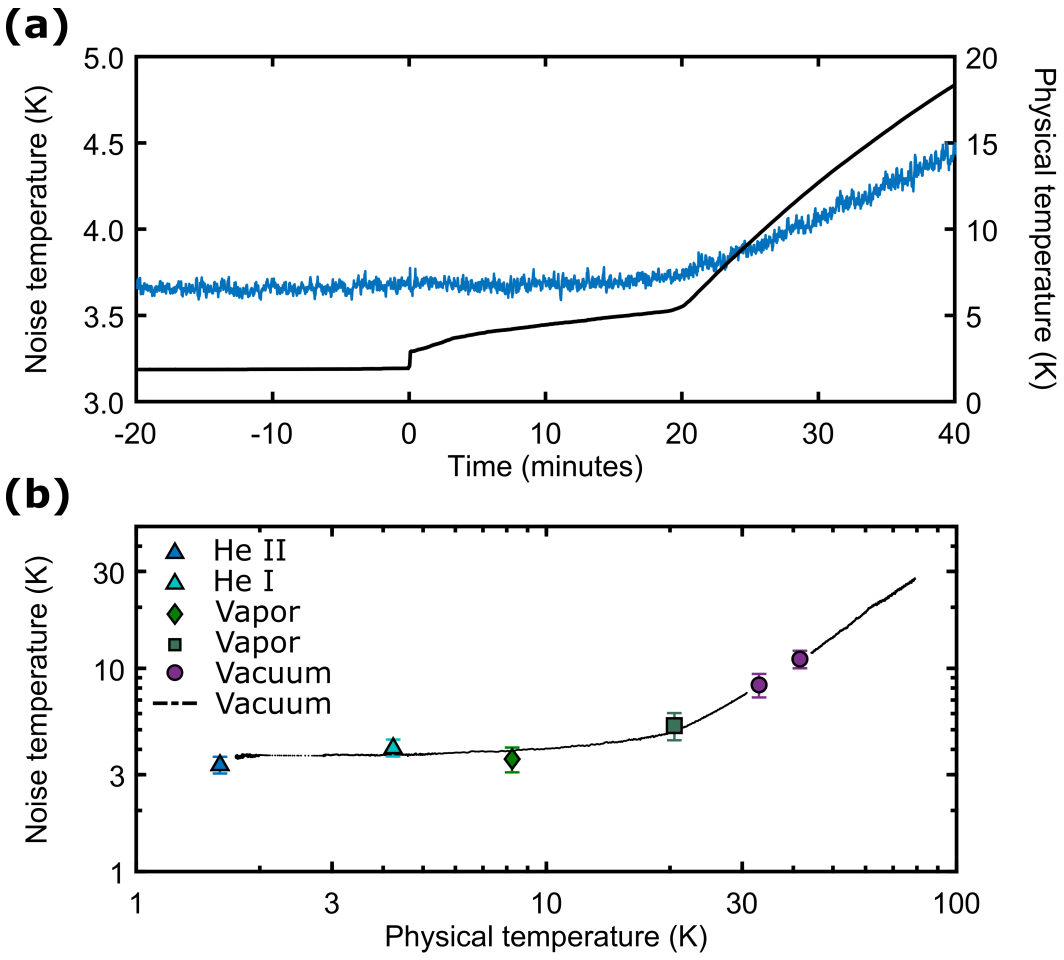

Fig. 3.8: **(a)** Noise temperature (left axis, blue line) and physical temperature (right axis, black line) versus time in an evaporating He II bath sampled at $f_{\mathrm{ENR}} = 10$ Hz and digitally filtered at 1 Hz, taken at a fixed bias $P_{\mathrm{DC}} = 80$ mW mm^{-1} ($V_{\mathrm{DS}} = 1.0$ V, $I_{\mathrm{DS}} = 80$ mA mm^{-1}, $V_{\mathrm{GS}} = -2.8$ V) and frequency $f = 4.55$ GHz. The sharp kink in the physical temperature at time $t = 0$ minutes, interpreted as the time at which superfluid is no longer present on the attenuator and device, is not reflected in the noise temperature. **(b)** Noise temperature (black line) versus physical temperature obtained from the transient data shown in **(a)**. Symbols show independently measured noise temperatures representing the same bath conditions as in Fig. 3.3(a), and the same bias conditions as in **(a)**. The presence of liquid cryogens does not affect the noise temperature within the measurement uncertainty.

3.4 Noise temperature dependence on cryogenic environment

We obtain further insight into how liquid cryogens impact HEMT noise performance by examining the DUT noise temperature measured continuously in a changing cryogenic environment. Figure 3.8(a) shows the time series of both T_e and T_{phys} measured continuously as the He II was pumped out of the measurement dewar, with $t = 0$ minutes chosen as a reference time at which a rise in T_{phys} was observed, interpreted as the departure of superfluid from the attenuator and device. A corresponding feature in the DUT noise temperature is absent. After $t = 0$ minutes the device thermalized with the surrounding ^{4}He vapor, and T_e was observed to increase smoothly with increasing physical temperature. After 20 minutes, the remaining He II liquid below the stage fully evaporated, and the warming rate increased as the mounting stage and DUT passively warmed to room temperature through the mounting apparatus.

In Fig. 3.8(b) the warming curve of T_e plotted against T_{phys} is shown from 1.6 K to 80 K, taken from the time series in Fig. 3.8(a). Again, the noise temperature measured in vacuum exhibits no sharp features, instead smoothly varying with physical temperature. Also plotted are noise temperatures measured separately under various bath conditions, at the same bias and frequency. The discontinuity in vacuum data reflects the period of time during which continuous measurement was paused, and frequency and bias dependent data were acquired. We note that the liquid, vapor, and vacuum data all lie within the reported error bars of the warming curve. These observations suggest that the liquid and vapor cryogen environments provide no self-heating mitigation beyond maintaining a fixed ambient temperature.

3.5 Measurement uncertainty analysis

We estimate the contribution of each quantity in Eq. (2.6) to the overall noise temperature measurement uncertainty ΔT_e, as given by the standard error propagation formula:

$$\Delta T_e^X = \left|\frac{\partial T_e}{\partial X}\right| \Delta X \tag{3.2}$$

where X denotes the measurement error source. All individual error sources are assumed to be independent unless otherwise stated, and are added in quadrature to estimate the overall uncertainty. Numerical estimates listed below assume a noise temperature of $T_e = 2$ K. We assume that each VNA loss measurement has an uncertainty of ±0.01 dB, which is the magnitude of the variation in the measured loss versus frequency of the calibration cable immediately after calibration. We

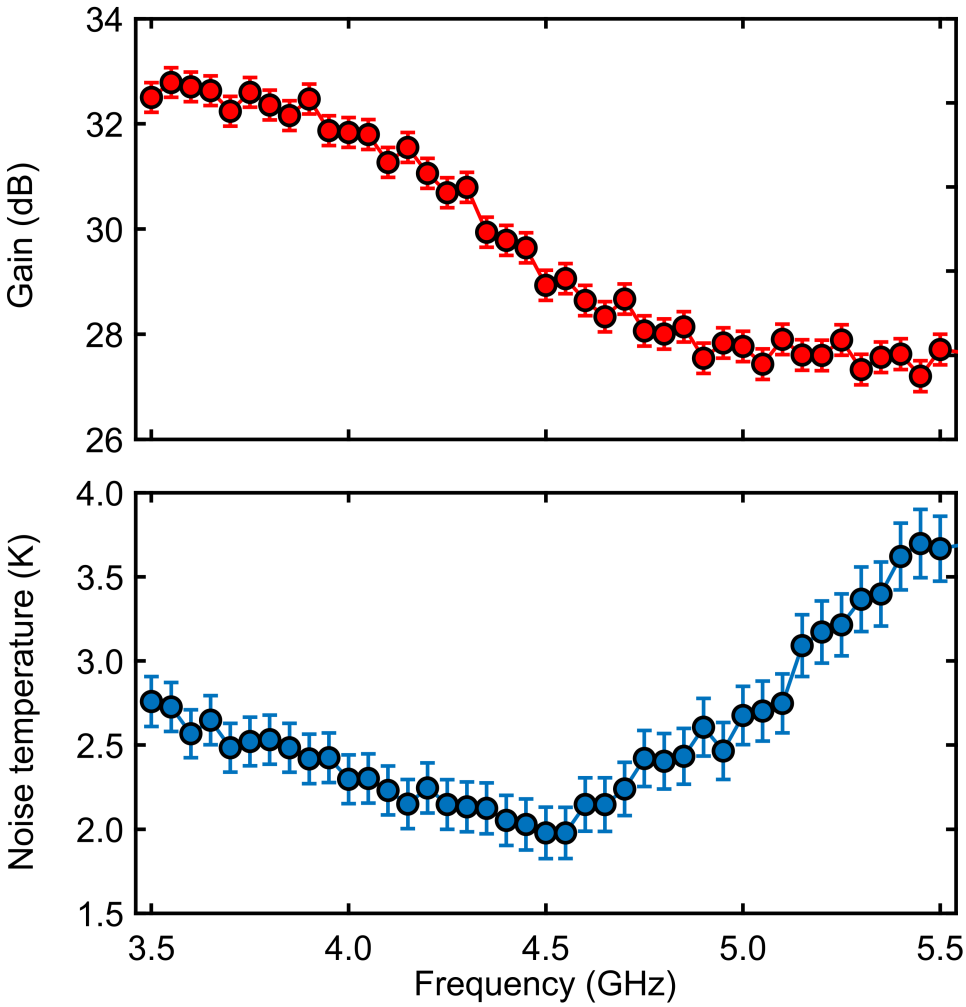

Fig. 3.9: Gain (top plot) and noise temperature (bottom plot) versus frequency measured with the device biased at its low-noise bias of P_{DC} = 24.5 mW (V_{DS} = 0.56 V, I_{DS} = 43.9 mA mm^{-1}, V_{GS} = −2.7 V). The approximately quadratic shape of the noise temperature curve is determined by the IMN.

also assume that the variance in the measured losses across different calibration and measurement dewars is 0.03 dB.

In Fig. 3.9 we illustrate the level of precision of our measurements by plotting the noise temperature and gain measured under the lowest noise conditions achieved in this experiment, at the low-noise bias of of P_{DC} = 24.5 mW mm^{-1} with the device submerged in He II at 1.6 K. The error bars were generated from the uncertainty analysis outlined below.

Attenuator

The uncertainty in the attenuator loss ΔL_2 is found by adding the uncertainty from the VNA measurements in calibration dewars 1 and 2 in quadrature, so that $\Delta L_2 = 0.05 dB$.

$$\left|\frac{\partial T_e}{\partial L_2}\right| = \frac{T_e + T_{L_2}}{L_2}$$
$$\Delta T_e^{L_2} = 0.036 \text{ K}$$

The uncertainty in the attenuator temperature T_{L_2} is determined by the temperature diode calibration. The calibrated Lake Shore DT-670-SD bonded to the attenuator chip has a manufacturer-reported temperature uncertainty of $\Delta T_{L_2} = \pm 20$ mK.

$$\left|\frac{\partial T_e}{\partial T_{L_2}}\right| = \frac{L_2 - 1}{L_2}$$
$$\Delta T_e^{T_{L_2}} = 0.020 \text{ K}$$

Coaxial cables

The uncertainties in the coaxial cable losses ΔL_1 and ΔL_3 are found by adding the uncertainties from three separate VNA loss measurements: the measurement of $L_{\text{coax}} = L_1 L_3$ in calibration dewar 1, and the measurements of L_1 and L_3 at room temperature to determine the loss asymmetry between the two cables, yielding $\Delta L_1 = 0.06$ dB and $\Delta L_3 = 0.07$ dB.

$$\left|\frac{\partial T_e}{\partial L_1}\right| = \frac{T_e + T_{L_1} L_2^{-1} + T_{L_2}(L_2 - 1) L_2^{-1}}{L_1}$$
$$\Delta T_e^{L_1} = 0.088 \text{ K}$$

$$\left|\frac{\partial T_e}{\partial L_3}\right| = \frac{T_{L_3}}{G_{\text{full}} L_1 L_2 L_3^2}$$
$$\Delta T_e^{L_3} = 0.006 \text{ K}$$

The uncertainty in the cable temperatures ΔT_{L_1} and ΔT_{L_3} are derived from error analysis of Eq. (2.17). We estimate $\Delta T_{\text{coax}} = \pm 20$ K.

$$\left|\frac{\partial T_e}{\partial T_{L_1}}\right| = \frac{L_1 - 1}{L_1 L_2}$$
$$\Delta T_e^{T_{L_1}} = 0.100 \text{ K}$$

$$\left|\frac{\partial T_e}{\partial T_{L_3}}\right| = \frac{L_3 - 1}{G_{\text{full}} L_1 L_2 L_3}$$
$$\Delta T_e^{T_{L_3}} = 0.032 \text{ K}$$

Gain

The uncertainty in the total gain ΔG_{full} comes directly from the uncertainty of a single VNA loss measurement so that $\Delta G_{\text{full}} = \pm 0.01$ dB.

$$\left|\frac{\partial T_e}{\partial G_{\text{full}}}\right| = \frac{T_{\text{coax}}(L_3 - 1)L_3^{-1} + T_{\text{BE}}}{L_1 L_2 G_{\text{full}}^2}$$
$$\Delta T_e^{G_{\text{full}}} = 0.002 \text{ K}$$

Backend detector

The uncertainty in the backend detector noise temperature ΔT_{BE} is determined by the temperature and loss uncertainties in the coaxial cable connecting the cooled load to the backend. We estimate $\Delta T_{\text{BE}} = \pm 5$ K.

$$\left|\frac{\partial T_e}{\partial T_{\text{BE}}}\right| = \frac{1}{G_{\text{full}} L_1 L_2}$$
$$\Delta T_e^{\text{BE}} = 0.016 \text{ K}$$

Noise source

The uncertainty in the noise source ENR comes from error analysis of Eq. (2.14). We estimate $\Delta E = \pm 0.040$ dB.

$$\left|\frac{\partial T_e}{\partial E}\right| = \frac{T_0}{(Y - 1)L_1 L_2}$$
$$\Delta T_e^{E} = 0.073 \text{ K}$$

The uncertainty in the noise source diode temperature ΔT_{C} comes from the uncertainty in the Type T thermocouple temperature measurement of the noise source chassis. We estimate $\Delta T_{\text{C}} = 1$ K.

$$\left|\frac{\partial T_e}{\partial T_{\text{C}}}\right| = \frac{1}{L_1 L_2}$$
$$\Delta T_e^{E} = 0.005 \text{ K}$$

Y-factor power

The Y-factor measurement uncertainty ΔY accounts for all uncertainty sources originating after the transduction of microwave power to DC voltage. We report an

effective normalized Y-factor error $\frac{\Delta Y}{Y}$ of better than 3×10^{-4} for a 4 s integration time, which used for all steady-state data presented in this paper.

$$\left|\frac{\partial T_e}{\partial Y}\right| = \frac{T_0 E}{L_1 L_2 (Y-1)^2}$$
$$\Delta T_e^{\mathrm{Y}} = 0.003 \text{ K}$$

Cable mismatch

There is error introduced from the difference in noise source impedance between the on and off state, which causes a changing reflection coefficient between the noise source and the first component in the measurement chain (in our experiment this is the input coaxial cable). In cases where the impedance match at the output of the noise source is poor, this error must be considered, and can be corrected for if the full S-parameters of the noise source in the on and off state and of the cable are known. This correction procedure is outlined in Appendix A. In our experiment this error was found to contribute negligibly to the overall uncertainty.

Overall uncertainty

The uncertainty budget is shown in Table 3.1. The uncertainty analysis shown in this section was used to generate the error bars in the primary noise temperature datasets.

Error Source	Value	Estimated Error	Contribution to T_e
L_2	20.00 dB	0.05 dB	0.036 K
T_2	1.600 K	0.020 K	0.020 K
L_1	3.25 dB	0.06 dB	0.088 K
L_3	3.44 dB	0.07 dB	0.006 K
T_1	223 K	20 K	0.100 K
T_3	223 K	20 K	0.032 K
G_{full}	1.98 dB	0.01 dB	0.002 K
T_{BE}	170 K	5.0 K	0.016 K
E	15.0 dB	0.040 dB	0.073 K
T_{C}	301.0 K	1 K	0.009 K
Y	6.8	0.002	0.003 K
RMS Sum			0.162 K

Table 3.1: Table of parameters used to extract T_e, along with their associated uncertainties.

3.6 Limits on thermal conductance at the helium-gate interface

We consider the finding that He II is unable to mitigate self-heating in the context of He II transport. In Section 1.3 we made predictions of the order of magnitude of the heat fluxes between the HEMT gate surface and He II. The persistence of an elevated gate temperature irrespective of liquid cryogenic environment suggests that our estimates of the predicted heat fluxes being below what is required to extract a significant percentage of the heat produced in the channel were correct. Taking 1 mW as an order of magnitude estimate for the cooling power required to measurably change the noise temperature and making the same assumption for thermal contact area $A = 1\ \mu\text{m} \times 200\ \mu\text{m}$ as in Section 1.3, we estimate the required heat transfer coefficient $h = \dot{Q}(A\Delta T)^{-1}$ to be $h = 250\ \text{kW m}^2\ \text{K}^{-1}$, which is a factor of 10 higher than the highest measured Kapitza resistance between He II and a solid (in this case Hg) [121].

3.7 Implications for noise performance of cryogenic HEMTs

We now examine the implications of our finding that self-heating in HEMTs cannot be mitigated for their noise performance. The only method to reduce gate noise below the observed low-temperature plateau at approximately 20 K is to reduce the dissipated DC power. However, lower power also reduces the gain, which in turn leads to an increase in the contribution of both drain noise and any noise source originating after the gain stage of the HEMT, when referred to the input.

We first explore how T_{min} from the Pospiezalski model [53] varies with bias while including the explicit bias dependencies of both T_{d} and T_{g}. We recall that T_{min} in the limit $f \ll f_T$ [22] is:

$$T_{\text{min}} = g_0 \frac{\sqrt{T_{\text{g}} T_{\text{d}}}}{g_{\text{m}}} \tag{3.3}$$

where we have explicitly introduced the bias independent prefactor $g_0 = 4\pi f(C_{\text{gs}} + C_{\text{gd}})\sqrt{(r_i + R_{\text{G}} + R_{\text{S}})g_{\text{ds}}}$. We assume a $T_{\text{phys}} = 4.2$ K, a gate-source capacitance $C_{\text{gs}} = 150$ fF, a drain-source capacitance $C_{\text{ds}} = 28$ fF, frequency $f = 5$ GHz, a parasitic gate resistance $R_{\text{G}} = 1\ \Omega$, a parasitic source resistance $R_{\text{S}} = 1\ \Omega$, an intrinsic input resistance $r_{\text{i}} = 1\ \Omega$, an intrinsic drain-source conductance $g_{\text{ds}} = 15.4$ mS, and a transconductance g_{m} obtained by taking a finite-difference approximation of the derivative of $I_{\text{DS}} - V_{\text{DS}}$ data for different V_{GS} separated by 20 mV. All values are taken from [58]. We also assume a drain noise temperature that varies linearly from $T_{\text{d}} = 20$ K at $P_{\text{DC}} = 0\ \text{mW mm}^{-1}$ to $T_{\text{d}} = 1000$ K at $P_{\text{DC}} = 68.5\ \text{mW mm}^{-1}$, an approximation of the bias dependence measured in [58], while taking $T_{\text{d}} = 20$ K

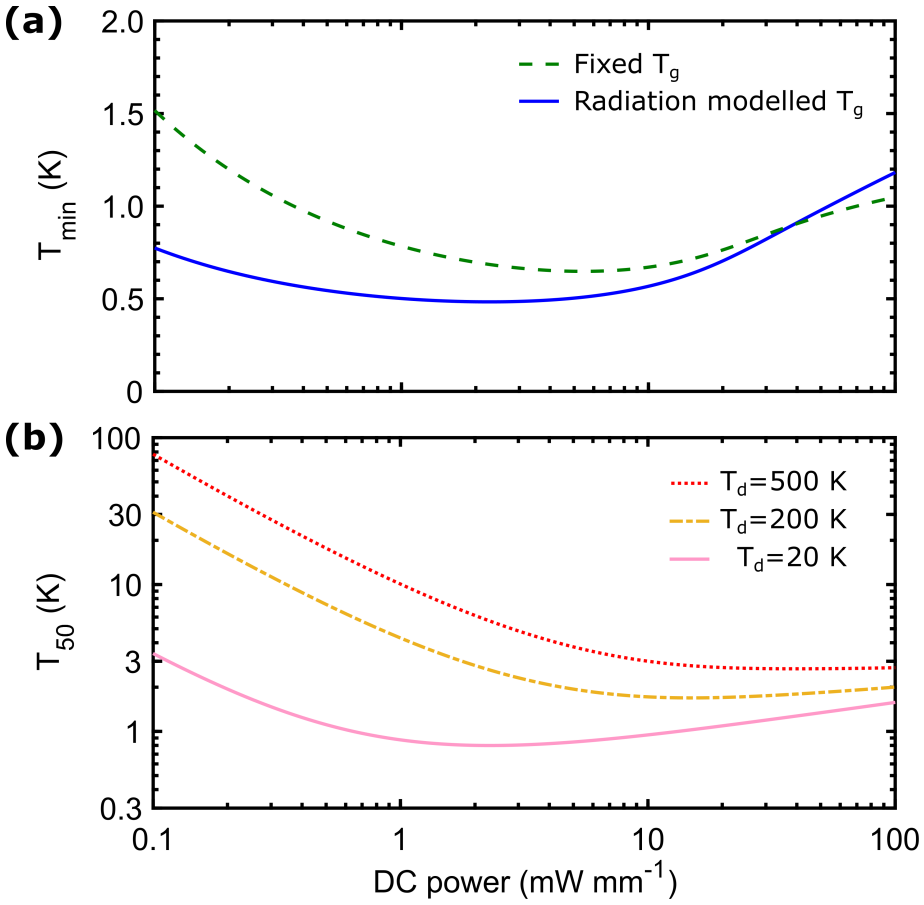

Fig. 3.10: **(a)** Modeled $T_{\rm min}$ versus bias, shown for a fixed gate temperature $T_{\rm g}$ = 20 K (dashed green line) and for a gate temperature with bias dependence determined by a radiation model (solid blue line). The radiation model predicts a gate temperature below 20 K for powers below 40 mW mm^{-1}, which is reflected in $T_{\rm min}$. **(b)** Modeled T_{50} noise temperature versus bias, shown for $T_{\rm d}$ = 500 K (dashed red line), $T_{\rm d}$ = 200 K (dash-dotted gold line), and $T_{\rm d}$ = 20 K (solid pink line). Both the minimum T_{50} and the power required to achieve this minimum decrease with decreasing $T_{\rm d}$.

as the zero-bias limit.

Figure 3.10(a) shows $T_{\rm min}$ versus dissipated power both with and without the $T_{\rm g} \propto P_{\rm DC}^{1/4}$ dependence predicted by the radiation model. For the case of fixed gate temperature we assume $T_{\rm g}$ = 20 K. The radiation model predicts a lower $T_{\rm min}$ than the fixed $T_{\rm g}$ model up to a power of $P_{\rm DC}$ = 15 mW mm^{-1}, above which self-heating raises the gate temperature above 20 K. The minimum $T_{\rm min}$ predicted by the radiation model is lower than that predicted by the fixed model by 0.16 K, and the bias at which the minimum $T_{\rm min}$ occurs is also lower by 2.7 mW mm^{-1}. Below this optimal bias, both models predict an increase in $T_{\rm min}$ with decreasing power, indicating where the gain is insufficient to overcome drain noise.

A reduction in drain noise at low biases is evidently beneficial. We demonstrate the effect such a reduction has on the overall noise temperature by using a phenomenological model that both accounts for self-heating and separates the input and output noise contributions additively, a feature of noisy amplifiers which is not captured in the expression of T_{min}. At low enough frequencies such that $f \ll f_T$, the noise temperature of a HEMT with a 50 Ω source impedance is:

$$T_{50} = \frac{T_{\mathrm{g}}(r_{\mathrm{i}} + R_{\mathrm{G}} + R_{\mathrm{S}}) + T_{\mathrm{d}} g_{\mathrm{ds}} g_{\mathrm{m}}^{-2}}{50\ \Omega} \tag{3.4}$$

as derived in Ref. [38] in the limit of open C_{gs} and C_{gd}. For illustrative purposes, we assume a constant T_{d}, a physical temperature of 4.2 K, and all other parameter values identical to those in the T_{min} model.

Figure 3.10(b) shows the modeled T_{50} noise temperature versus dissipated power at different drain temperatures. Drain temperatures of 500 K and 200 K were chosen to approximate state-of-the-art low-power performance in GaAs devices [58] and InP devices [49], respectively. A knee is observed in each curve, the location of which indicates where the gate noise and input-referred drain noise become comparable in magnitude. As T_{d} is decreased, both the T_{50} value at the knee and the bias at which the knee is observed decrease. This feature is explained as follows. As T_{d} decreases, less gain is required to achieve the same contribution of T_{d} to the overall noise, which implies that less power is required to bias the device, ultimately leading to less self-heating and therefore a lower T_{g}. In this way we see that reducing T_{d} leads to a simultaneous improvement in noise temperature and reduction in optimal low-noise bias.

Chapter 4

SUMMARY AND OUTLOOK

In this work, we evaluated the utility of using liquid cryogens to mitigate the self-heating effect, a limiting noise source in low-noise cryogenic microwave HEMT amplifiers. The primary object of study was a packaged two-stage cryogenic HEMT amplifier. This device, whose noise was measured in various cryogenic environments including liquid superfluid helium-4, did not exhibit improved noise performance beyond what was expected from conventional solid-state conductive cooling strategies. The work presented here demonstrates a contribution to further establishing and understanding the noise limits of cryogenic HEMT amplifiers.

In Chapter 2 we demonstrated the design and construction considerations of our experiment, and showed all calibration procedures which were required. We discussed the vacuum and cryogenic engineering involved in evaporatively cooling the liquid bath of a helium dewar. We provided the details of our microwave noise measurement apparatus, which was based on the cold-attenuator Y-factor method, demonstrating in particular the ability to digitally sample Y-factors at speeds in excess of 600 kHz, limited by the digital sampling rate of our analog-digital converter. The room temperature characterization of our DUT was presented, as were all calibration techniques required to perform the experiment, both at room and cryogenic temperatures. We also outlined the measurement procedure which was followed to characterize the noise performance of our device.

In Chapter 3 we examined the dependence of the device's noise temperature on bias, frequency, physical temperature, and cryogenic environment. We developed a small-signal model of the device which was used to extract its gate temperature and drain temperature. We compared the extracted gate temperatures to the predictions of an equivalent circuit phonon radiation model, and found good agreement over a wide range of cryogenic temperatures and biases. The gate temperature was found to exhibit the same plateau at temperatures below 20 K as has been observed in the overall noise temperature measured both in this work and in other published studies. We also measured the LNA noise temperature as the He II bath in which it was immersed evaporated from the HEMT surface, and found no change in noise temperature within the measurement uncertainty. These observations led us to the

conclusion that self-heating of cryogenic HEMTs cannot be mitigated through direct liquid cooling strategies. This observation was found to be in agreement with our estimates of the He II cooling power accessible to the HEMT gate, based on our approximation of the HEMT surface area and values of the solid-helium boundary thermal conductance available in the literature. We explored the consequences of our null result on the limits of HEMT noise by incorporating the effect of self-heating into noise modelling of FET amplifiers. We found that both the Pospiesalski noise model's prediction of the device's minimum noise temperature, and a phenomenological model of noisy linear amplifiers both predict that a reduction in drain temperature enables simultaneous improvements in noise performance by reducing the gain required to overcome the drain noise, and hence reducing the dissipated power, thereby diminishing the magnitude of self-heating.

4.1 Future work

We outline here the potential direction for future research that extends naturally from the work presented in this thesis, both by suggesting extensions and improvements to the characterization measurements performed here, and by discussing other possible methods of improving HEMT noise performance given the limits imposed by self-heating. Firstly, as discussed in Chapter 2, the cryogenic vacuum engineering can be improved by including an inner vacuum jacket in the pumping line, so that the room temperature vacuum seals do not experience convective cooling from the pumped helium. An alternative is to implement a different design which uses subcooled He II instead of saturated He II. As discussed briefly in Chapter 1, subcooled helium presents several engineering advantages, and at high pressures has been shown to increase the film-boiling heat transfer coefficient h_{fb} in certain surface geometries (see Table 7.5 of Ref. [63]). A yet more sophisticated apparatus might involve the use of forced-flow convective cooling which has also be shown to increase h_{fb} [69, 101]. Finally, different surface passivisation treatments designed to increase the effective thermal interface area should be explored.

The cold-attenuator Y-factor scheme itself can be improved by moving the noise diode directly to the input of the cold attenuator, eliminating noise contributions from the lossy input coaxial cabling. A coaxially coupled, internally calibrated, packaged noise source capable of continuously variable noise generation from a chip-mounted thermal source which can be operated at cryogenic chassis temperatures is currently in development [145]. A similar device which employs additional noise amplification via a travelling wave parametric amplifier has been successfully

demonstrated in a dilution refrigeration environment [146]. A larger scale improvement would be to design a semiconductor probe-station, commonly employed for full DC and microwave discrete transistor characterization [147], capable of containing a He II bath inside its vacuum assembly. This would enable measurements of discrete HEMTs immersed in He II, enabling a more systematic evaluation of the possible effects of, for example, the use of subcooled He II, increased thermal interface area, etc.

The experimental technique used here to measure LNA noise temperatures in liquid cryogenic environements can also be applied to other LNA technologies. A particular example would be studying the effect of liquid cryogenic cooling on SiGe heterojunction bipolar transistor (HBT) amplifiers, which possess an inherently different structure and whose "self-heating" is expected to occur over a larger physical region than in HEMTs [148].

As already alluded to, our findings bolster the conventional wisdom that low-noise HEMT amplifier design should involve minimizing the power dissipation required to achieve sufficient gain to overcome drain noise. A more rigorous understanding of the physical origins of drain noise should continue [57] so that future device designs can achieve the lowest possible drain temperatures and take full advantage of the conclusions of Chapter 3, that a reduction in drain noise leads to a cascading improvement in noise temperature. Future efforts must incorporate developments from all facets of low-noise amplifier research, including the theory of noise in HEMTs, device fabrication techniques, and precision measurement schemes.

BIBLIOGRAPHY

[1]E. Velmre, "Thomas johann seebeck (1770-1831)", PROCEEDINGS OF THE ESTONIAN ACADEMY OF SCIENCES **13**, 276–282 (2007).

[2]G. Busch, "Early history of the physics and chemistry of semiconductors-from doubts to fact in a hundred years", European Journal of Physics **10**, 254–264 (1989).

[3]L. Lukasiak and A. Jakubowski, "History of semiconductors", Journal of telecommunications and information technology, 3–9 (2010).

[4]L. Hoddeson, ed., *Out of the crystal maze: chapters from the history of solid state physics* (Oxford University Press, New York, 1992), 697 pp.

[5]C. Kittel, P. McEuen, and John Wiley & Sons, *Introduction to solid state physics*, OCLC: 987438137 (2015).

[6]N. W. Ashcroft and N. D. Mermin, *Solid state physics* (Holt, Rinehart and Winston, New York, 1976), 826 pp.

[7]P. Horowitz and W. Hill, *The art of electronics*, Third edition (Cambridge University Press, New York, NY, 2015), 1192 pp.

[8]P. Bondyopadhyay, "Sir j.c. bose diode detector received marconi's first transatlantic wireless signal of december 1901 (the "italian navy coherer" scandal revisited)", Proceedings of the IEEE **86**, Conference Name: Proceedings of the IEEE, 259–285 (1998).

[9]M. Riordan and L. Hoddeson, "The origins of the pn junction", IEEE Spectrum **34**, Conference Name: IEEE Spectrum, 46–51 (1997).

[10]D. Burg and J. H. Ausubel, "Moore's law revisited through intel chip density", PLOS ONE **16**, edited by T. Al-Ameri, e0256245 (2021).

[11]G. L. Arsov, "Celebrating 65th anniversary of the transistor", Electronics ETF **17**, 63–70 (2013).

[12]J. J. Bautista, "Chapter 5 HEMT low-noise amplifiers", in *Low-noise systems in the deep space network*, edited by M. S. Reid, Deep-space communications and navigation series, OCLC: ocn230181178 (Wiley, Hoboken, N.J, 2008), pp. 195–254.

[13]J. A. Pérez-Taborda, O. Caballero-Calero, and M. Martín-González, "Silicon-germanium (SiGe) nanostructures for thermoelectric devices: recent advances and new approaches to high thermoelectric efficiency", in *New research on silicon - structure, properties, technology*, edited by V. I. Talanin (InTech, May 31, 2017).

[14]M. W. Pospieszalski, "Extremely low-noise cryogenic amplifiers for radio astronomy: past, present and future", in 2018 22nd international microwave and radar conference (MIKON) (May 2018), pp. 1–6.

[15]J. Grahn, E. Cha, A. Pourkabirian, J. Stenarson, and N. Wadefalk, "III-v HEMTs for cryogenic low noise amplifiers", in 2020 IEEE international electron devices meeting (IEDM), ISSN: 2156-017X (Dec. 2020), pp. 25.6.1–25.6.4.

[16]L. Esaki and R. Tsu, "Superlattice and negative differential conductivity in semiconductors", IBM Journal of Research and Development **14**, Conference Name: IBM Journal of Research and Development, 61–65 (1970).

[17]R. Dingle, H. L. Störmer, A. C. Gossard, and W. Wiegmann, "Electron mobilities in modulation-doped semiconductor heterojunction superlattices", Applied Physics Letters **33**, 665–667 (1978).

[18]H. Störmer, R. Dingle, A. Gossard, W. Wiegmann, and M. Sturge, "Two-dimensional electron gas at a semiconductor-semiconductor interface", Solid State Communications **29**, 705–709 (1979).

[19]S. Weinreb, "Low-noise cooled GASFET amplifiers", IEEE Transactions on Microwave Theory and Techniques **28**, 1041–1054 (1980).

[20]M. Pospieszalski, S. Weinreb, P.-C. Chao, U. Mishra, S. Palmateer, P. Smith, and J. Hwang, "Noise parameters and light sensitivity of low-noise high-electron-mobility transistors at 300 and 12.5 k", IEEE Transactions on Electron Devices **33**, Conference Name: IEEE Transactions on Electron Devices, 218–223 (1986).

[21]M. Pospieszalski, W. Lakatosh, R. Lai, K. Tan, D. Streit, P. Liu, R. Dia, and J. Velebir, "Millimeter-wave, cryogenically-coolable amplifiers using AlInAs/GaInAs/InP HEMTs", in 1993 IEEE MTT-s international microwave symposium digest, ISSN: 0149-645X (June 1993), 515–518 vol.2.

[22]M. Pospieszalski, "Extremely low-noise amplification with cryogenic FETs and HFETs: 1970-2004", IEEE Microwave Magazine **6**, Conference Name: IEEE Microwave Magazine, 62–75 (2005).

[23]M. Laviron, D. Delagebeaudeuf, P. Delescluse, P. Etienne, J. Chaplart, and N. T. Linh, "Low noise normally on and normally off two-dimensional electron gas field-effect transistors", Applied Physics Letters **40**, 530–532 (1982).

[24]K. Joshin, T. Mimura, M. Ninori, Y. Yamashita, K. Kosemura, and J. Saito, "Noise perfomance of microwave HEMT", in 1983 IEEE MTT-s international microwave symposium digest, ISSN: 0149-645X (May 1983), pp. 563–565.

[25]S. Weinreb, R. Lai, N. Erickson, T. Gaier, and J. Wielgus, "W-band InP wideband MMIC LNA with 30 k noise temperature", in 1999 IEEE MTT-s international microwave symposium digest (cat. no.99ch36282), Vol. 1 (June 1999), 101–104 vol.1.

[26]J. Bautista, J. Bowen, N. Fernandez, Z. Fujiwara, J. Loreman, S. Petty, J. Prater, R. Grunbacher, R. Lai, M. Nishimoto, M. Murti, and J. Laskar, "Cryogenic, x-band and ka-band InP HEMT based LNAs for the deep space network", in 2001 IEEE aerospace conference proceedings (cat. no.01th8542), Vol. 2 (Mar. 2001), 2/829–2/842 vol.2.

[27]M. Varonen, R. Reeves, P. Kangaslahti, L. Samoska, A. Akgiray, K. Cleary, R. Gawande, A. Fung, T. Gaier, S. Weinreb, A. C. S. Readhead, C. Lawrence, S. Sarkozy, and R. Lai, "A 75–116-GHz LNA with 23-k noise temperature at 108 GHz", in 2013 IEEE MTT-s international microwave symposium digest (MTT), ISSN: 0149-645X (June 2013), pp. 1–3.

[28]J. Schleeh, J. Mateos, I. Íñiguez-de-la-Torre, N. Wadefalk, P. A. Nilsson, J. Grahn, and A. J. Minnich, "Phonon black-body radiation limit for heat dissipation in electronics", Nature Materials **14**, 187–192 (2015).

[29]N. Wadefalk, A. Mellberg, I. Angelov, M. Barsky, S. Bui, E. Choumas, R. Grundbacher, E. Kollberg, R. Lai, N. Rorsman, P. Starski, J. Stenarson, D. Streit, and H. Zirath, "Cryogenic wide-band ultra-low-noise if amplifiers operating at ultra-low DC power", IEEE Transactions on Microwave Theory and Techniques **51**, 1705–1711 (2003).

[30]A. H. Akgiray, S. Weinreb, R. Leblanc, M. Renvoise, P. Frijlink, R. Lai, and S. Sarkozy, "Noise measurements of discrete HEMT transistors and application to wideband very low-noise amplifiers", IEEE Transactions on Microwave Theory and Techniques **61**, Conference Name: IEEE Transactions on Microwave Theory and Techniques, 3285–3297 (2013).

[31]J. Schleeh, G. Alestig, J. Halonen, A. Malmros, B. Nilsson, P. A. Nilsson, J. P. Starski, N. Wadefalk, H. Zirath, and J. Grahn, "Ultralow-power cryogenic InP HEMT with minimum noise temperature of 1 k at 6 GHz", IEEE Electron Device Letters **33**, Conference Name: IEEE Electron Device Letters, 664–666 (2012).

[32]J. Schleeh, N. Wadefalk, P. Å. Nilsson, J. P. Starski, G. Alestig, J. Halonen, B. Nilsson, A. Malmros, H. Zirath, and J. Grahn, "Cryogenic 0.5–13 GHz low noise amplifier with 3 k mid-band noise temperature", in 2012 IEEE/MTT-s international microwave symposium digest, ISSN: 0149-645X (June 2012), pp. 1–3.

[33]E. Cha, N. Wadefalk, P.-Å. Nilsson, J. Schleeh, G. Moschetti, A. Pourkabirian, S. Tuzi, and J. Grahn, "0.3–14 and 16–28 GHz wide-bandwidth cryogenic MMIC low-noise amplifiers", IEEE Transactions on Microwave Theory and Techniques **66**, Conference Name: IEEE Transactions on Microwave Theory and Techniques, 4860–4869 (2018).

[34]D. Cuadrado-Calle, D. George, G. A. Fuller, K. Cleary, L. Samoska, P. Kangaslahti, J. W. Kooi, M. Soria, M. Varonen, R. Lai, and X. Mei, "Broadband MMIC LNAs for ALMA band 2+3 with noise temperature below 28 k", IEEE Transactions on Microwave Theory and Techniques **65**, Conference Name: IEEE Transactions on Microwave Theory and Techniques, 1589–1597 (2017).

[35]F. Heinz, F. Thome, A. Leuther, and O. Ambacher, "Noise performance of sub-100-nm metamorphic HEMT technologies", in 2020 IEEE/MTT-s international microwave symposium (IMS), ISSN: 2576-7216 (Aug. 2020), pp. 293–296.

[36]M. Brozel, "Gallium arsenide", in *Springer handbook of electronic and photonic materials*, edited by S. Kasap and P. Capper (Springer US, Boston, MA, 2006), pp. 499–536.

[37]M. Arps, H.-G. Each, W. Passenberg, A. Umbach, and W. Schlaak, "Influence of SiN/sub x/ passivation on the surface potential of GaInAs and AlInAs in HEMT layer structures", in Proceedings of 8th international conference on indium phosphide and related materials (1996), pp. 308–311.

[38]A. H. Akgiray, "New technologies driving decade-bandwidth radio astronomy: quad-ridged flared horn and compound-semiconductor LNAs", Medium: PDF Version Number: Final, PhD thesis (California Institute of Technology, May 7, 2013).

[39]E. F. Schubert, "Delta doping of III–v compound semiconductors: fundamentals and device applications", Journal of Vacuum Science & Technology A: Vacuum, Surfaces, and Films **8**, 2980–2996 (1990).

[40]A. Leuther, A. Tessmann, I. Kallfass, R. Losch, M. Seelmann-Eggebert, N. Wadefalk, F. Schafer, J. D. Gallego Puyol, M. Schlechtweg, M. Mikulla, and O. Ambacher, "Metamorphic HEMT technology for low-noise applications", in 2009 IEEE international conference on indium phosphide & related materials (May 2009), pp. 188–191.

[41]J. J. Komiak, P. M. Smith, K. H. G. Duh, D. Xu, and P. C. Chao, "Metamorphic HEMT technology for microwave, millimeter-wave, and submillimeter-wave applications", in 2013 IEEE compound semiconductor integrated circuit symposium (CSICS) (Oct. 2013), pp. 1–4.

[42]J. Schleeh, "Cryogenic ultra-low noise inP high electron mobility transistors", PhD thesis (Chalmers Univ. of Technology, Göteborg, 2013), 127 pp.

[43]E. Cha, "InP high electron mobility transistors for cryogenic low noise and low power amplifiers", ISBN: 9789179054076 OCLC: 1240756548, PhD thesis (Chalmers Univ. of Technology, Göteborg, 2020).

[44]C.-C. Chiong, Y. Wang, K.-C. Chang, and H. Wang, "Low-noise amplifier for next-generation radio astronomy telescopes: review of the state-of-the-art cryogenic LNAs in the most challenging applications", IEEE Microwave Magazine **23**, Conference Name: IEEE Microwave Magazine, 31–47 (2022).

[45]A. Y. Choi, "Investigation of electronic fluctuations in semiconductor materials and devices through first-principles simulations and experiments in transistor amplifiers", Medium: PDF Version Number: Final, PhD thesis (California Institute of Technology, Jan. 4, 2022).

[46]J. M. Chow, J. M. Gambetta, E. Magesan, D. W. Abraham, A. W. Cross, B. R. Johnson, N. A. Masluk, C. A. Ryan, J. A. Smolin, S. J. Srinivasan, and M. Steffen, "Implementing a strand of a scalable fault-tolerant quantum computing fabric", Nature Communications **5**, 4015 (2014).

[47]J. M. Hornibrook, J. I. Colless, I. D. Conway Lamb, S. J. Pauka, H. Lu, A. C. Gossard, J. D. Watson, G. C. Gardner, S. Fallahi, M. J. Manfra, and D. J. Reilly, "Cryogenic control architecture for large-scale quantum computing", Physical Review Applied **3**, 024010 (2015).

[48]P. Krantz, M. Kjaergaard, F. Yan, T. P. Orlando, S. Gustavsson, and W. D. Oliver, "A quantum engineer's guide to superconducting qubits", Applied Physics Reviews **6**, 021318 (2019).

[49]E. Cha, N. Wadefalk, G. Moschetti, A. Pourkabirian, J. Stenarson, and J. Grahn, "A 300-μw cryogenic HEMT LNA for quantum computing", in 2020 IEEE/MTT-s international microwave symposium (IMS), ISSN: 2576-7216 (Aug. 2020), pp. 1299–1302.

[50]J. C. Bardin, D. H. Slichter, and D. J. Reilly, "Microwaves in quantum computing", IEEE Journal of Microwaves **1**, Conference Name: IEEE Journal of Microwaves, 403–427 (2021).

[51]J. Aumentado, "Superconducting parametric amplifiers: the state of the art in josephson parametric amplifiers", IEEE Microwave Magazine **21**, Conference Name: IEEE Microwave Magazine, 45–59 (2020).

[52]F. Arute, K. Arya, R. Babbush, D. Bacon, J. C. Bardin, R. Barends, R. Biswas, S. Boixo, F. G. S. L. Brandao, D. A. Buell, B. Burkett, Y. Chen, Z. Chen, B. Chiaro, R. Collins, W. Courtney, A. Dunsworth, E. Farhi, B. Foxen, A. Fowler, C. Gidney, M. Giustina, R. Graff, K. Guerin, S. Habegger, M. P. Harrigan, M. J. Hartmann, A. Ho, M. Hoffmann, T. Huang, T. S. Humble, S. V. Isakov, E. Jeffrey, Z. Jiang, D. Kafri, K. Kechedzhi, J. Kelly, P. V. Klimov, S. Knysh, A. Korotkov, F. Kostritsa, D. Landhuis, M. Lindmark, E. Lucero, D. Lyakh, S. Mandrà, J. R. McClean, M. McEwen, A. Megrant, X. Mi, K. Michielsen, M. Mohseni, J. Mutus, O. Naaman, M. Neeley, C. Neill, M. Y. Niu, E. Ostby, A. Petukhov, J. C. Platt, C. Quintana, E. G. Rieffel, P. Roushan, N. C. Rubin, D. Sank, K. J. Satzinger, V. Smelyanskiy, K. J. Sung, M. D. Trevithick, A. Vainsencher, B. Villalonga, T. White, Z. J. Yao, P. Yeh, A. Zalcman, H. Neven, and J. M. Martinis, "Quantum supremacy using a programmable superconducting processor", Nature **574**, 505–510 (2019).

[53]M. W. Pospieszalski, "Modeling of noise parameters of MESFETs and MODFETs and their frequency and temperature dependence", IEEE Transactions on Microwave Theory and Techniques **37**, Conference Name: IEEE Transactions on Microwave Theory and Techniques, 1340–1350 (1989).

[54]H. Statz, H. Haus, and R. Pucel, "Noise characteristics of gallium arsenide field-effect transistors", IEEE Transactions on Electron Devices **21**, Conference Name: IEEE Transactions on Electron Devices, 549–562 (1974).

[55]M. W. Pospieszalski, "On the limits of noise performance of field effect transistors", in 2017 IEEE MTT-s international microwave symposium (IMS) (June 2017), pp. 1953–1956.

[56]T. Gonzalez, O. M. Bulashenko, J. Mateos, D. Pardo, L. Reggiani, and J. M. Rubi, "Noise suppression due to long-range coulomb interaction: crossover between diffusive and ballistic transport regimes", Semiconductor Science and Technology **12**, 1053–1056 (1997).

[57]I. Esho, A. Y. Choi, and A. J. Minnich, "Theory of drain noise in high electron mobility transistors based on real-space transfer", Journal of Applied Physics **131**, 085111 (2022).

[58]B. Gabritchidze, K. Cleary, J. Kooi, I. Esho, A. Readhead, and A. J. Minnich, "Experimental characterization of temperature-dependent microwave noise of discrete HEMTs: drain noise and real-space transfer", in 2022 IEEE/MTT-s international micowave symposium (IMS), (In print) (June 2022).

[59]J. J. Bautista and E. M. Long, "Physical temperature of the active region in cryogenically cooled indium phosphide high-electron mobility transistors", Interplanetary Network Progress Report **42-170**, ADS Bibcode: 2007IPNPR.170D...1B, 1–9 (2007).

[60]K. Duh, W. Kopp, P. Ho, P.-C. Chao, M.-Y. Ko, P. Smith, J. Ballingall, J. Bautista, and G. Ortiz, "32-GHz cryogenically cooled HEMT low-noise amplifiers", IEEE Transactions on Electron Devices **36**, 1528–1535 (1989).

[61]M. A. McCulloch, J. Grahn, S. J. Melhuish, P.-A. Nilsson, L. Piccirillo, J. Schleeh, and N. Wadefalk, "Dependence of noise temperature on physical temperature for cryogenic low-noise amplifiers", Journal of Astronomical Telescopes, Instruments, and Systems **3**, 014003 (2017).

[62]A. Y. Choi, I. Esho, B. Gabritchidze, J. Kooi, and A. J. Minnich, "Characterization of self-heating in cryogenic high electron mobility transistors using schottky thermometry", Journal of Applied Physics **130**, 155107 (2021).

[63]S. W. Van Sciver, *Helium cryogenics* (Springer New York, New York, NY, 2012).

[64]S. W. Van Sciver, "Applications of superfluid helium in large-scale superconducting systems", in *Quantized vortex dynamics and superfluid turbulence*, Vol. 571, edited by C. F. Barenghi, R. J. Donnelly, and W. F. Vinen, red. by R. Beig, J. Ehlers, U. Frisch, K. Hepp, W. Hillebrand, D. Imboden, R. L. Jaffe, R. Kippenhahn, R. Lipowsky, H. v. Löhneysen, I. Ojima, H. A. Weidenmüller, J. Wess, and J. Zittartz, Series Title: Lecture Notes in Physics (Springer Berlin Heidelberg, Berlin, Heidelberg, 2001), pp. 51–65.

[65]P. Lebrun, L. Serio, L. Tavian, and R. Weelderen, "Cooling strings of superconducting devices below 2 k: the helium II bayonet heat exchanger", in *Advances in cryogenic engineering*, edited by P. Kittel (Springer US, Boston, MA, 1998), pp. 419–426.

[66]B. Baudouy, "Heat transfer and cooling techniques at low temperature", Proceedings of the CAS-CERN Accelerator School: Superconductivity for Accelerators, edited by R. Bailey, Publisher: CERN (2014).

[67]P. Lebrun, "Twenty-three kilometres of superfluid helium cryostats for the superconducting magnets of the large hadron collider (LHC)", in *Cryostat design*, edited by J. Weisend II, Series Title: International Cryogenics Monograph Series (Springer International Publishing, Cham, 2016), pp. 67–94.

[68]D. R. Tilley and J. Tilley, *Superfluidity and superconductivity*, 3. ed., repr, Graduate student series in physics (Inst. of Physics Publ, Bristol, 2003), 470 pp.

[69]P. Lebrun, *Superfluid helium as a technical coolant*, CERN-LHC-Project-Report-125 (CERN, Geneva, July 1997), p. 15.

[70]F. London, *Superfluids. volume 1. macroscopic theory of superconductivity volume 1. macroscopic theory of superconductivity*, OCLC: 439791906 (Dover, New York, 1961).

[71]J. Wilks, *The properties of liquid and solid helium* (Oxford University Press, New York, Jan. 1967), 703 pp.

[72]A. J. Leggett, "Superfluidity", Reviews of Modern Physics **71**, S318–S323 (1999).

[73]A. Schmitt, *Introduction to superfluidity*, Vol. 888, Lecture Notes in Physics (Springer International Publishing, Cham, 2015).

[74]W. P. Halperin, "Eighty years of superfluidity", Nature **553**, 413–414 (2018).

[75]P. Kapitza, "Viscosity of liquid helium below the lambda-point", Nature **141**, 74–74 (1938).

[76]J. F. Allen and A. D. Misener, "Flow of liquid helium II", Nature **141**, 75–75 (1938).

[77]R. J. Donnelly, "The discovery of superfluidity", Physics Today **48**, 30–36 (1995).

[78]K.-H. Bennemann and J. B. Ketterson, *Novel superfluids: volume 1* (Oxford University Press, Feb. 28, 2013).

[79]C. D'Errico, S. S. Abbate, and G. Modugno, "Quantum phase slips: from condensed matter to ultracold quantum gases", Philosophical Transactions of the Royal Society A: Mathematical, Physical and Engineering Sciences **375**, 20160425 (2017).

[80]F. Tafuri, ed., *Fundamentals and frontiers of the josephson effect*, Springer Series in Materials Science volume 286 (Springer, Cham, 2019), 859 pp.

[81]E. Varoquaux, "Anderson's considerations on the flow of superfluid helium: some offshoots", Reviews of Modern Physics **87**, 803–854 (2015).

[82]A. Joshi and R. Packard, "A continuously operating, flux locked, superfluid interferometer", Journal of Low Temperature Physics **172**, 162–174 (2013).

[83]R. E. Packard and Y. Sato, "Superfluid helium quantum interference devices (SHeQUIDs): principles and performance", Journal of Physics: Conference Series **568**, 012015 (2014).

[84]L. A. DeLorenzo and K. C. Schwab, "Ultra-high q acoustic resonance in superfluid 4he", arXiv:1607.07902 [cond-mat, physics:quant-ph] (2016).

[85]J. G. E. Harris, A. D. Kashkanova, A. B. Shkarin, C. D. Brown, S. Garcia, K. Ott, and J. Reichel, "Quantum optomechanics experiments in superfluid helium", in Rochester conference on coherence and quantum optics (CQO-11) (2019), Tu2B.1.

[86]A. B. Shkarin, A. D. Kashkanova, C. D. Brown, S. Garcia, K. Ott, J. Reichel, and J. G. E. Harris, "Quantum optomechanics in a liquid", Physical Review Letters **122**, 153601 (2019).

[87]S. Singh, L. A. D. Lorenzo, I. Pikovski, and K. C. Schwab, "Detecting continuous gravitational waves with superfluid ^{4} he", New Journal of Physics **19**, 073023 (2017).

[88]V. Vadakkumbatt, M. Hirschel, J. Manley, T. J. Clark, S. Singh, and J. P. Davis, "Prototype superfluid gravitational wave detector", Physical Review D **104**, 082001 (2021).

[89]K. Schutz and K. M. Zurek, "On the detectability of light dark matter with superfluid helium", Physical Review Letters **117**, 121302 (2016).

[90]D. Carney, G. Krnjaic, D. C. Moore, C. A. Regal, G. Afek, S. Bhave, B. Brubaker, T. Corbitt, J. Cripe, N. Crisosto, A. Geraci, S. Ghosh, J. G. E. Harris, A. Hook, E. W. Kolb, J. Kunjummen, R. F. Lang, T. Li, T. Lin, Z. Liu, J. Lykken, L. Magrini, J. Manley, N. Matsumoto, A. Monte, F. Monteiro, T. Purdy, C. J. Riedel, R. Singh, S. Singh, K. Sinha, J. M. Taylor, J. Qin, D. J. Wilson, and Y. Zhao, "Mechanical quantum sensing in the search for dark matter", Quantum Science and Technology **6**, 024002 (2021).

[91]R. Barron and G. Nellis, *Cryogenic heat transfer, second edition* (CRC Press, May 23, 2016).

[92]T. Trollier, J. Tanchon, Y. Icart, and A. Ravex, "High capacity 30 k remote helium cooling loop", in (2014), pp. 1461–1466.

[93]T. Trollier, J. Tanchon, J. Lacapere, and P. Camus, "30 k to 2 k vibration free remote cooling systems", IOP Conference Series: Materials Science and Engineering **755**, 012041 (2020).

[94]R. C. Richardson and E. N. Smith, eds., *Experimental techniques in condensed matter physics at low temperatures*, Advanced book classics, OCLC: ocn221243361 (Westview Press, Boulder, Colo, 1998), 338 pp.

[95]G. K. White and P. J. Meeson, *Experimental techniques in low-temperature physics*, 4th ed, Monographs on the physics and chemistry of materials 59, OCLC: ocm46694689 (Clarendon Press ; Oxford University Press, Oxford : New York, 2002), 280 pp.

[96]F. Pobell, *Matter and methods at low temperatures*, 3rd, rev. and expanded ed (Springer, Berlin ; New York, 2007), 461 pp.

[97]R. Radebaugh, "Review of refrigeration methods", in *Handbook of superconducting materials* (Taylor and Francis Books, Inc., Oxfordshire, 2020).

[98]K. Pieterman, J. A. M. Dam, and H. Postma, "Low temperature closed cooling system for MRI magnets", in *Advances in cryogenic engineering*, edited by R. W. Fast (Springer US, Boston, MA, 1986), pp. 533–541.

[99]J. Duchateau and B. Turck, "Application of superfluid helium cooling techniques to the toroidal field systems of tokamaks", IEEE Transactions on Applied Superconductivity **9**, Conference Name: IEEE Transactions on Applied Superconductivity, 157–160 (1999).

[100]R. C. Duckworth, J. A. Demko, A. Lumsdaine, J. Rapp, T. Bjorholm, R. H. Goulding, J. B. O. Caughman, and W. D. McGinnis, "Cryogenic considerations for superconducting magnet design for the material plasma exposure experiment", IOP Conference Series: Materials Science and Engineering **101**, 012143 (2015).

[101]H. Vaghela, V. J. Lakhera, and B. Sarkar, "Forced flow cryogenic cooling in fusion devices: a review", Heliyon **7**, e06053 (2021).

[102]L. Tisza, "Transport phenomena in helium II", Nature **141**, 913–913 (1938).

[103]L. Landau, "Theory of the superfluidity of helium II", Physical Review **60**, 356–358 (1941).

[104]R. J. Donnelly and C. F. Barenghi, "The observed properties of liquid helium at the saturated vapor pressure", Journal of Physical and Chemical Reference Data **27**, 1217–1274 (1998).

[105]N. Bogolyubov, "On the theory of superfluidity", J. Phys. (USSR) **11**, 23–32 (1947).

[106]R. P. Feynman, "Atomic theory of the two-fluid model of liquid helium", Physical Review **94**, 262–277 (1954).

[107]P. P. Craig and J. R. Pellam, "Observation of perfect potential flow in superfluid", Physical Review **108**, 1109–1112 (1957).

[108]W. Van Alphen, R. De Bruyn Ouboter, and K. Taconis, "Persistent superfluid flow in a circuit filled with jeweller's rouge", Physics Letters A **24**, 380–381 (1967).

[109]L. G. Grimes and L. c. Jackson, "The thickness of the saturated helium film above and below the lambda-point", Philosophical Magazine **4**, 1346–1355 (1959).

[110]E. S. Sabisky and C. H. Anderson, "Verification of the lifshitz theory of the van der waals potential using liquid-helium films", Physical Review A **7**, 790–806 (1973).

[111]W. E. Keller, "Thickness of the static and the moving saturated he II film", Physical Review Letters **24**, 569–573 (1970).

[112]C. Van den Meijdenberg, K. Taconis, and R. De Bruyn Ouboter, "The entropy of helium II under pressure from measurements on the fountain effect", Physica **27**, 197–218 (1961).

[113]J. Maynard, "Determination of the thermodynamics of he II from sound-velocity data", Physical Review B **14**, 3868–3891 (1976).

[114]Andronikashvili, Zh. Esksp. Theor. Fiz. **16**, 780 (1946).

[115]V. Arp, "Heat transport through helium II", Cryogenics **10**, 96–105 (1970).

[116]B. Rousset and F. Viargues, "An alternative cooling scheme for the TeV superconducting linear accelerator project", Cryogenics **34**, 91–94 (1994).

[117]W. Van Alphen, G. Van Haasteren, R. De Bruyn Ouboter, and K. Taconis, "The dependence of the critical velocity of the superfluid on channel diameter and film thickness", Physics Letters **20**, 474–475 (1966).

[118]R. B. Hallock and E. B. Flint, "Quasi-isothermal superfluid-film flow: oscillations between two reservoirs", Physical Review A **10**, 1285–1299 (1974).

[119]P. Kapitza, "The study of heat transfer in helium II", in *Helium 4* (Elsevier, 1971), pp. 114–153.

[120]T. Frederking, "Thermal transport phenomena at liquid he II temperatures", Chem. Eng. Progr. Symp Series **64**, 21–55 (1968).

[121]N. Snyder, "Heat transport through helium II: kapitza conductance", Cryogenics **10**, 89–95 (1970).

[122]I. M. Khalatnikov, *An introduction to the theory of superfluidity*, 1st ed. (W.A. Benjamin, New York, 1965).

[123]S. Takada, M. Murakami, N. Kimura, and J. G. Weisend, "Heat transfer characteristics of four film boiling modes around a horizontal cylindrical heater in he II", in AIP conference proceedings (2010), pp. 1335–1342.

[124]K. Betts and A. Leonard, "Free convection film boiling from a flat, horizontal surface in saturated he II", Adv. Cryog. Eng. **21**, 282–292 (1975).

[125]D. Labuntzov and Y. Ametistov, "Analysis of helium II film boiling", Cryogenics **19**, 401–404 (1979).

[126]A. Kryukov and S. Van Sciver, "Calculation of the recovery heat flux from film boiling in superfluid helium", Cryogenics **21**, 525–528 (1981).

[127]M. Arthur, "Measurement of noise performance factors", in 1973 IEEE g-MTT international microwave symposium (1973), pp. 226–226.

[128]R. Pettai, *Noise in receiving systems* (Wiley, New York, 1984), 273 pp.

[129]M. Leffel and R. Daniel, *The y factor technique for noise figure measurements*, Oct. 29, 2021.

[130]J. E. Fernandez, "A noise-temperature measurement system using a cryogenic attenuator", Telecommunications and Mission Operations Progress Report **135**, ADS Bibcode: 1998TMOPR.135F...1F, 1–9 (1998).

[131]D. M. Pozar, *Microwave engineering*, 4th ed, OCLC: ocn714728044 (Wiley, Hoboken, NJ, 2012), 732 pp.

[132]A. Cowley and H. Sorensen, "Quantitative comparison of solid-state microwave detectors", IEEE Transactions on Microwave Theory and Techniques **14**, 588–602 (1966).

[133]V. Giordano, C. Fluhr, B. Dubois, and E. Rubiola, "Characterization of zero-bias microwave diode power detectors at cryogenic temperature", Review of Scientific Instruments **87**, 084702 (2016).

[134]A. Soliman, A. Janzen, and S. Weinreb, "Thermal modelling of coaxial line for cryogenic noise measurements", in 2016 URSI asia-pacific radio science conference (URSI AP-RASC) (Aug. 2016), pp. 900–903.

[135]A. F. Mills, *Heat transfer*, 2nd ed (Prentice Hall, Upper Saddle River, N.J, 1999), 954 pp.

[136]*NIST material properties: teflon*.

[137]*NIST material properties: 304 stainless (UNS s30400)*.

[138]L. M. Jiji, *Heat convection*, 2. ed (Springer, Berlin Heidelberg, 2009), 543 pp.

[139]J. L. Cano, N. Wadefalk, and J. D. Gallego-Puyol, "Ultra-wideband chip attenuator for precise noise measurements at cryogenic temperatures", IEEE Transactions on Microwave Theory and Techniques **58**, Conference Name: IEEE Transactions on Microwave Theory and Techniques, 2504–2510 (2010).

[140]J. F. Allen and A. Misener, "The properties of flow of liquid he ll", Proceedings of the Royal Society of London. Series A. Mathematical and Physical Sciences **172**, 467–491 (1939).

[141]A. Evenson, D. Brewer, A. Symonds, and A. Thomson, "Van der waals potential for helium adsorbed on glass and nitrogen coated glass", Physics Letters A **33**, 35–36 (1970).

[142]M. H. W. Chan, A. W. Yanof, and J. D. Reppy, "Superfluidity of thin he 4 films", Physical Review Letters **32**, 1347–1350 (1974).

[143]M. Somerville, A. Ernst, and J. del Alamo, "A physical model for the kink effect in InAlAs/InGaAs HEMTs", IEEE Transactions on Electron Devices **47**, 922–930 (2000).

[144]R. Webster, Shangli Wu, and A. Anwar, "Impact ionization in InAlAs/InGaAs/InAlAs HEMT's", IEEE Electron Device Letters **21**, 193–195 (2000).

[145]J. Kooi, *Private communcation*, E-mail, 2022.

[146]S. Simbierowicz, V. Vesterinen, J. Milem, A. Lintunen, M. Oksanen, L. Roschier, L. Grönberg, J. Hassel, D. Gunnarsson, and R. E. Lake, "Characterizing cryogenic amplifiers with a matched temperature-variable noise source", Review of Scientific Instruments **92**, 034708 (2021).

[147]D. Russell, K. Cleary, and R. Reeves, "Cryogenic probe station for on-wafer characterization of electrical devices", Review of Scientific Instruments **83**, 044703 (2012).

[148]N. R. Naik and A. J. Minnich, "Quasiballistic electron transport in cryogenic SiGe HBTs studied using an exact, semi-analytic solution to the boltzmann equation", Journal of Applied Physics **130**, 174504 (2021).

[149]F. Caspers, "RF engineering basic concepts: s-parameters", CAS - CERN Accelerator School: Specialised Course on RF for Accelerators, Publisher: CERN (2010).

Appendix A

CORRECTION ALGORITHM FOR A CHANGING NOISE SOURCE IMPEDANCE

We present an algorithm to correct for the error introduced into the measured noise power by a changing impedance mismatch at the input of a 2-port network consisting of the following components: (1) a microwave noise source at the input with reflection coefficients S_{22}^{H} and S_{22}^{C} at its output plane in the hot and cold states respectively; (2) a power detector at the output with reflection coefficient S_{11}^{BE} at its input plane; (3) any series of elements connecting the noise source to the detector which we can treat as a single element with S-matrix $\mathbf{S^{net}}$. This scenario is shown schematically in Fig. A.1(a). The technique relies on mathematically cascading these quantities to find an effective cascaded gain S_{21}^{casc} of the entire network which is used to modify Eq. (2.6).

First each quantity $S_{22}^{(\mathrm{H,C})}$, S_{11}^{BE}, and S_{ij}^{net} is measured. Next a set of effective S-pars for the noise source and detector are defined as $S_{11}^{\mathrm{H,C}} = 0$, $S_{21}^{\mathrm{H,C}} = S_{12}^{\mathrm{H,C}} = S_{21}^{\mathrm{BE}} = S_{12}^{\mathrm{BE}} = 1$, and $S_{22}^{\mathrm{BE}} = 0$, so that each component has a fully defined S-matrix. This is equivalent

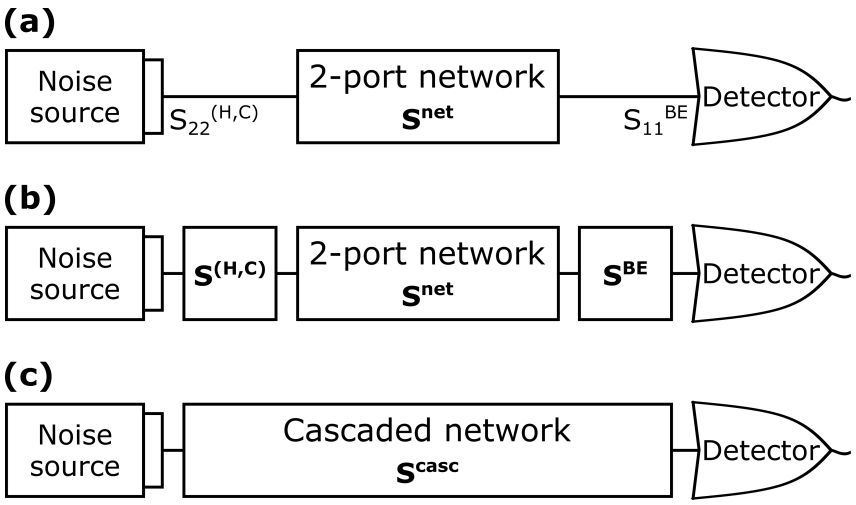

Fig. A.1: Equivalent noise measurement scheme representations involving a noise source, an intermediate 2-port network, and a detector where **(a)** reflections are attributed to the noise source output plane and detector input plane, **(b)** the noise source and detector are treated as ideal and virtual components carry the associated S-pars, and **(c)** the noise source and detector are treated as ideal and all S-pars are cascaded into a single element.

to treating the noise source and detector as ideal, perfectly matched elements and introducing virtual components at the input and output of the network with S-matrices $\mathbf{S^{(H,C)}}$ and $\mathbf{S^{BE}}$, respectively, using the S-pars defined above. This network is shown schematically in Fig. A.1(b), and is equivalent to the network shown in Fig. A.1(a).

In order to cascade each component, we transform from the scattering matrix (S-matrix) representation to the transfer matrix (T-matrix) representation. Since there are several T-matrix formalisms (see, for example, the ABCD matrix defined in Chapter 4 of Ref. [131]), we adopt the definition from Appendix A of Ref. [149] which does not rely on knowing the reference impedance Z_0. In terms of S_{ij}, the T-matrix elements T_{ij} are given by:

$$\begin{aligned} T_{11} &= \frac{S_{12}S_{21} - S_{22}S_{11}}{S_{21}}, & T_{12} &= \frac{S_{11}}{S_{21}} \\ T_{21} &= -\frac{S_{22}}{S_{21}}, & T_{22} &= \frac{1}{S_{21}} \end{aligned} \tag{A.1}$$

The T-matrix $\mathbf{T_M}$ of m cascaded 2-ports is then given by matrix multiplication:

$$\mathbf{T_M} = \mathbf{T_1 T_2} \ldots \mathbf{T_m} \tag{A.2}$$

We use Eq. (A.1) to transform each of the three components in our network, cascade them using Eq. (A.2), and then transform back to the S-matrix representation using:

$$\begin{aligned} S_{11} &= \frac{T_{12}}{T_{22}}, & S_{12} &= \frac{T_{11}T_{22} - T_{12}T_{21}}{T_{22}} \\ S_{21} &= \frac{1}{T_{22}}, & S_{22} &= -\frac{T_{21}}{T_{22}} \end{aligned} \tag{A.3}$$

The final cascaded network is shown schematically in Fig. A.1(c) and is equivalent to the networks shown in Figs. A.1(a) and A.1(b).

This procedure allows us to define effective gains of the cascaded network $G^{\mathrm{H}}_{\mathrm{casc}} = |S^{\mathrm{H}}_{21}|^2$ with the noise source on and $G^{\mathrm{C}}_{\mathrm{casc}} = |S^{\mathrm{C}}_{21}|^2$ with the noise source off. We use these to modify Eqs. (2.4) and (2.5) as follows:

$$\begin{aligned} \frac{P_{\mathrm{H}}}{Bk_{\mathrm{B}}} = \Bigg(& T_{\mathrm{H}} \frac{G^{\mathrm{H}}_{\mathrm{casc}}}{L_1 L_2 L_3} + T_{L_1} \frac{G^{\mathrm{H}}_{\mathrm{casc}}(L_1 - 1)}{L_1 L_2 L_3} \\ & + T_{L_2} \frac{G^{\mathrm{H}}_{\mathrm{casc}}(L_2 - 1)}{L_2 L_3} + T_e \frac{G^{\mathrm{H}}_{\mathrm{casc}}}{L_3} + T_{L_3} \frac{(L_3 - 1)}{L_3} + T_{\mathrm{BE}} \Bigg) \end{aligned} \tag{A.4}$$

$$\frac{P_{\mathrm{C}}}{Bk_{\mathrm{B}}} = \left(T_{\mathrm{C}} \frac{G^{\mathrm{C}}_{\mathrm{casc}}}{L_1 L_2 L_3} + T_{L_1} \frac{G^{\mathrm{C}}_{\mathrm{casc}}(L_1 - 1)}{L_1 L_2 L_3} \right.$$
$$\left. + T_{L_2} \frac{G^{\mathrm{C}}_{\mathrm{casc}}(L_2 - 1)}{L_2 L_3} + T_e \frac{G^{\mathrm{C}}_{\mathrm{casc}}}{L_3} + T_{L_3} \frac{(L_3 - 1)}{L_3} + T_{\mathrm{BE}} \right) \quad \text{(A.5)}$$

We can again solve for T_{e} by plugging Eqs. (A.4) and (A.5) into Eq. (2.1). and arrive at:

$$T_{\mathrm{e}} = \frac{1}{L_1 L_2} \left[\frac{T_0 E}{Y' - 1} - T_{\mathrm{C}} - T_{\mathrm{coax}}(L_1 - 1) - T_{L_2}(L_2 - 1) L_1 - \frac{Y - 1}{G^{\mathrm{H}}_{\mathrm{casc}}} \left(T_3 \frac{L_3 - 1}{L_3} + T_{\mathrm{BE}} \right) \right] \quad \text{(A.6)}$$

where we have defined $Y' = Y G^{\mathrm{C}}_{\mathrm{casc}} (G^{\mathrm{H}}_{\mathrm{casc}})^{-1}$.

Fig. A.2 shows the extracted noise temperature T_{e} from measurements of an identically designed device to the primary LNA studied in this work, taken at room temperature using the noise source and backend detector described in Section 2.2. The extraction using Eqs. (2.6) and (A.6) are both shown, along with a separate measurement taken using a commercial NFA whose noise source uses attenuation pads to dampen the effect of the impedance change between hot and cold states (a technique which is not applicable when unattenuated noise power is required). The DUT has a relatively high reflection coefficient $|S_{11}| \approx -2$ dB over its bandwidth, and was connected directly to the output of each noise source. Without correction, oscillations of approximately 20 K magnitude with a roughly 1 GHz period can be seen seen. The NFA measurement also exhibits noise temperature oscillations with frequency, but the attenuator pads suppress their magnitude to less than roughly 5 K. With the correction algorithm, the agreement between the NFA measurement and the extracted T_{e} improves significantly.

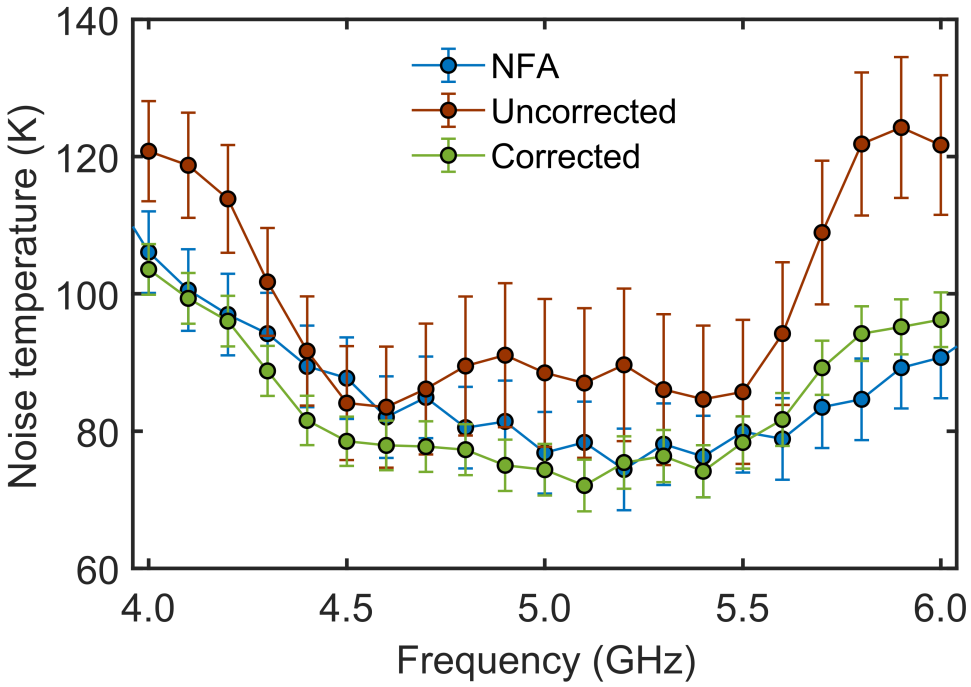

Fig. A.2: Noise temperature of packaged HEMT amplifier versus frequency measured at room temperature with a commerical NFA (blue circles) and with the noise measurement setup described in Section 2.2 using the uncorrected Eq. (2.6) (red circles) and the corrected Eq. (A.6) (green circles). The agreement between the two measurements improves upon correction. All measurements were performed at the same bias. Error bars reflect the overall measurement uncertainty, including the impedance mismatch in the uncorrected case.